Discretizing the sphere with an irregular lattice: Application to the transverse-field Ising model

Master's thesis

Submitted to the Faculty of Mathematics, Computer Science
and Natural Sciences at RWTH Aachen University

presented by

Grigorios Makris

under the supervision of

Prof. Dr. Fabian Hassler

Institute for Quantum Information
and
Prof. Dr. Stefan Wessel

Institute for Theoretical Solid State Physics

10/2024

Abstract

The thesis investigates the discretization of the sphere with irregular lattices, on which physical systems, and in particular the transverse-field Ising model, can be studied. More specifically, irregular lattices are necessary since, for arbitrary number of sites, the sphere cannot be covered with a regular grid. We solve the free particle problem on lattices that are easy to scale up and investigate if the expected $SO(3)$ symmetry is recovered with increasing lattice size. The Fibonacci lattice is shown to be a good candidate for this. Having obtained the nearest neighbor hoppings for the free particle problem, we directly utilize them as interaction coefficients in the transverse-field Ising model placed on the Fibonacci lattice. With this choice of coefficients, the spin spectrum showcases better (approximate) degeneracies of the $SO(3)$ compared to the case with constant coefficients. The search for the critical point of the system is halted due to pronounced finite-size effects.

Contents

List of Figures

List of Tables

Chapter 1

Introduction

The problem of discretizing the sphere, by distributing points on it uniformly, has a long history and is relevant in many fields of research, such as statistical physics, climate modeling and chemistry. On its own right, it is an interesting geometric problem as well. There are the constructions, such as the Plato and Archimedean solids, where the points are distributed in such a way that they are all symmetric. The Plato solids cover the sphere with identical polygonal faces while the Archimedean solids may have alternating faces. A major limitation of such geometries is the relatively small number of points they contain and the general inability to scale them up arbitrarily by keeping the same local structure and symmetry.

It is of general interest to make constructions that include many points. For arbitrary number of points, the distributions are, in principle, approximately, rather than exactly, uniform. In this case, the notion of uniformity is not clear and, thus, different approaches have been followed. These approaches are not necessarily mutually exclusive. One of them is establishing an equal area partitioning of the sphere. Another would be seeking to maximize the smallest distance between different points, making the *packing* of points optimal. This is, also, referred to as the Tammes's problem [1] and it has been analytically evaluated for small number of points [2]. A general optimization method includes making the points interact with each other through a potential (for example the Coulomb potential) and finding the configuration with the minimum potential energy. This relates to the Thomson problem. [1], [3]. Interestingly for number of points, $N = 8$ and $N = 20$, the polyhedra that minimize the potential energy are not reported to be the Plato solids, even though these are symmetric configurations [4].

Furthermore, there exist constructions that are considered to have approximately uniform distributions and do not, necessarily, require optimization. This makes it easier to create configurations with increasing number of points. For example, starting from the Platonic solids, points are added symmetrically across their faces. This implementation has been used in studies, for example in [5], [6], [7], either as the main geometry or a

starting point for considerations. A different construction would be to implement spiral points. In this case, one chooses a rule for the azimuthial angle, φ, and fills the spherical surface by moving along the polar angle with a specified step [1]. The use of spirals can be motivated by the empirical observations for the packing they produce and for being reasonably close to configurations that minimize certain potential energies [1] , [8]. Further motivation is given explicitly in the context of this thesis.

Choosing a construction is relevant in physics as many problems relate to the sphere. There might be problems, such as the hydrogen atom, where the solutions to Schrödinger's equation can be treated analytically and expressed in terms of spherical harmonics. However, problems such as the aforementioned Thomson problem, where one wants to find the equilibrium positions of many interacting electrons on the sphere, do not in general allow for an analytic solution. A numerical solution, which utilizes a construction of a spherical grid (or mesh), is required. The need for a numerical solution arises also, for example, in the field of geophysical fluid dynamics where one has to solve partial differential equations on a meshed spherical geometry [9].

Placing a spin system on the sphere is relevant in the context of phase transitions. A system, such as the ones that are studied in this thesis, exhibits a phase transition when it undergoes a change of phase from disordered to ordered, with respect to its order parameter (for example the magnetization in the case of spin systems). At its critical point, it exhibits scale invariance, due to the lack of a characteristic scale [10]. There are systems that at the critical point exhibit not only scale invariance but, rather, the more general conformal symmetry. In this case, their correlation functions transform covariantly under conformal transformations. A system that has been shown analytically to exhibit conformal symmetry at criticality is the 1 dimensional transverse-field Ising chain [11].

Conformal symmetry implies a relation for the correlation functions between a system studied on the flat space $\mathbb{R}^d$ and on the "cylinder" $S^{d-1} \times \mathbb{R}$ [12]. In particular, it implies finite-size scaling predictions for the correlation length in the infinite direction, $\mathbb{R}$, of the cylinder. This motivates the study of models on the sphere, S^2. The reason for using a quantum model in particular becomes apparent due to the quantum to classical mapping. A quantum system may be mapped to a classical model in a dimension higher. This additional dimension should correspond to the $\mathbb{R}$ in $S^2 \times \mathbb{R}$. Verifying the predictions due to conformal symmetry for three dimensions numerically, using discretized spheres, has been suggested since [12] was published. There have been attempts to study critical systems by implementing discrete spheres [13], [14] and more elaborate finite-element methods on sphere [15]. More recently, the fuzzy sphere has been introduced leading to more precise results [16]. However, this method does not utilize a lattice construction.

The aim of this thesis is to define the transverse-field Ising model (TFIM) on the sphere, in a way that it respects the characteristic $SO(3)$ symmetry, expected for a system on a sphere. To achieve that, we, firstly, solve for the free particle on the sphere,

as it is a non-interacting problem which we can scale up easily and whose spectrum we can straightforwardly evaluate. The free particle Hamiltonian is directly related to the Laplacian which we can treat as a tight-binding model with hoppings between neighboring points. Having established a configuration that yields the characteristic spectrum with $2l+1$ degeneracies, where l is the angular momentum quantum number, we utilize the hoppings as interaction terms in the TFIM.

The thesis is organized as follows.

- In Ch. 2, the candidate lattices on which we will solve the free particle problem are introduced and compared. These are the Fibonacci lattice, which is a spiral lattice, and a construction that starts from the icosahedron and symmetrically adds vertices on its faces, the icosahedron-seed. The spectra of the free particle on the two lattices are compared and as a result the Fibonacci lattice is chosen. Furthermore, in the case of Fibonacci, we motivate an explanation for the limitations the underlying lattice imposes on the spectrum.

- In Ch. 3 the general theory of phase transitions, relevant for the Ising models, is further explained. After a brief explanation of how symmetry breaking can occur, we formally state how the quantum model can map to a classical Ising model of a dimension higher. This allows for the explanation of the quantum phase transition in terms of that of the classical model [17]. Since phase transitions formally occur on infinite systems, we introduce the finite-size scaling theory. The theory makes predictions for how the finite sized counterparts of the infinite systems behave near the critical point. The exposition is motivated through the underlying renormalisation group methods which we briefly explain in App. D. Moreover, finite-size scaling is important in the sense that the existence or not of conformal symmetry can be inferred even on finite systems. In the last section of the chapter, we describe the explicit predictions with which conformal symmetry supplements finite-size scaling. This, as discussed, motivates studying the, bounded in two directions, $S^2 \times \mathbb{R}$ geometry.

- In Ch. 4 the TFIM is placed on the Fibonacci lattice with its interaction terms being the free particle hoppings. We study the low energy spectrum for system sizes that the exact diagonalization permits. We compare it to the case of the same model with constant interaction terms and evaluate in which of the two the degeneracies of the $SO(3)$ are visibly recovered. Furthermore, we motivate why using the free particle hoppings as interaction terms makes the spherical model locally similar to the flat 2 dimensional TFIM. Afterwards, we attempt to find the critical point of the system by looking at intersections of the Binder cumulant for various system sizes, using the SSE quantum monte carlo method.

Chapter 2

Constructing a discrete sphere

The goal of this chapter is to construct a lattice that approximates a sphere. In the ideal case, we would want to cover the sphere with a *regular lattice*. Well known regular lattices are the regular polyhedra or Platonic solids [1]. These three-dimensional geometries consist of flat identical faces and straight edges. The edges intersect at the lattice sites (also named vertices or points). Three regular polyhedra are shown in Fig. 2.1. The cube, which has square faces and 8 vertices, the regular icosahedron, with triangular faces and 12 vertices and the regular dodecahedron, with regular pentagonal faces and 20 vertices. However, such regular polyhedra exist only for specific number of vertices N, namely $N = 4, 6, 8, 12$ and 20 (see App. A, for a proof). To study lattices with more sites, we would, in principle, have to approximate the sphere with *irregular lattices*. An irregular lattice is, for example, a polyhedron whose points do not uniformly cover the sphere and does not have identical faces. Implementing irregular lattices, to approximate the sphere, has been a long-standing problem. It has been studied through various approaches, see for example [1] for a review.

In this chapter, we will implement two irregular lattices, the Fibonacci lattice and the icosahedron-seed. With both approaches, we will have a systematic way to increase the number of points we use. The Fibonacci lattice is a spiral lattice where the golden angle is used to allocate the points on the sphere. The icosahedron-seed symmetrically adds vertices on the triangular faces of the regular icosahedron. In order to judge which lattice better approximates the sphere, we will study symmetry properties of the lattices. Physical systems on a sphere have an $SO(3)$ symmetry. This implies that to each angular momentum quantum number l, there is a $2l+1$ degenerate energy level. To observe this, we will first study the free particle on a sphere. Based on our observation,

[1] As mentioned in the introduction, for number of vertices 8 and 20 these symmetric configurations are not reported to yield a minimum of the Thomson problem [4]. So, they may not be the most uniform distributions of points on the sphere. Nevertheless, they are still regular lattices in the sense that they cover the sphere with a repeating pattern.

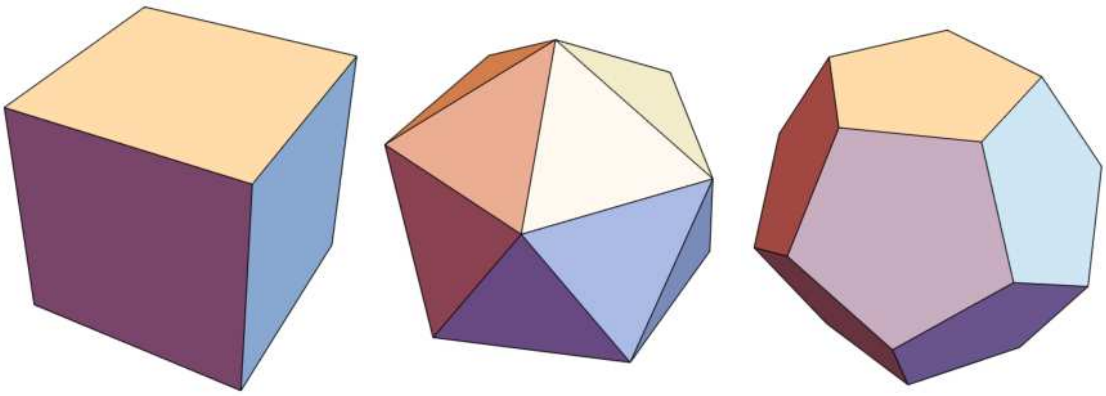

Figure 2.1: Examples of Platonic solids with (from left to right) $N = 8$ (cube), $N = 12$ (regular icosahedron) and $N = 20$ (regular dodecahedron) vertices. These are three of the five Platonic solids. The cube has square faces. The faces of the regular icosahedron are equilateral triangles and the faces of the regular dodecahedron are regular pentagons.

we will then decide whether the Fibonacci lattice or the icosahedron-seed provides a better approximation of the sphere. In addition, the study of the free particle enables us to define the generators of rotation. Implementing rotations will be useful in order to understand the geometric constraints on the spectrum.

2.1 Irregular lattices on the sphere

For arbitrary number of sites, N, we cannot have a perfect uniform distribution on a sphere. So, we resort to a non-uniform distribution. To create a lattice out of it, we must define connections between the sites. Doing so, we can create a (convex) polyhedron. Due to the non-uniformity, the polyhedron we create is irregular. Its face cannot, in general, be identical to each other (see App. A). This is equivalent to saying that the lattice does not have a well defined unit cell. Furthermore, the faces can, for example, be triangular, rectangular or pentagonal.

For our lattices, triangulation will be used. This is the process, where we create a convex polyhedron with triangular faces. The edges of the triangles define which sites are directly connected. In the following, we may also refer to them as nearest neighbors (NN) lattices. An example of a triangulated or NN lattice, is shown in Fig. 2.2 (a). This particular one is the triangulated Fibonacci lattice.

However, we can also choose to connect the sites by allowing edges to intersect each other. In this case, the geometry created is not a polyhedron. As an example, the Fibonacci lattice with intersecting edges is shown in Fig. 2.2 (b). We consider both cases because there is no clear rule that favors one or the other. What is relevant is which one is better for studying physical systems. We will make the comparison in Section. 2.2. There, we

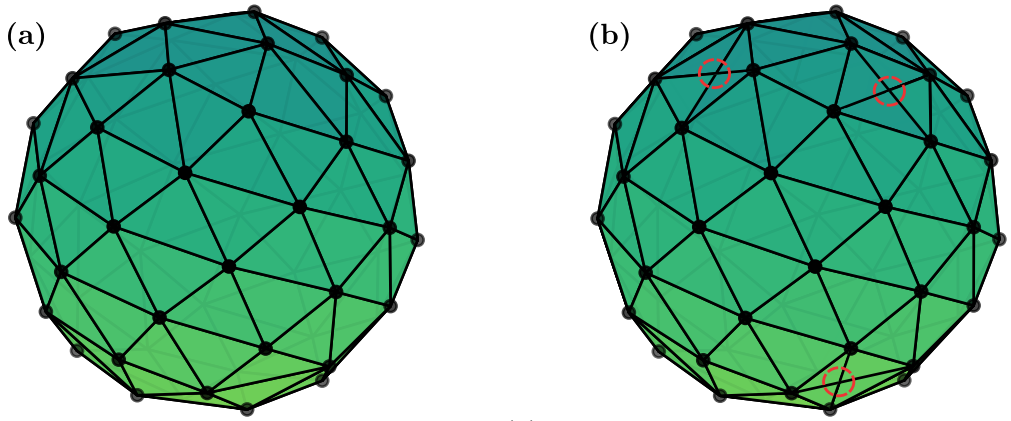

Figure 2.2: Fibonacci lattice with $N = 60$. (a) The triangulated Fibonacci lattice. This geometry is a convex polyhedron with triangular faces. (b) Fibonacci lattice where edges are allowed to intersect. Such intersections are spotted with the red dashed circles.

will solve the free particle on the sphere.

The lattices we will study are the Fibonacci lattice and the icosahedron-seed. We will explain how to construct them. Jointly with that, we will motivate why we chose these particular ones. That is to say, we will see if the distribution of sites is reasonably uniform. For the icosahedron-seed, all additional vertices are added symmetrically across the faces. Therefore, there is a sense of uniformity in this lattice.

To study the uniformity of the Fibonacci lattice, we consider two geometric measures. These are the *equal-area packing* and the *packing efficiency*. To give proper definitions and formulas, we closely follow Ref. [18]. We should note that both measures are defined on the plane and not on the sphere. However, we will construct the Fibonacci lattice from an initial spiral on the plane which gives optimal values for the two measures.

For each point n of the spiral, we have two polar coordinates (r_n, φ_n). The r_n is defined as

$$r_n = \sqrt{n}. \tag{2.1}$$

Here, we have $n = 0, 1, \ldots, N-1$. The first point sits at the center of the disk as shown in Fig. 2.3. The radius r_{N-1} defines the radius of our spiral. Due to Eq. (2.1), for every N it holds that $\frac{\pi r_{N-1}^2}{N-1} = \pi$. This is the equal-area packing. Even if we increase the number of points, the average area that corresponds to each point on the spiral is always constant and equal to π. This is the area of a ring formed between the circle with r_{n-1} and r_n. Evidently, the equal area packing is a global measure and does not provide information on the density of the points.

The rule for defining the φ_n makes use of the golden angle λ, where

$$\lambda = \left(1 - \frac{1}{\Phi}\right)2\pi = \left(3 - \sqrt{5}\right)\pi. \tag{2.2}$$

We see that λ is defined via the golden ratio

$$\Phi = \frac{1+\sqrt{5}}{2}. \tag{2.3}$$

For the azimuthial coordinate of the spiral we have

$$\varphi_n = n\lambda. \tag{2.4}$$

If we were to plot the φ_n on a unit circle, no two points would coincide due to lack of periodicity, virtue of λ being irrational. On the contrary, if λ was a rational number, we could more easily find the period. More specifically, a rational number is given by the ratio of two integers. The denominator of the ratio would correspond to the period.

We choose λ in particular since Φ is an irrational number which, in a sense, is the hardest to approximate with a rational [19]. Roughly speaking, the more irrational the number, the harder it is to be approximated by a ratio of two relatively prime numbers. That is to say, in order to get a good approximation to the golden ratio, the integers become larger and larger. So, to define a effective period, we would need an increasingly large value for the denominator. This is why we would expect to have a somewhat even distribution of points along the φ_n coordinate, without the need to go to large numbers.

To visually justify the use of the golden ratio, Fig. 2.3 shows two spirals, the one where the golden angle is used, Eq. (2.4), and one with $\varphi_n = \sqrt{2}\pi n$. Each consists of $N = 1000$ points. We can compare the choice of the two irrational numbers. For the $\sqrt{2}$ spiral, the points tend to accumulate along specific spirals. We can also follow spirals for sequence of points on the golden angle spiral. However, there, we more easily discern intersecting spirals, which disrupt the sequences. As a result, there is not as clear a pattern in this case.

In particular, the golden angle spiral exhibits higher packing efficiency [18],

$$\eta = \frac{1}{A}\inf\{|x-y|^2 : x, y \in X, x \neq y\}. \tag{2.5}$$

If η is large, then there should be no densely packed regions. Because of this and the equal area packing, we would expect that there would be no sparse regions either. This motivates the fact that the density of points will not vary considerably between different regions. To be more concrete on the optimum packing of spirals on the plane, consider the allocation,

$$X = \{\sqrt{n}e^{i2\pi n\delta} : n = 1, 2, 3, \dots\}. \tag{2.6}$$

According to [18], for $0 \leq \delta \leq \frac{1}{2}$, the maximum value for η is achieved if and only if $\delta = 2 - \Phi = \frac{3-\sqrt{5}}{2}$. Using λ, we have

$$X = \{\sqrt{n}e^{i\lambda n} : n = 1, 2, 3, \dots\}. \tag{2.7}$$

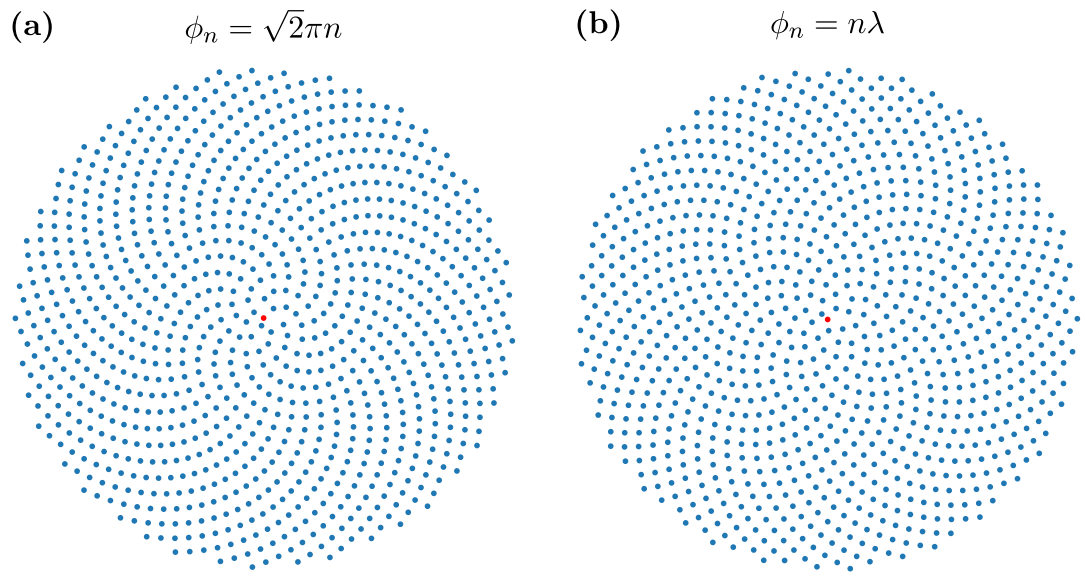

Figure 2.3: Spirals on the plane for $N = 1000$ points. a) For this spiral the azimuthial coordinate for the points is $\varphi_n = \sqrt{2}\pi n$. We can confirm visually that the points clearly accumulate on spirals. b) Here $\varphi_n = n\lambda$, where λ is the golden angle. It is harder to see accumulation of points on specific spirals. This leads us to the (visual) conclusion that the points are packed more homogeneously. The red points denote the origin.

Note that, Eq. (2.7) does not include $n = 0$. It is not obvious then, if we should include the point or not. We do so initially. However, we will discuss this further in the context of Fibonacci lattice on the sphere.

For the mapping to the sphere, we will consider unit spirals,

$$r_n = \sqrt{\frac{n}{N-1}}. \tag{2.8}$$

The spiral and the sphere have the same azimuthial angle, φ_n. The spherical polar angle is obtained from the mapping

$$\theta_n = \arccos\left(1 - 2r_n^2\right). \tag{2.9}$$

The coordinates of the unit sphere are then (φ_n, θ_n). The θ is related to r non-linearly because we want the mapping to be an equal-area mapping. Due to Eq. 2.4, no two points have the same φ on the spherical surface.

The cartesian coordinates of the points on the Fibonacci sphere are

$$(x_n, y_n, z_n) = \left(2r_n\sqrt{1-r_n^2}\cos\varphi_n, 2r_n\sqrt{1-r_n^2}\sin\varphi_n, 1-2r_n^2\right). \tag{2.10}$$

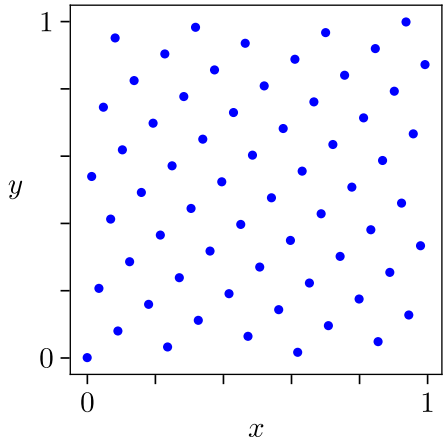

Figure 2.4: Spiral with golden angle mapped to a unit square, $N = 64$. The lattice is periodic in the x direction, since it represents the azimuthial direction of the spiral and of the sphere. The $y = 0{,}1$ boundaries represent the poles of the Fibonacci lattice on the sphere. Therefore, they are not equivalent.

We observe that $z_n = 1 - 2n$, due to Eq. (2.1). So, consecutive points have constant spacing in the z-axis. Note also that, for $n = 0$ and $n = N - 1$, we have $\theta_0 = 0$ and $\theta_{N-1} = \pi$. These are the north and south pole respectively.

Furthermore, we want to see if we can improve upon this spherical configuration. To do this, we need to consider perturbations of the Fibonacci lattice. Perturbations amount to sensibly shifting the lattice sites. The assessment of the perturbations will be discussed in Sections. 2.2 and 2.3. There, we will see if there exists a preferable variation, for which the free particle exhibits a better spherical symmetry.

However, even if there is no optimal perturbation, we will still be able to study physical systems on candidate configurations that resemble each other. This way, we can see how susceptible physical properties are to minor lattice changes. This will tell us if said changes are indeed important. To do all this, we must first introduce a structured way to implement different lattices.

To visualize this process, it is useful to consider one more mapping of the lattice. This is the mapping from the spiral to a unit square,

$$x_n = \varphi_n \left(\frac{1}{\lambda} - \frac{1}{2\pi} \right) \pmod 1 \,, \tag{2.11}$$

$$y_n = r_n^2. \tag{2.12}$$

The unit square is shown in Fig. 2.4. It may seem exhaustive to introduce an additional mapping at this point. However, it is easier to visualize the lattice shifts on the 2D plane rather than on the sphere or the spiral.

Despite the modulo factor in Eq. (2.11), which is there to bound x-direction to 1, the equation is linear in φ_n. Since it represents the azimuthial direction, this lattice is periodic along the x-axis. The mapping for y_n, Eq. (2.12), is not linear because we want an area-preserving mapping. The boundaries, $y = 0, 1$ on the square represent the poles of the sphere. The two boundaries are, therefore, not equivalent.

In order to realize different lattices, we add a constant offset $\frac{\varepsilon}{N-1}$ to the y in Eq. (2.12), where $0 \leq \varepsilon \leq 0.5$. We are basically translating the lattice of Fig. 2.4 along the y direction. Points that touch $y = 1$ are promoted to $y = 0$. In the sphere, due to Eq. (2.9), this would correspond to the translated south pole becoming too close to the translated north pole.

We want to avoid having two points in such small proximity. Therefore, the configuration with points on both poles, will be implemented only once. Otherwise, we will implement the Fibonacci lattice with $N+1$ points but we will, then, exclude the point on the south pole, so that we, again, have N points in total.

So, the configurations with N sites and no point in the south pole are given for all mappings, square-spiral-sphere, by

$$y_n = \frac{n+\varepsilon}{N}, \tag{2.13}$$

$$r_n = \sqrt{\frac{n+\varepsilon}{N}}, \tag{2.14}$$

and

$$\theta_n = \arccos\left\{1 - 2\left(\frac{n+\varepsilon}{N}\right)^2\right\}. \tag{2.15}$$

Here, $n = 0, 1, 2..., N-1$ and $0 \leq \varepsilon \leq 0.5$. As we increase the ε, the lattice sites move away from the north pole and closer to the south pole. The configuration, P, with both points on the poles is given by

$$\theta_n = \arccos\left\{1 - 2\left(\frac{n}{N-1}\right)^2\right\}, \qquad n = 0, 1, 2..., N-1. \tag{2.16}$$

We observe that the distances between the points on the poles and their neighbors, are always substantially smaller than the rest of the distances in the lattice. In addition to that, setting $\varepsilon = 0$ in Eq (2.15) corresponds to no point in the south pole. There, we also expect neighboring distances, that are larger than most distances within the lattice, to appear. Although the total number of such distances is not statistically significant, it remains for all system sizes.

Having explained the Fibonacci sphere[2], we will shortly describe the icosahedron-seed. To construct this lattice, we introduce vertices within each of the icosahedron faces, as

[2]We also want to note useful online resources for explanations and interactive visuals for the Fibonacci sphere, by Martin Roberts and Amit Sch.

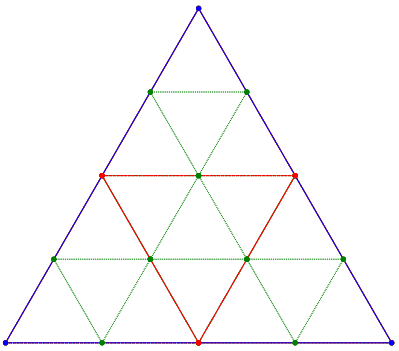

Figure 2.5: Generations of the icosahedron-seed. Blue: 0-generation. Triangular face of the original icosahedron. Red: 1-generation. Vertices are introduced at the mid-points of the blue edges. The vertices connect to 4 edges on this triangular face, visible, and to two edges on the adjacent triangular faces. Green: 2-generation. Vertices are introduced at the mid-points of the red and blue edges. The vertices connect to their six nearest vertices, which might also include vertices of adjacent triangular faces.

is done for example in [5]. We will call the k^{th} round of vertex generation, k-generation. So, the 0-generation is the regular icosahedron. In the 1-generation, we introduce vertices on the mid-points of each edge. We radially project the vertices on the surface of the sphere and, then, we connect the new vertices with each other.

Specifically, each new vertex connects to the 4 new immediate neighbors, in addition to the two closest existing vertices of the previous generation. In the 2-generation we again introduce vertices on the mid-points of all edges. We again project on the spherical surface. We connect the vertices with their 6 closest neighbors. Some of these connections might already exist because of the previous generation.

This process repeats up to the k we want. It is shown in Fig. 2.5. Each generation is painted with a different color. One can see that each of the original icosahedron vertices (blue vertices) gives rise to 5 edges. All the other vertices give rise to 6 edges each. To verify this, consider that some vertices also connect to vertices in adjacent triangular faces.

Therefore, the number of defects, namely the vertices with 5 edges, is constant and equal to 12, no matter the total number of points. This is, seemingly, an advantage for the icosahedron-seed. Very quickly as we increase the lattice point, the vast majority of sites connect to the same number of sites.

The number of vertices for each k-generation is

$$V_k = 12 + 10(4^k - 1). \tag{2.17}$$

This way, we can only construct lattices with specific number of vertices.

We have shown that both lattice constructions enable us to systematically vary the number of sites. Throughout the thesis, we will be interested in the scaling behavior of the systems defined on the lattices. We will scale up (down) the system by increasing (decreasing) the number of sites N. It is, then, important to clarify, what the scaling means geometrically. That is, what it means in terms of the nearest neighbor distances and the radius of the sphere, R.

If regular lattices could be constructed, there would be a well defined lattice constant, a, given by

$$a = \sqrt{\frac{4\pi R^2}{N}}. \tag{2.18}$$

This shows that there are three relevant quantities on the sphere; the R, the N and the a. We can do scaling with two equivalent approaches. We can choose to scale a as $\sim 1/\sqrt{N}$. In this case, R is kept constant. This makes the distribution of points on the sphere denser as system size is increased. So all lengths scales, like nearest neighbor distances, scale down with increasing system size. On the other hand, we can choose the radius to scale as

$$R \sim \sqrt{N}. \tag{2.19}$$

In this case, a remains constant. Since a is a local quantity, the local behavior of lattices of different sizes should be similar. We should note that we can go from one scaling approach to the other by simply multiplying the lengths and the radius with the correct power of N.

In our irregular lattices we cannot formally define a lattice constant. Nevertheless, we may again consider the quantity a as our lattices are reasonably uniform. Because of this, we expect lattices of different N to locally resemble each other. It, then, makes sense for a parameter like a to be relevant.

In the Fibonacci lattice, we mapped to the unit sphere, Eqs. (2.9). This approach corresponds to scaling a with system size keeping R constant. However, from now on, we will consider scaling as Eq. (2.19). This is because we want to directly compare local quantities of different lattices. In the next section, such local quantities will be the *NN* distances and the *NN* hoppings.

2.2 Tight-binding Laplacian on the sphere

The first system we will study is the free particle. This amounts to solving the Laplacian on our discrete spheres. The Laplacian is a rotationally invariant operator by definition. It is, then, useful to study it in order to establish the (approximate) spherical symmetry. In addition to that, the analytic solution for its spectrum on a sphere is well known. Thus, we can directly compare it to our numerical solution. This will be a way to decide

between our two candidate lattices. The lattice, for which the free particle exhibits a better spectrum, will be chosen.

The Hamiltonian of the free particle,

$$\mathrm{H}_{\mathrm{free}} = -\frac{\nabla^2}{2}, \tag{2.20}$$

is proportional to the Laplacian. The $\hbar$ and the mass have been set to 1. In solid state terms discretizing the Hamiltonian means constructing a tight-binding model. Each site i in our lattices is connected to neighboring sites, j. We denote the coordinates of the sites i, j by the vectors $\boldsymbol{r}_i, \boldsymbol{r}_j$. They extend from the center of the sphere to its surface. To implement the Laplacian, we use an arbitrary, smooth function f. The hopping terms J_{ij} of the tight-binding model are fixed through the following equation,

$$-\frac{1}{2}\nabla^2 f\Big|_{\boldsymbol{r}_i} = \mu_i f(\boldsymbol{r}_i) + \sum_{j\in NN} J_{ij} f(\boldsymbol{r}_j). \tag{2.21}$$

Essentially, the Laplacian acting on f at point i is expressed with respect to the value of f at i and at its neighbors j [3]. In order to find the coefficients J_{ij}, we Taylor expand each $f(\boldsymbol{r}_j)$ in Eq. (2.21) around $\boldsymbol{r}_i$. The expansion happens on the tangential plane of the sphere at point i, $(\perp_i)$. All the $3D$ vectors $\boldsymbol{r}_j - \boldsymbol{r}_i$ are projected on the $2D$ tangential plane $(\perp_i)$. The derivatives in the expansion are also meant to exist within the plane.

To illustrate the Taylor expansion, we denote the coordinates of the 2D plane $(\perp_i)$ as x_k, with $k = 1, 2$. We then have,

$$\boldsymbol{h}_{ij} = (\boldsymbol{r}_j - \boldsymbol{r}_i)_{\perp_i}, \tag{2.22}$$

$$f(\boldsymbol{r}_j) = f(\boldsymbol{r}_i) + \sum_{k=1,2} \frac{\partial f}{\partial x_k}\bigg|_{\boldsymbol{r}_i} h_{ij}^k + \frac{1}{2}\sum_{k,l=1,2} \frac{\partial^2 f}{\partial x_k \partial x_l}\bigg|_{\boldsymbol{r}_i} h_{ij}^k h_{ij}^l, \tag{2.23}$$

and

$$\nabla^2 f\Big|_{\boldsymbol{r}_i} = \frac{\partial^2 f}{\partial x_1 \partial x_1}\bigg|_{\boldsymbol{r}_i} + \frac{\partial^2 f}{\partial x_2 \partial x_2}\bigg|_{\boldsymbol{r}_i}. \tag{2.24}$$

We should note that $\boldsymbol{h}_{ij} \neq \boldsymbol{h}_{ji}$, because in Eq. (2.22) the tangent plane changes as well.

[3] This is similar to the familiar formula for the discretization of the second order derivative in one dimension,

$$\frac{d^2 f}{dx^2} \approx \frac{f(x+\Delta x) - 2f(x) + f(x-\Delta x)}{(\Delta x)^2} = t_1 f(x+\Delta x) + t_2 f(x) + t_3 f(x-\Delta x).$$

In this case, $t_1 = t_3 = \frac{1}{(\Delta x)^2}$ and $t_2 = -\frac{2}{(\Delta x)^2}$.

We substitute Eqs. (2.22), (2.23) and (2.24), back to Eq. (2.21). We demand that all the coefficients around the derivatives match between the left and right hand side. This way, for every site i, we get the conditions,

$$\sum_{j\neq i} J_{ij} + \mu_i = 0, \tag{2.25}$$

$$\sum_{j\neq i} J_{ij}\boldsymbol{h}_{ij} = 0, \tag{2.26}$$

$$\sum_{j\neq i} J_{ij}\boldsymbol{h}_{ij}\otimes\boldsymbol{h}_{ij} = -\mathbb{1}, \tag{2.27}$$

The zero order condition, Eq. (2.25), can be automatically satisfied for each i by just adjusting the value of μ_i. There are two first order conditions, Eq. (2.26), because the $\boldsymbol{h}$ are two dimensional vectors. There are three second order conditions implied through the matrix equation in Eq. (2.27). Therefore, the conditions we must set are, in total, 5.

These 5 conditions must be simultaneously satisfied for all lattice sites. Given that $J_{ij} = J_{ji}$, due to the Laplacian being real and symmetric matrix, the system of 5 equations of point i is not independent from the system of equations of any neighboring point j. Therefore, to evaluate the J_{ij} properly, one must solve a $5N$ linear system of equations. The total number of variables, M, of the system is equal to the total number of couplings J_{ij}. The system of equations is given in matrix form as

$$A\boldsymbol{x} = \boldsymbol{b}. \tag{2.28}$$

The A is a $5N\times M$ matrix. The first 5 rows correspond to site 1, the next 5 to site 2 and so on. Thus, for every site i, we have a $5\times M$ submatrix. In this submatrix, we fill the same number of columns as the total number of connections of site i. If, for example, site i connects to 6 neighbors, 6 columns are filled. The entries of each column are the distance elements $(h^1_{ij}, h^2_{ij}, h^1_{ij}h^1_{ij}, h^2_{ij}h^2_{ij}, h^1_{ij}h^2_{ij})$ as they appear in Eqs. (2.26) and (2.27). The j_s are the neighboring sites that connect to i.

For a specific neighbor l, we can arrange the k^{th} column to be the one with the il distance elements. Then, when we go to the submatrix of site l, we must again fill the k^{th} column. This is because $J_{il} = J_{li}$. This time, the elements must be $(h^1_{li}, h^2_{li}, h^1_{li}h^1_{li}, h^2_{li}h^2_{li}, h^1_{li}h^2_{li})$. As mentioned, the connections are different since $\boldsymbol{h}_{il} \neq \boldsymbol{h}_{li}$. In total, each column of A has ten elements, five for each connection.

The elements of the $\boldsymbol{x}$ vector are the J_{ij}. It follows, then, that the coupling J_{il} is placed on the k^{th} row of $\boldsymbol{x}$. The column vector $\boldsymbol{b}$ is given from the right hands side of Eqs. (2.26) and (2.27) and is equal to $(0, 0, -1, -1, 0)$, repeated N times. Having constructed the system, our goal is to solve for $\boldsymbol{x}$.

The Hamiltonian is given by

$$\mathrm{H}_{\mathrm{free}} = \sum_i \mu_i |i\rangle\langle i| + \sum_{<ij>} J_{ij} |i\rangle\langle j|, \tag{2.29}$$

in the position basis, $|i\rangle$. This is the tight-binding model for the free particle, where J_{ij} are the hopping terms and μ_i the on-site terms.

This construction can be implemented, in principle, for any geometry defined on the sphere. The geometry does not have to be triangulated. This means that we could also use the lattice shown on (b) in Fig. 2.2. The number of neighbors has to be sufficient so that the system of equations, Eqs. (2.26) and (2.27), or Eq. (2.28), can be solved. The neighbors should also be within a distance that justifies expanding up to 2nd order only.

We will assume that 2nd order is enough. It is straightforward to check if introducing more orders changes the results. We found that this is not the case. The problem we face is that the system of equations, is not, in general, exactly solvable. Specifically, the number of equations, $5N$, is larger than the number of hoppings (in reference to Eq. (2.28), $5N > M$).

The problem gets more constrained if we consider expanding to 3rd order. This will just increase the number of linear equations. Introducing more neighbors (intersecting edges), on the other hand, does increase the number of hoppings. However, this way, the distances between some points will be large. This might make the 2nd order expansion questionable.

In any case, one resorts to finding the *least squares* solution to Eq. (2.28), similarly to Ref. [20]. In practice, we assess the validity of the solution by looking at the energy spectrum, which is known to have degeneracy $2l + 1$. Also, due to the scaling behavior in Eq. (2.19) for the radius, the energy spectrum scales as

$$E \sim \frac{l(l+1)}{2} \frac{1}{N}. \tag{2.30}$$

In the spectrum plots, we will always rescale appropriately so that $E = \frac{l(l+1)}{2}$.

Therefore, we can directly put to the test the possible adjustments we described. First, we will decide between the triangulated Fibonacci sphere, such as (a) in Fig. 2.2, and the Fibonacci sphere with intersecting edges such as (b) in Fig. 2.2. To do that we have to consider multiple different realisations of the one with intersecting edges. To construct a lattice with intersecting edges we first define a distance ρ. We allow the points i to connect with all their neighbors j, for which $|\boldsymbol{r}_j - \boldsymbol{r}_i| \leq \rho$.

For every ρ, we solve the system of equations and identify the weakest hopping J_{ij}. We then erase this hopping and solve the system of equations again, with one hopping less. We continue this iteratively, for a sufficient number of erased hoppings. Then the

different configurations of the same ρ are compared. We pick the iteration with the best spectrum. Then, we proceed to a smaller ρ.

We assess the resulting spectra based on how degenerate the energy levels are and how close the ratio of the 2nd and 3rd energy levels is to $\frac{E_2}{E_3} = \frac{1}{3}$. In addition, since we use a least squares solver, we take into account the residual of the solutions. We concluded that the best spectra from this procedure essentially match the ones of the triangulated case.

Afterwards, we compare the spectra of the triangulated Fibonacci lattice and the $k = 1, 2, 3$-generation of the icosahedron-seed. In Fig. 2.6 we plot different number of eigenvalues for each size. The number of eigenvalues we plot suffices to distinguish the features of the two geometries. We want to see which construction's eigenvalues converge better to the free particle spectrum.

In order to understand the spectrums we see, we should explain some symmetry properties. The icosahedron (the 0-generation) is symmetric under 60 rotations. That is, there exist 60 rotations that map the polyhedron to itself. In group theory terms, the 60 rotations correspond to a group of order 60. This is called the icosahedral group, I [21]. It is also known from group theory that the irreducible representations of this group have dimensions $1, 3, 3, 4$ and 5.

Consider a physical system placed on the icosahedron uniformly. It has icosahedral symmetry. Therefore, its spectrum should exhibit $1, 3, 3, 4$, or 5-fold degeneracies accordingly. If we were to compare these numbers with the degeneracies of the $SO(3)$ group, then we see that they correspond in number to $l = 0, 1$ and 2. The 4-fold icosahedral degeneracy is not part of the $SO(3)$ degeneracies. Also the icosahedral degeneracies are limited to a maximum of 5. This is not the case for $SO(3)$ since l can take any, non-negative integer, value such that all odd integers can serve as degeneracies.

The new vertices, for each k, are introduced symmetrically on each face. So, the icosahedron-seed does not have additional symmetries. Here, we essentially examine if it is the free particle solution, that can make the icosahedron-seed overcome the icosahedral symmetry. In Fig. 2.6 the generations of the icosahedron do not seem to overcome it. For example, we can see no 7-fold degeneracy appearing on the 4th energy level. We see a 3-fold and and 4-fold essentially exact degeneracy, which are two of the icosahedral degeneracies.

In comparison, the Fibonacci lattice showcases the correct degeneracies for low energies, even in the cases where they are more approximate. This is especially true for $N = 142$ and 642. This happens while the Fibonacci lattice, as a geometry, does not exhibit symmetries. So, there is no symmetry to overcome when solving the free particle problem. The (approximate) $SO(3)$ symmetry emerges quickly with increasing system size. The convergence results, thus, indicate that we should work with the Fibonacci lattice.

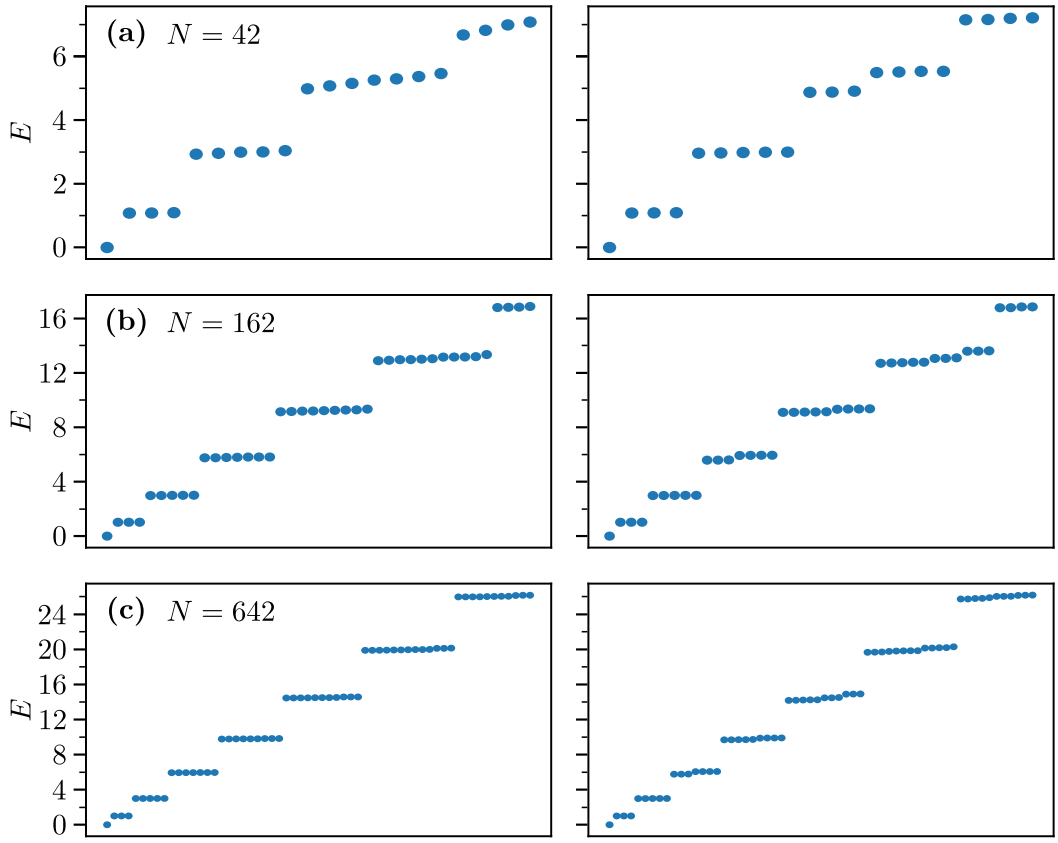

Figure 2.6: Comparison of free particle spectrum between the Fibonacci lattice and the generations of the icosahedron-seed. (a) The 20 lowest energies are shown for $N = 42$. The third energy level, at around $E = 3$, exhibits an approximate (or quasi-) degeneracy for the Fibonacci lattice. The degeneracy for this level in the 1-generation is an essentially exact 5-fold, which follows from the icosahedral degeneracies. Its fourth energy level has a visible gap. This gap separates the energies to the essentially exact 3-fold and 4-fold degeneracies, which are also part of the icosahedral degeneracies. (b) The 40 lowest eigenenergies are shown for $N = 162$. The Fibonacci spectrum exhibits correct (approximate) degeneracies even beyond the third energy level ($E = 3$). For $E > 3$, we observe small gaps within the energy levels of the 2-generation. Again, the energy levels separate into icosahedral degeneracies. (c) The 60 lowest eigenenergies are shown for $N = 642$. The Fibonacci lattice exhibits correct degeneracies for the energy levels shown. In comparison gaps persist for the 3-generation even for the fourth energy level.

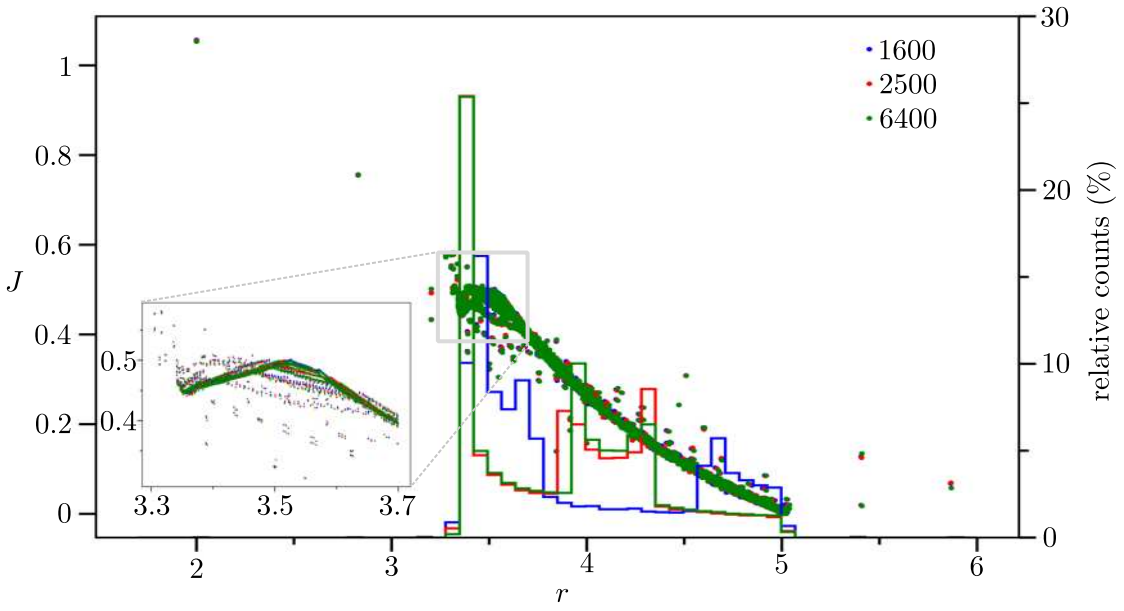

Figure 2.7: Behavior of hoppings with distance for the triangulated Fibonacci lattice. The scattered plots mostly fall on top of each other. Hence, the J have very similar r-dependence for all system sizes. The histograms, y-axis on the right, count the relative number of times a specific distance appears on the lattice. There appear statistically insignificant distances for $r \lesssim 3$ and $r \gtrsim 5.2$. They exist because $J(r)$ is plotted for the lattice variation with a point on the north pole and no point on the south pole. This corresponds to $\varepsilon = 0$ in Eq. (2.15). The point on the north pole is very close to its neighbors. The lack of a point on the south pole explains the large distances. As we progressively increase ε, less and less such distances appear. The inset figure indicates that for the regions around $r \sim 3.5$, there is substantial variance in the value of J, for all sizes, with respect to r and a non-monotonous trend.

2.3 Free particle on the Fibonacci lattice

Having chosen the Fibonacci lattice and seen that its spectrum better approximates the $SO(3)$ degeneracies, we study it further. It is of interest to examine how the hoppings J, as they appear in Eq. (2.29), vary with distance. In Fig. 2.7, we show scatter plots of all the J_{ij} against the respective $r = |\boldsymbol{r}_j - \boldsymbol{r}_i|$. We observe that for different system sizes the trend of $J(r)$ is very similar, i.e the scattered plots mostly fall on top of each other.

The histograms in the background of Fig. 2.7 denote the relative number of times a distance r appears between neighbors. The percentages vary for different N. If we assume that a single value r corresponds to only one $J(r)$, then the percentages also explain the frequency in which $J(r)$ appear for different N. However, this correspondence seems to

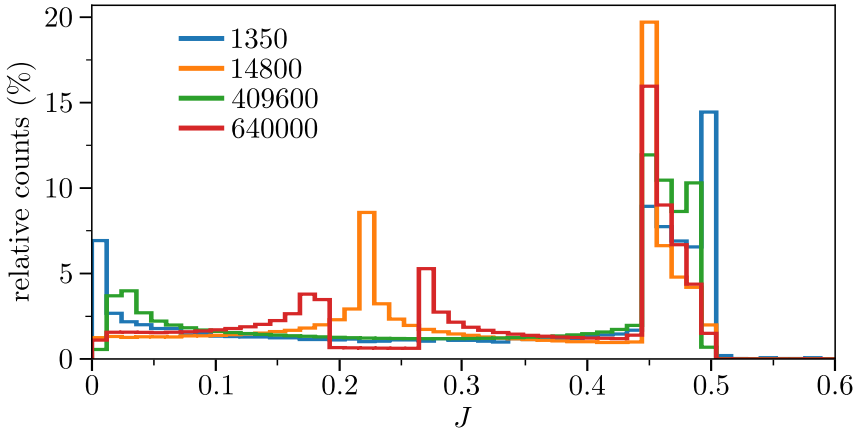

Figure 2.8: Histogram for the frequency in which J appear in the system. For all system sizes, the $J > 0.44$ appear more frequently. However, other J are prominent as well, as indicated by the smaller peaks. The position of these peaks varies considerably with system size.

be more reliable in the tail of $J(r)$. More specifically, for smaller r, we see high variance in the value of J, as indicated by the inset plot of Fig. 2.7.

We, also, note the appearance of the statistically insignificant distances, $r \lesssim 3$ and $r \gtrsim 5.2$, in Fig. 2.7. They exist because we plot $J(r)$ for a variation of the lattices with a point on the north pole and no point in the south pole. This corresponds to $\varepsilon = 0$ in Eq. (2.15). The point on the north pole is very close to its neighbors. The lack of a point on the south pole explains the large distances. As we progressively increase ε, less and less such distances appear.

In order to properly evaluate the J, we use a different histogram plot, shown in Fig 2.8. We count the number of times the values of J appear. This is plotted irrespective of the corresponding distance r. For all system sizes, we see highest percentages for the large values of J, $J > 0.4$. The behavior, on smaller values than that, varies significantly as we increase the system size. As explained in Fig. 2.7 this is attributed to the underlying lattice structure. More specifically, the percentages of NN distances vary accordingly.

As we increase the N, the position of the smaller peaks oscillate. We can roughly say that they oscillate between the two configurations shown in Fig. 2.9. We refer to configurations with a peak either at the center (continuous arrow) of the histogram or a peak at very low J (dashed arrow). Astonishingly, the "period" of the oscillation seems to be related to the golden ratio, Φ (see Eq. (2.3)). In particular, a system of size N has very similar distribution for the J as a system of size $\Phi^2 N$ [4].

When scaling up the system, it would make sense to compare different sizes where the

[4]Of course, by $\Phi^2 N$ we mean the closest integer to that number.

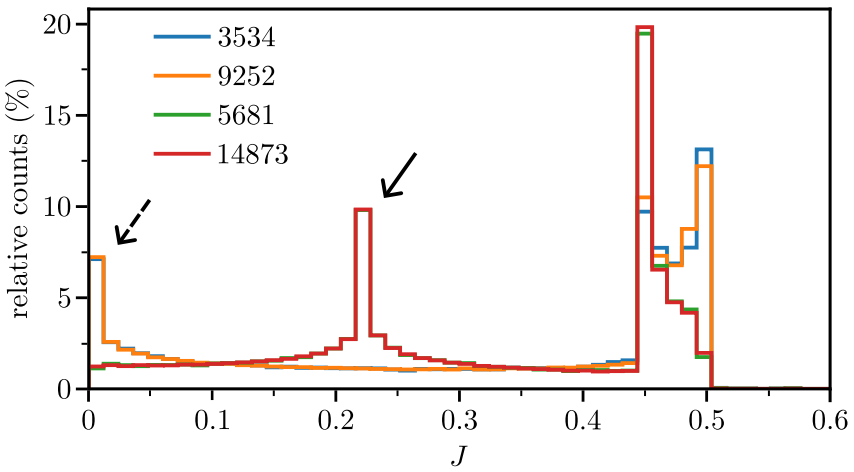

Figure 2.9: Histogram of J illustrating two distinct configuration types for the smaller peaks in J. For one configuration type, we have a smaller peak approximately at the center of the figure (continuous arrow). This corresponds to the sizes 5681 and 14873. For the other configuration type, the smaller peaks are placed at very small J (dashed arrow). This configuration type corresponds to sizes 3534 and 9252. Note that for the same configuration type, the two sizes are N and $\Phi^2 N$. Φ is the golden ratio and it is given by Eq. (2.3). As we vary the system size arbitrarily, the positions of the smaller peaks oscillate between the peaks in the two configurations shown here.

behavior of the J is similar. Nevertheless, for all N, the hoppings were used to explicitly construct the Laplacian. We saw no particularity in the spectrum of the free particle that can be attributed to different J distributions. Therefore, when it comes to evaluating the free particle for different system sizes, we will not take this thought into consideration. This line of thinking will be relevant for the spin system where we will, again, use these hoppings.

The last component in the evaluation of the free particle is to assess which Fibonacci lattice perturbation to use. We can compare how the J behave for the different perturbations. We will study the different ε of Eq. (2.15) and the configuration of Eq. (2.16) with points on both poles. Figure. 2.10 shows how perturbations differ for the system sizes $N = 450$, 1178, and 3084. These sizes are related by the multiplicative constant Φ^2 and have very similar behavior for the J. The figures indicate that variations in J become less prominent with system size. The position of the peaks in the histograms effectively does not change due to different perturbations, for any system size.

We should note that the configuration with points on both poles as well as ones with small ε include some $J > 0.6$, which are not shown. This is explained in our previous statement on Fig. 2.7; there is a statistically insignificant number of small distances if we include points near or on the poles. Therefore, as shown in Fig. 2.7, there is a statistically insignificant number of J with large values.

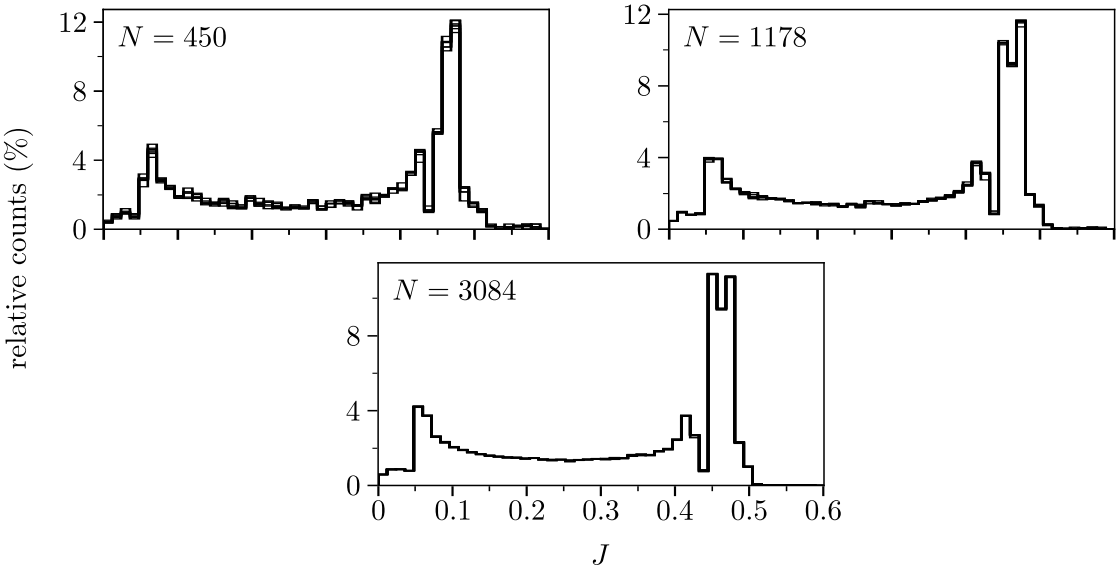

Figure 2.10: Histograms of J for different implementations of the Fibonacci lattices, for $N = 450, 1178$, and 3084. These system sizes differ by the multiplicative constant Φ^2 and have similar behavior for the J. The different perturbations correspond to $\varepsilon = 0, 0.1, ..., 0.5$ in Eq. (2.15) and to the configuration of Eq. (2.16) with points on both poles. The differences in the perturbations become less prominent with system size. The positions of the peaks in the histograms essentially do not change for the different perturbations, for any system size. We should note that the configuration with points on both poles, as well as ones with small ε, include some $J > 0.6$, which are not shown. This is because there is a statistically insignificant number of small distances if we include points very near or on the poles. Therefore, there is a statistically insignificant number of J larger than 0.6 as shown in Fig. 2.7.

Furthermore, in Fig. 2.11, we plot the spectrum for $N = 20$, for $\varepsilon = 0$ and $\varepsilon = 0.5$. The $\varepsilon = 0.5$ exhibits a slightly better approximate 3-fold and 5-fold degeneracy energy for the second and third energy level. Nevertheless, as we increase the system size the differences on the spectra decrease. Therefore, to resolve the optimal configuration would be tedious. Instead of comparing multiple energy levels, we can compare the residuals of the least squares solutions of Eq. (2.28). The residual is given by the norm of $\boldsymbol{b} - A\boldsymbol{x}$, where x is the least squares solution.

Comparing the residuals may be applicable in this case, because we solve for very similar systems. Therefore, the second order expansion should be similarly justified. The residuals for various ε are shown in Table 2.3. We see that the residuals get smaller as we increase ε. This is consistent for all system sizes N we have tried. Albeit the small decrease of the residuals, this argumentation also motivates the choice of larger ε.

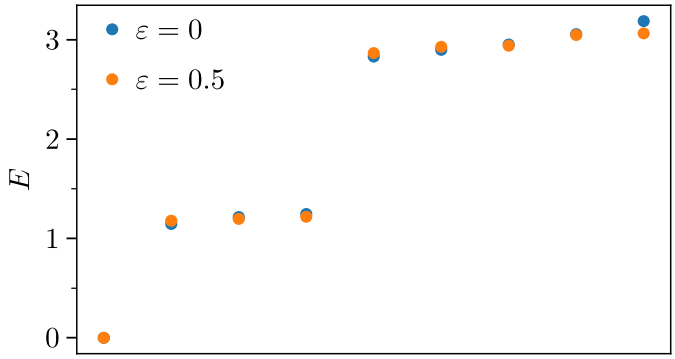

Figure 2.11: Spectrum of Fibonacci lattice perturbations with $\varepsilon = 0$ and $\varepsilon = 0.5$, for $N = 20$. The x-axis is not physical, it is just the indexing of the eigenvalues. The first 9 eigenvalues are plotted for each ε. We observe that the spectrum of $\varepsilon = 0.5$ appears slightly more degenerate in the second and third energy level.

2.4 Rotations and geometric constraints

If we can sensibly define angular momentum operators, L^x, L^y and L^z, then we can implement rotations. In particular, with these operators we can implement rotations for all one-particle problems defined on the sphere. The rotation operator around the z-axis is e^{iL^z}.

For the free particle we first construct the momentum operators,

$$\boldsymbol{p} = i[\mathrm{H}_{\mathrm{free}}, \boldsymbol{r}]. \tag{2.31}$$

This follows since $\mathrm{H}_{\mathrm{free}} \approx \dfrac{\boldsymbol{p}^2}{2}$. The angular momentum operators are given by

$$L = \boldsymbol{r} \times \boldsymbol{p}. \tag{2.32}$$

$\boldsymbol{\varepsilon}$	**Residuals** $\cdot\, 10^2$
P	9.74
0	9.89
0.1	9.19
0.2	9.04
0.3	8.76
0.4	8.53
0.5	8.48

Table 2.1: Residuals for different perturbations of the Fibonacci lattice at $N = 100$. The P denotes the configuration with points on both poles given by Eq. (2.16). The ε are the ones in Eq. (2.15).

The $\boldsymbol{r}$ are exactly known to us as the sphere was explicitly constructed. In addition, we can quantify up to which l subspace the L^x, L^y and L^z are good. Namely, how well they satisfy the commutation relations of the angular momentum algebra. We can, also, compare their eigenvalues to the exact ones.

Implementing rotations through angular momentum operators is one way to go. The other way would be through permutations of the vertices. However, we cannot claim there exists a permutation of the lattice sites that corresponds to a rotation. This is because of how the points allocate on the Fibonacci lattice. There is, actually, no rotation (around any axis) that maps our lattice back to itself.

However, the construction of the Fibonacci lattice allows us to define a permutation that approximately does that. To see this, we again consider the Fibonacci lattice on a unit square, Fig. 2.4. The x coordinate is linearly related to the φ angle around the z-axis of the sphere. So, translating the vertices along the x-axis in the square, with periodic boundary conditions in the x direction, corresponds to moving around the z-axis on the sphere.

We, now, have to find how much we should x-translate in order to have the best, albeit approximate, mapping of the sphere back to itself. First, we mesh the y axis in equal segments (see Fig. 2.12). We, then, translate all the points of the lattice by a unique value Δx. We have to find the Δx for which there is a minimum x-distance, between the translated (red) and the original vertices (blue) in Fig. 2.12. We only compare blue and red points within the same segment. Then, each red point is matched to a neighboring blue one. The matching procedure does not allow for a red point to match to its original blue point. It, also, does not allow for two red points to match to the same blue point.

In general, we have to fine-tune the number of segments we want. Also, we should take into account that the allocation of points along the x-axis is dictated by the golden angle. As discussed in the first section, this establishes a good uniform distribution. Since each segmented block contains $\sqrt{N} = 8$ points in Fig. 2.12, the translation constant Δx should be $\Delta x \sim \frac{1}{\sqrt{N}}$.

A more physical way to find the best angle is to act with the possible permutations on the eigenstates we found for $\mathrm{H}_{\mathrm{free}}$. In the ideal case, the permutation, $\mathcal{R}$, should act on our spherical harmonics as

$$\mathcal{R}|lm\rangle = e^{im\varphi}|lm\rangle. \tag{2.33}$$

So, we assess how good a permutation is by how many m quantum numbers we can distinguish from those phase factors. Eventually, we concluded that the best angle is

$$\varphi \approx \frac{2\pi}{\sqrt{N}}. \tag{2.34}$$

In this case we divided the y-axis in $L = \sqrt{N}$ segments.

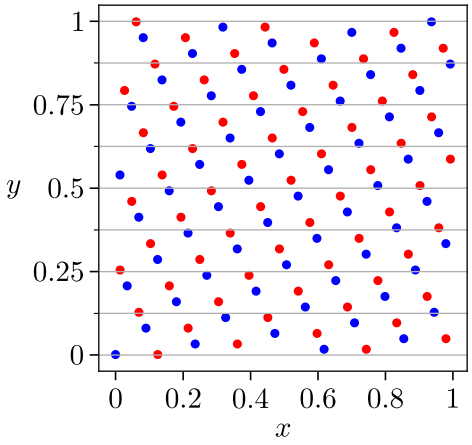

Figure 2.12: Permutations along the x-direction on the unit square lattice for $N = 64$. By blue we denote the original Fibonacci lattice on a unit square and by red the permuted one. We have segmented the y-axis in 8 segments and translated by $\Delta x = \frac{2\pi}{8}$ in the x-direction.

The optimal angle being $\varphi \approx 2\pi/\sqrt{N}$, gives an estimate for how many energy levels we can discern on the free particle spectrum. More specifically, we notice that

$$\exp\left\{im\frac{2\pi}{\sqrt{N}}\right\} = \exp\left\{i\left(m \pm \sqrt{N}\right)\frac{2\pi}{\sqrt{N}}\right\}, \tag{2.35}$$

while it is known that $-l \leq m \leq l$. Therefore, for the energy level with $l \approx \sqrt{N}/2$, we would not be able to distinguish between $m \approx -\sqrt{N}/2$ and $m \approx \sqrt{N}/2$. Evidently, the inability to distinguish the m becomes more pronounced when $l > \sqrt{N}/2$. For this reason, we cannot claim that we can resolve between eigenstates corresponding to energy levels with $l \gtrsim \sqrt{N}/2$. This argument is reasonably justified in Fig. 2.13. There, we can distinguish approximately $\frac{\sqrt{N}}{2} + 1$ energy levels for each system size, although not all of them are sufficiently degenerate. To avoid further confusion, we clarify that we count the energy levels by considering the $E = 0$ as the first energy level.

So, this constraint follows from the optimal angle and is therefore geometric. Besides illuminating how geometry affects the spectrum, permutations will be used in the interacting system as well. There, we cannot define generators of spatial/lattice rotations. The only way to discern between angular momentum subspaces in the energy spectrum, is to implement permutations.

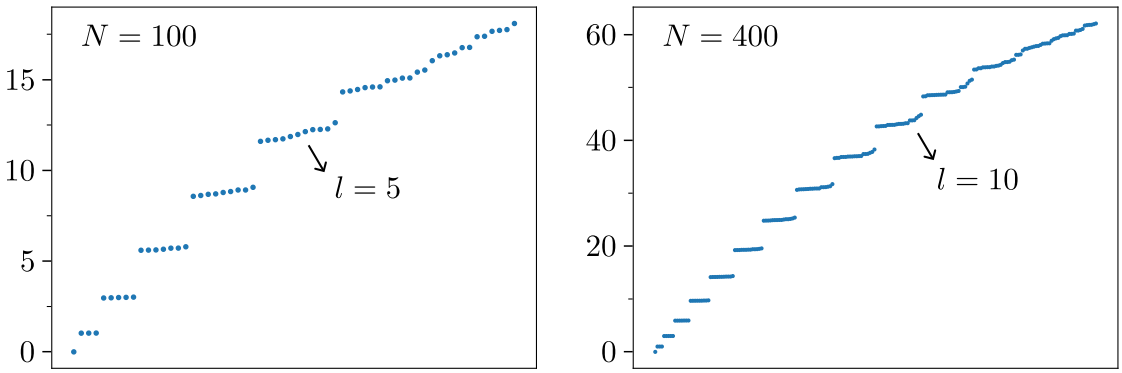

Figure 2.13: Resolution of energy levels for the spectra of triangulated Fibonacci lattices. We can distinguish energy levels although they are only approximately degenerate. For both $N = 100$ and $N = 400$ we can discern energy levels approximately up to the $\sqrt{N}/2 + 1$ energy level. This corresponds to the energy level of the free particle with $l = \sqrt{N}/2$. This limit in our resolution is imposed by the underlying geometry. There is a minimum angle, $\theta \approx 2\pi/\sqrt{N}$, with which the lattice can be rotated to, approximately, map back to itself. For two eigenstates within the same energy level we cannot distinguish the quantum numbers m, if they differ by $\sqrt{N}$ due to Eq. (2.35). Eigenstates with such eigenvalues for m would appear at the $l = \sqrt{N}/2$ energy level and beyond. It is after this level in our spectrum plots, where we claim that we cannot visually distinguish the energy levels anymore.

Chapter 3

Transverse-field Ising model at criticality

In this chapter, we give a brief overview of the quantum phase transition of the transverse-field Ising model (TFIM). We start by motivating how symmetry breaking of the $\mathbb{Z}_2$ symmetry could lead to an ordered state. This symmetry breaking is intimately tied with the degeneracy of the ground state energy. To illustrate this degeneracy and gain a quantitative picture, we will look at the energy spectrum of transverse-field Ising chain. This $d = 1$ dimensional model has also been analytically solved.

Furthermore, we will discuss the transfer matrix method of mapping the d-dimensional quantum Ising model to a corresponding $(d + 1)$-dimensional classical one. This correspondence between d quantum and $(d + 1)$ classical enable us to carry over arguments of classical phase transitions to the quantum problem. To that regard, being formulated through transfer matrices, it explains how correlation lengths of the classical model, and their scaling with system size, connect to the energies of the quantum model.

The scaling of quantities with system size, or else finite-size scaling, is relevant to understand if one wants to treat numerical problems, where the systems are necessarily finite. The basic, heuristic, finite-size scaling theory for classical systems is discussed. It is explained in connection to the renormalization group (RG) theory. The relevant components of RG are only partially explained in App. D, since an exhaustive detailing of them goes beyond the scope of this thesis.

Lastly, conformal symmetry will be discussed. At the critical point, a system might exhibit not only scale invariance but, also, be symmetric under the more general conformal transformations. The one dimensional TFIM, for example, is analytically known to exhibit such a symmetry [22]. However, in a dimension higher, predictions, due to this symmetry, have only been numerically verified [23], [16]. Said predictions also relate to finite-size scaling predictions for systems placed on $S^{d-1} \times \mathbb{R}$ geometries. As we will

see, this showcases the relevance of studying the TFIM on a sphere, S^2. Conformal symmetry is explained more in depth in App. B.

3.1 Symmetry Breaking

Conisder the TFIM Hamiltonain given by

$$\mathrm{H} = -J \sum_{\langle ij \rangle} S_i^x \otimes S_j^x - h \sum_i S_i^z, \tag{3.1}$$

where the $\langle ij \rangle$ indicate nearest neighbor interactions. The two-spin interaction term is the ferromagnetic interaction, where $J > 0$. The transverse field term is, in this case, given in the z direction with $h > 0$. Also, here, $S_i^{x,y,z} = \frac{1}{2}\sigma_i^{x,y,z}$, where the σ are the Pauli matrices.

The Hamiltonian commutes with the $\mathbb{Z}_2$ operator

$$\mathcal{P} = \prod_i \sigma_i^z. \tag{3.2}$$

Due to the properties of this operator, $\mathcal{P}^2 = 1$ and $\mathrm{Tr}(\mathcal{P}) = 0$, its eigenvalues are ± 1 and the positive are equal in number to the negative ones. Because of $[\mathcal{P}, \mathrm{H}] = 0$, the space of eigenstates of the Hamiltonian is naturally divided to two $\mathbb{Z}_2$ subspaces.

In this section, we will discuss when an ordered ground state can appear in the system. An ordered ground state, $|0\rangle$, is one for which the *order parameter*, $\langle 0|S_i^x|0\rangle$, is non-zero. The ground state is the relevant one when we care about $T = 0$. In general, an ordered state appears due to a quantum phase transition, which occurs as we tune the parameter h in Eq. (3.1). More specifically, there are different regimes depending on the value of h.

For very large h, the transverse field term dominates in Eq. (3.1). This indicates a configuration for the ground state where all the spins are parallel in the z direction. On the other hand, at very small h, the ferromagnetic term is dominant. It would, then, be suggestive to say that the ground state has all spins aligned in the "up" or "down" x direction ($|\rightarrow\rangle$ or $|\leftarrow\rangle$). However, such a state would not be an eigenstate of $\mathcal{P}$. The ground state which has a definite $\mathbb{Z}_2$ number should be a superposition of the states aligned in either of the x directions.

As long as there is no symmetry breaking of $\mathbb{Z}_2$, that is all allowed physical states are eigenstates of $\mathcal{P}$, there can be no ordered state. To see this, consider a state $|\Psi\rangle$ for which

$$\mathcal{P}|\Psi\rangle = \pm|\Psi\rangle \tag{3.3}$$

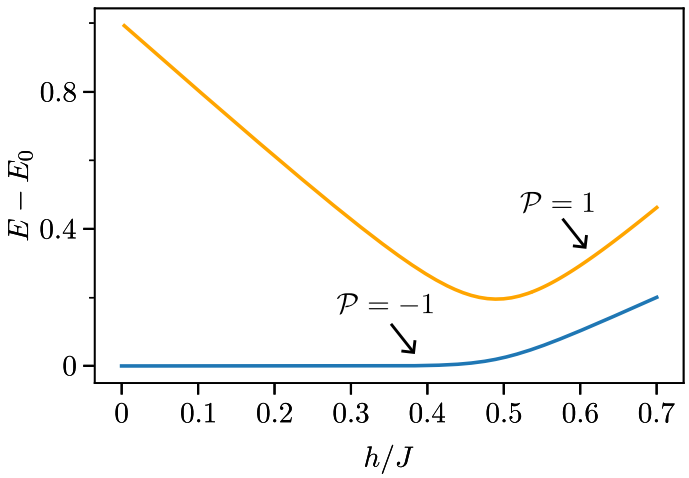

Figure 3.1: First excitations of the finite transverse-field Ising chain. The number of sites in the chain is 16. The ground state E_0 belongs to the even $\mathbb{Z}_2$ sector ($\mathcal{P} = 1$). The first excited state, $E_1^{\mathcal{P}=-1}$, belongs to the odd subspace and its energy essentially lies on top of the ground state as h/J is decreased. The $E_1^{\mathcal{P}=1}$ is the first excited state that belongs to the even subspace. At the critical point, $h = 0.5J$, both these energies become degenerate with the ground state energy in the infinite system.

and

$$\mathcal{P} S_i^x \mathcal{P} = -S_i^x. \tag{3.4}$$

Therefore, $\langle\Psi|S_i^x|\Psi\rangle = -\langle\Psi|\mathcal{P}S_i^x\mathcal{P}|\Psi\rangle = -\langle\Psi|S_i^x|\Psi\rangle$, which yields

$$\langle\Psi|S_i^x|\Psi\rangle = 0. \tag{3.5}$$

The symmetry breaking, thus, makes sense when two eigenstates of different parity have the same energy. In that case, a superposition of the two should be allowed in the statistical physics sense, given that the resulting state also minimizes the free energy (which is just the energy at $T = 0$). So, for the TFIM to have an ordered state, we should not be able to distinguish the two lowest energy eigenvalues. These eigenvalues must also belong to different subspaces of $\mathcal{P}$.

In Fig. 3.1, we plot the energies of the lowest excitations ($E - E_0$) of the transverse-field Ising chain against the transverse field h. We annotate the subspace of $\mathbb{Z}_2$ each of them belongs to. The first excited state belongs to a different $\mathbb{Z}_2$ subspace than the ground state. The energy of this state is, $E_1^{\mathcal{P}=-1}$ and progressively overlaps to E_0 as h decreases.

In fact, we know from the analytical solution of the transverse-field Ising chain [24], that for the infinite system, $E_1^{\mathcal{P}=-1}$ and $E_1^{\mathcal{P}=1}$ become equal to E_0 at $h = 0.5J$[1]. This is the critical point of the system. For $h \leq 0.5J$, an ordered state appears due to

[1]The usual $h = J$ as it appears in [24] is applicable when we consider the Hamiltonian with the Pauli spin matrices.

$E_1^{\mathcal{P}=-1} = E_0$ in the infintite system. Even though the analytical solution exists only for the one dimensional chain, the same reasoning applies to higher dimensions. Within the context of the thesis, where we place the TFIM on a sphere, we are interested in the two dimensional case.

As we will discuss in the next section, we can explain the d-dimensional TFIM by mapping it to a $(d+1)$-classical Ising system. This enables one to explain the quantum phase transition in terms of the corresponding classical one in $(d+1)$ dimensions. In the classical case, the second order phase transitions formally only appears in infinite systems. Therefore, we know that, even though Fig. 3.1 does suggest a degeneracy for low h at the finite system, true degeneracy and symmetry breaking may happen on the infinite TFIM.

3.2 Quantum to Classical Mapping

To show the mapping of the quantum model to the classical one of one dimension higher, we will consider a more general TFIM Hamiltonian,

$$\mathrm{H} = -\sum_{ij} J_{ij}\sigma_i^x \otimes \sigma_j^x - h\sum_i \sigma_i^z. \tag{3.6}$$

The nearest neighbor couplings might differ from each other. We, also, chose to use the σ matrices for ease of calculations (no prefactors) in the following.

The mapping to the classical system comes about in the evaluation of the partition function of the quantum system,

$$Z = \mathrm{Tr}(e^{-\beta \mathrm{H}}). \tag{3.7}$$

The idea of the mapping is that we can treat the partition function as a classical partition function calculated through an effective classical Hamiltonian (action). For the derivation we follow [17] and [25]. We, first, discretize $e^{-\beta \mathrm{H}}$,

$$e^{-\beta \mathrm{H}} = e^{-\delta\tau \mathrm{H}} e^{-\delta\tau \mathrm{H}} e^{-\delta\tau \mathrm{H}} e^{-\delta\tau \mathrm{H}} \ldots, \tag{3.8}$$

where each temperature step is denoted by $\delta\tau$ and the total number of them is $M = \frac{\beta}{\delta\tau}$. Each exponential in Eq. (3.8), is known as the *transfer matrix*,

$$T = e^{-\delta\tau \mathrm{H}}. \tag{3.9}$$

Making $\delta\tau$ very small we can justify the following,

$$\exp\left(-\delta\tau \mathrm{H}\right) = \exp\left(\delta\tau \sum_{ij} J_{ij}\sigma_i^x \otimes \sigma_j^x\right) \exp\left(\delta\tau h \sum_i \sigma_i^z\right) + O(\delta\tau)^2. \tag{3.10}$$

We introduce completeness relations in the product of operators, Eq. (3.8), within the trace of partition function,

$$Z = \mathrm{Tr}\left(e^{-\delta\tau \mathrm{H}} \sum_{\{\sigma^x_{i,1}\}} \left|\{\sigma^x_{i,1}\}\right\rangle \left\langle\{\sigma^x_{i,1}\}\right| e^{-\delta\tau \mathrm{H}} \sum_{\{\sigma^x_{i,2}\}} \left|\{\sigma^x_{i,2}\}\right\rangle \left\langle\{\sigma^x_{i,2}\}\right| e^{-\delta\tau \mathrm{H}} \dots \right). \quad (3.11)$$

The $\{\sigma_{i,m}\}$ indicate a many spin state, where spins are placed on all lattice sites i. Therefore, in this formula i does not indicate a single spin site. It is just there to show that, essentially, for all m the same type of summation happens. The additional indexing starts from $m = 0$ and goes up to $m = M - 1$. The summation over $\{\sigma_{i,0}\}$ is enforced via the trace. Also, due to the trace we take $\left|\{\sigma^x_{i,0}\}\right\rangle = \left|\{\sigma^x_{i,M}\}\right\rangle$, which explains the numbering up to $M - 1$.

Investigating each of the terms up to order $\delta\tau$, Eq. (3.10), we have

$$\left\langle\{\sigma^x_{i,m}\}\right| \exp\left(-\delta\tau \mathrm{H}\right) \left|\{\sigma^x_{i,m+1}\}\right\rangle = \left(\prod_{k=1}^{N} \left\langle\sigma^x_{k,m}\right| \exp\left(\delta\tau h \sigma^z_k\right) \left|\sigma^x_{k,m+1}\right\rangle \right) \times$$
$$\times \exp\left(\delta\tau \sum_{\langle ij\rangle} J_{ij} s_{i,m} s_{j,m} \right). \quad (3.12)$$

The ferromagnetic interacting term is expressed in the same basis as the completeness relation. Therefore, it becomes a number. More specifically, the $s_{i,m+1}$ are now numbers that take the values ± 1. The product up to N corresponds to the sum in the transverse direction in Eq. (3.10). The curly brackets are dropped because, due to the product, we can use states $|\sigma_{k,m+1}\rangle$ defined on a single site, k.

Using $\exp\left(\delta\tau h \sigma^z_k\right) = \sigma^z_k \sinh h\delta\tau + \cosh h\delta\tau$, $\sigma^z|{\rightarrow}\rangle = |{\leftarrow}\rangle$, and $\sigma^z|{\leftarrow}\rangle = |{\rightarrow}\rangle$, we eventually get

$$\langle\sigma^x_{k,m}| \exp\left(\delta\tau h \sigma^z_k\right) |\sigma^x_{k,m+1}\rangle = A \exp\left(B s_{k,m} s_{k,m+1}\right). \quad (3.13)$$

Here, $A = \sqrt{\sinh h\delta\tau \cosh h\delta\tau}$ and $B = -\frac{1}{2}\ln\left(\tanh h\delta\tau\right)$. The Eq. (3.13) might seem complicated. However, everything follows from the consideration that the $s_{k,m}$ and $s_{k,m+1}$ only take the values ± 1 and from a simple substitution one can do for each combination of the values of $s_{k,m}$ and $s_{k,m+1}$.

Substituting Eq. (3.13) into Eq. (3.12) we get,

$$\left\langle\{\sigma^x_{i,m}\}\right| \exp\left(-\delta\tau \mathrm{H}\right) \left|\{\sigma^x_{i,m+1}\}\right\rangle = A^N \exp\left(B \sum_k s_{k,m} s_{k,m+1} + \delta\tau \sum_{\langle kl\rangle} J_{kl} s_{k,m} s_{l,m} \right). \quad (3.14)$$

Making the final substitution into the partition function, Eq. (3.11) we get

$$Z = \sum_{\{s\}} A^{NM} \exp\left(B \sum_{k,m} s_{k,m} s_{k,m+1} + \delta\tau \sum_{\langle kl\rangle,m} J_{kl} s_{k,m} s_{l,m} \right). \tag{3.15}$$

Here the physical indexes (k and l) are summed up to N, and the m are summed up to M. We see from Eq. (3.15), that we can consider an effective classical Hamiltonian,

$$\mathrm{H_{cl}}\left(\{s\}\right) = -B \sum_{k,m} s_{k,m} s_{k,m+1} - \sum_{\langle kl\rangle,m} \delta\tau J_{kl} s_{k,m} s_{l,m}, \tag{3.16}$$

for which $Z \propto \sum e^{-\mathrm{H_{cl}}(s)}$. Therefore, we can calculate the partition function by summing over all possible configurations $\{s\}$. In this interpretation, the spins sit on a bigger lattice which extends also in the time dimension and at each time slice (step) there is an identical copy of the physical lattice (k indexing). The lattice constant in the time direction is $\delta\tau$ and the interaction term in that direction is given by B.

In turn, the $M = \frac{\beta}{\delta\tau}$ is the thickness of the time direction (the time slices over which we sum). We should note that the equivalence to this classical description relies on $\delta\tau$ being small, as seen in Eq. (3.10). However, we need to examine how to take $\delta\tau \to 0$ in Eq. (3.15), as there might be irregularities. Firstly, the overall constant depends on M and hence on $\delta\tau$.

We can argue, however, that is not physically important since in calculating physical quantities, such as the correlation functions, the constants drop out since Z appears also on the denominator of the calculations. Furthermore, we observe that the lower the $\delta\tau$, the interaction in the time direction, B, dominates over the vanishing interaction $\delta\tau J$. Lastly, there is the limit of the summation in the time direction, M, which for small $\delta\tau$ should be large but finite (depending on the value of β).

We are interested in the mapping that adds an infinite dimension to the system and does not have these divergences. Then $\delta\tau$ should be finite, in a manner where Eq. (3.10) is satisfied, and take $M \to \infty$. This can, then, only happen when also $\beta \to \infty$ [2]. So, a quantum model defined on d dimensions maps to a classical model defined on $d+1$ dimensions. Henceforth, we will make the distinction between the d dimensions of the quantum model and the $d+1$ dimensions in the equivalent classical model, by denoting $D = d + 1$.

In the context of conformal symmetry and finite-size scaling, we will be interested in correlation functions of observables separated in the time direction. Examples of these

[2] Nevertheless, this introduces another subtlety in the process, since the condition on $\delta\tau$ from Eq. (3.10) actually scales with the size of the quantum system as $1/\sqrt{N}$. So $\delta\tau$ should, also, go to zero, as N is increased. Therefore, we should be careful in the order we take the limits. We should note that this is not obviously alleviated even if we did the quantum to classical mapping by directly using the formal Trotter's formula (as done here [26]), where we directly treat $M \to \infty$. The reason for that is that it applies to bounded operators and we would have multiplied our operators by the infinite β.

are correlation functions of the spin $\langle s_{j,0}s_{i,n}\rangle$ and of the energy density ε. The spins, here, have two components, as they are the classical spins that appear in Eq. (3.16) which exist both in the space and time direction. Since we calculate the quantities in the quantum system, we have to see which trace averages correspond to these correlation functions.

Using the transfer matrix (Eq. (3.9)), we get the following equality,

$$\begin{aligned}\frac{1}{Z}\mathrm{Tr}\Big(T^{M-n}\sigma_j^x T^n \sigma_i^x\Big) &\sim \frac{1}{Z}\sum_{\{s\}} s_{j,0}s_{i,n}\exp\left(-\mathrm{H_{cl}}\right)\\ &= \langle s_{j,0}s_{i,n}\rangle. \end{aligned} \tag{3.17}$$

It is straightforward to confirm the first line, since it is essentially the same process as for the evaluation of the partition function. The basis we chose for the trace and the completeness relation insertions is this of σ^x, so the operators act trivially on it. The right hand side of Eq. (3.17) is actually the classical correlation function of two spins, $\langle s_{j,0}s_{i,n}\rangle$.

The Eq. (3.17) holds as long as the quantum to classical mapping is valid. This implies that the temperature is zero, which we know corresponds to being in the ground state of the quantum system. To formally see that we actually evaluate quantities on the ground state, consider the left hand side of Eq. (3.17). The $T = e^{-\delta\tau \mathrm{H}}$ can be expressed in the energy basis, $|n\rangle$, as

$$T = \sum_n e^{-E_n\delta\tau}|n\rangle\langle n|. \tag{3.18}$$

Since $M = \frac{\beta}{\delta\tau} \to \infty$ the trace in Eq. (3.17) becomes an average over the ground state, $|0\rangle$. More specifically, the ground state is the lowest energy state so it will be the one that survives with the highest relative probability coefficient $e^{-M\delta\tau E}$ (which comes from Eq. (3.18)) as $M \to \infty$. In other words,

$$\langle s_{j,0}s_{i,n}\rangle \sim \frac{1}{Z}\langle 0|\sigma_j^x T^n \sigma_i^x|0\rangle. \tag{3.19}$$

The justification for this implies that the ground state is not degenerate, which is true for the finite TFIM as discussed in Section. 3.1. The ground state expectation values is more easily evaluated. The ground state belongs to the $\mathbb{Z}_2$ subspace for which $\mathcal{P} = 1$. Since $\mathcal{P}\sigma_i^x\mathcal{P} = -\sigma_i^x$, the operator σ_i^x acting on the ground state in Eq. (3.19) only excites states of $\mathcal{P} = -1$. Therefore, schematically,

$$\sigma_i^x|0\rangle \sim |1\rangle + |\mathcal{P} = -1\rangle + \ldots, \tag{3.20}$$

where with $|1\rangle$ we indicate the first excited state which also belongs to $\mathcal{P} = -1$. As explained in Section. 3.1, the state $|1\rangle$ is the one with the smallest energy eigenvalue of the $\mathcal{P} = -1$ subspace.

Therefore, for very large n,

$$T^n \sigma_i^x |0\rangle \sim e^{-n\delta\tau E_1} |1\rangle. \tag{3.21}$$

The same argument would hold, also, if $|1\rangle$ was degenerate; it would just be all the degenerate states surviving. Including now the partition function, $Z = e^{-\beta E_0}$, in the denominator, one easily sees that

$$\langle s_{j,0} s_{i,n} \rangle \sim e^{-n\delta\tau(E_1 - E_0)}. \tag{3.22}$$

The correlation function exhibits the exponential decay with distance in the time direction. The distance of the two spins is given by $\tau = n\delta\tau$. The inverse correlation length in the time direction is directly related to the energy excitation of the first excited state

$$\xi_\tau^{-1} = E_1 - E_0. \tag{3.23}$$

The second correlation function is the one of the energy density,

$$\varepsilon(\tau) \sim J_{ij} s_{i,n} s_{j,n} \tag{3.24}$$

which we define in a specific time, $\tau = n\delta\tau$.

The relevant quantum mechanical operator, through which we get the correlation function, is

$$K \sim J_{ij} \sigma_i^x \sigma_j^x. \tag{3.25}$$

The correlation function, $\langle \varepsilon\varepsilon \rangle$, is calculated through the trace

$$\mathrm{Tr}\left(T^{M-n} K T^n K\right) \sim \langle 0|KT^n K|0\rangle. \tag{3.26}$$

The operator K is a $\mathcal{P} = 1$ operator in the sense that $\mathcal{P}K\mathcal{P} = K$. Therefore, acting on the ground state it is expected to excite even states. Actually, to avoid re-evaluating the ground state after the K has acted, we redefine K such that

$$K \to K - \langle 0|K|0\rangle. \tag{3.27}$$

With the same argumentation as before only the first excited state in the $\mathcal{P} = 1$ sector "survives" when n is very large. Therefore,

$$\langle \varepsilon(\tau)\varepsilon(0) \rangle - \langle \varepsilon \rangle^2 \sim e^{-\tau(E_1^{\mathcal{P}=1} - E_0)}, \tag{3.28}$$

and

$$\xi_\tau^{-1} = E_1^{\mathcal{P}=1} - E_0. \tag{3.29}$$

3.3 Finite-size scaling predictions for isotropic systems

In the previous section, we saw that correlation lengths of the classical correlation functions are directly related to the energy levels of the corresponding quantum model. If there exists a critical value for the transverse field parameter, $h = h_c$, such that the energy E of the excited state becomes degenerate with the ground state, then the correlation length diverges,

$$\xi^{-1}(h) = E(h) - E_0(h) \to 0 \qquad \text{as } h \to h_c. \tag{3.30}$$

As discussed in Section 3.1, such degeneracies are expected to occur for the infinite transverse-field Ising model. The reason behind this is related to the fact that $\xi \to \infty$ signals a second order phase transition and these should occur at infinite systems (see App. D).

Numerically, we can only implement finite systems, which formally do not exhibit phase transitions. Nevertheless, in finite systems of sufficiently large size, we expect to see remnants of what would be the critical behavior of the infinite system. This roughly means that instead of divergences we would see peaks in these quantities. These peaks are bounded by system size.

The finite-size scaling theory enables us to make predictions for finite-size effects. In this section, we will elaborate on some results of the theory on isotropic systems. We will invoke a number of physical assumptions and the results presented are heuristic. In order to solidify them, one should examine physical systems specifically. We will only give information on the Ising model through references, as discussing other physical systems is beyond the scope of the thesis.

In order to put finite-size scaling theory on a firmer basis, one needs to introduce renormalization group (RG) arguments. Since the renormalization group theory is extensive, we briefly review some essential results in App. D. In general, we follow the exposition of finite-size effects of [17].

Implicitly, we assume that the system we treat is a classical Ising model. It is described by the interactions of the type $K_1 s_i s_j + K_2 s_i$. The K_1 denotes the reduced interaction terms, βJ and the K_2 is the magnetic field. In an infinite system, $N \to \infty$, the singular part of the free energy is assumed to transform under an RG rescaling step as [17],

$$f_s\big(\{K\}\big) = b^{-d} f_s\left(\{K'\}\right). \tag{3.31}$$

The general assumption is that, at some point along the RG transformations, we would have $K' = K$. This would be the fixed point. Heuristically, the idea is to express the Hamiltonian with respect to parameters called scaling variable, υ, instead of the K. The scaling variable transforms as $\upsilon \to b^y \upsilon$ under the RG transfromations.

If the exponents y are positive, then, unless we set υ to zero, it will saturate to a value only at infinity. Variables υ with positive y are called relevant and to find the fixed

point they must be set to zero. For the case of the Ising model near the critical point, the relevant v are considered to be the reduced temperature $t = \frac{T-T_c}{T_c}$ and the magnetic field h (see Eqs. (D.17) and (D.18)). This is further explained in App. D.

Suppose that we have a system which is bounded in all linear dimensions, for example it is of size $L \times L \times L$. The system is also defined with a lattice constant a. Then, the L is a dimensionless variable and the physical length (measured in units of length) is aL. Under renormalization group transformations, we rescale, $a \to ba$, and keep aL constant. This means that $L \to L/b$.

In order to treat a finite system under the RG scheme, we need to introduce the system size L as a variable in the RG flow. At the same time, as $L \to \infty$ we should return to Eq. (3.31). The following generalization is assumed,

$$f_s\left(\{K\}, L^{-1}\right) = b^{-d} f_s\left(\{K'\}, bL^{-1}\right). \tag{3.32}$$

The assumption leading to this equation is that the finite size L does not affect the RG equations for K. Through Eq. (3.32), we can think of L^{-1} as a relevant scaling variable. The exponent indicates that the RG eigenvalue of this scaling variable is $y = 1$.

Given that we treat L as a scaling variable, we can infer the scaling form of the susceptibility at zero field. This is done in the same manner we showcase in App. D for a relevant variable. We iterate the RG transformations up to an arbitrary value in which the linearized RG flow holds. In turn, the susceptibility is given by

$$\chi(t, L^{-1}) \sim |t|^{-\gamma} \Phi\left(\frac{|t|^{-\nu}}{L}\right). \tag{3.33}$$

We observe here γ and ν. These are known as scaling exponents which as discussed in App. D are universal for a specific class (for example the Ising universality class) [10]. We see here that the scaling function, Φ, depends on $|t|^{-\nu}/L$. Furthermore, we know that, App. D, the scaling of the correlation length ξ_∞ of the infinite system is given by

$$\xi_\infty \sim \frac{1}{|t|^\nu}. \tag{3.34}$$

Therefore, the relevant parameter for the finite-size effects on the susceptibility is the ratio ξ_∞/L. To be consistent ξ_∞ is also given in units of lattice spacing. So, we can examine the behavior of χ according to the value of this ratio. If the system size is much larger than the correlation length, then, arguably, the behavior of χ is similar to as if $L \to \infty$[3]. On the other hand, for finite L as t decreases, the finite-size effects should become relevant. Roughly, we can say this happens when $|t| = L^{-1/\nu}$ [17].

We can rewrite Eq. (3.33) by multiplying and dividing with $L^{\gamma/\nu}$. In this case, we can group all the arguments $tL^{1/\nu}$ in a new scaling function $\tilde{\Phi}(tL^{1/\nu})$. In total we have,

$$\chi(t, L^{-1}) \sim L^{\gamma/\nu} \tilde{\Phi}\left(tL^{1/\nu}\right). \tag{3.35}$$

[3]Technically, $|t|^{-\nu} \to \infty$ when $t \to 0$. However, we implicitly mean that, here, we take the limit $L \to \infty$ first.

As stated at the beginning of this section, we expect the susceptibility to have a rounded peak in the finite system. In Eq. (3.35) the $L^{\gamma/\nu}$ indicates how the peak scales with system size. Technically, as we presented it, it indicates how the susceptibility scales with system size, at the critical temperature of the infinite system, $t = 0$. At $t = 0$, we have $\tilde{\Phi}(0)$ (which is not divergent because of the finite size of the system), so that this value is constant for all system sizes.

However, one could argue that $t = 0$ is close to the peak for large enough systems and, thus, $L^{\gamma/\nu}$ reveals the scaling of the peak as well. To see how this could happen, consider t_{max}, which indicates the position of the maximum of $\tilde{\Phi}\big(tL^{1/\nu}\big)$ for a specific L. If $t_{max} \sim L^{-1/\nu}$ then indeed the factor $L^{\gamma/\nu}$ also shows how the peak scales with system size.

To motivate why we expect $t_{max} \sim L^{-1/\nu}$ we have to state a more general assumption. If we assume that, at the infinite system, t_{max} becomes $t_c = 0$, it is not completely unreasonable to also assume, [11], that there exists a scaling law such as

$$t_{max} \sim L^{-\lambda}. \tag{3.36}$$

The exponent λ is to be defined. We, now, make the additional assumption that for the correlation length of the finite system, ξ, at t_{max}, we have

$$\xi_L(t_{max}) \sim L. \tag{3.37}$$

In this assumption, the correlation length is not only bounded by system size, it is directly proprotional to it. Given that as $L \to \infty$ then $\xi_L \to \xi_\infty$, and that $\xi_\infty \sim |t|^{-\nu}$, we can substitute Eq. (3.37) in Eq. (3.36) and get $\lambda = 1/\nu$.

What we have presented so far gives us some basic (heuristic) results for finite-size scaling. We can go a step further if we consider universality. In particular, while we explained the scaling behavior, there also exist prefactors in equations such as Eq. (3.35). We mention in App. D that the critical exponents are universal. However, there exist universal quantities other than the exponents.

We have the following expression for the singular part of the free energy of the infinite system,

$$f_s(t, h) \sim A_1 \, |t|^{2-\alpha} \, W\big(A_2 h \, |t|^{-\beta-\gamma}\big), \tag{3.38}$$

where we expressed Eq. (D.19) in terms of the scaling exponents α, β and γ. The W is the scaling function and also assumed to be universal [11]. On the other hand, the scale factors A_1 and A_2 are not universal. As we saw in App. D, such scale factors are system dependent. Similarly, a non-universal constant, ξ_0, may appear in the correlation length,

$$\xi_\infty \sim \xi_0 \, |t|^{-\nu} \, . \tag{3.39}$$

Then as long as the hyperscaling relation holds,

$$\alpha = 2 - d\nu, \tag{3.40}$$

it would be consistent to claim that,

$$A_1 \xi_0^d = \text{universal quantity}, \tag{3.41}$$

due to Eq. (3.38) [11]. If we consider the behavior close to the critical point, $t \to 0$, at $h = 0$,

$$\lim_{t \to 0} f_s(t, h = 0) \xi_\infty^d(t) = \text{universal}. \tag{3.42}$$

We assume the finite-size effects to appear in the singular free energy, Eq. (3.38), similarly as for the susceptibility,

$$f_s(t, h = 0, L) \sim A_1 \, |t|^{2-\alpha} \, W\big(\xi_\infty / L\big). \tag{3.43}$$

If we multiply and divide the right hand side by $(L/\xi_0)^{(2-\alpha)/\nu}$ and use Eqs. (3.39) and (3.40), we can re-express Eq. (3.43) as

$$f_s(t, h = 0, L) \sim \frac{1}{L^d} Y\big(C_1 t L^{1/\nu}\big). \tag{3.44}$$

Here Y is, again, considered a universal function, whereas C_1 is a non-universal scale factor related to ξ_0 and A_1 [11]. We, also, notice that there is no overall non-universal scale factor multiplying Y.

From Eq. (3.42), we see that ξ_∞ is directly related to a universal function as well. Furthermore, we assume that we can again treat the finite counterpart, ξ_L, as a function of ξ_∞ / L. Then, due to Eqs. (3.42) and (3.44) we get

$$\xi_L^{-1}(t, h = 0) = L^{-1} S(C_1 t L^{1/\nu}, 0). \tag{3.45}$$

The S is considered again a universal function, as explained. Therefore, at the infinite critical point, $t = 0$, we would have

$$\xi_L(0, 0) = L S(0, 0). \tag{3.46}$$

This showcases a very general prediction of RG and finite-size scaling. Namely, the correlation length is directly proportional to the linear size of the system through a universal function. In Section. 3.4, we will see that, due to conformal symmetry, we can specify this universal function and directly relate it to a critical exponent [11].

Therefore, the usefulness of finite-size scaling lies on the fact that with it we can, in principle, predict and find the universal properties of thermodynamic quantities. This is already suggested in Eq. (3.35). By scaling the susceptibility for different system sizes at the critical point of the infinite system, we can infer the value of the ratio γ/ν.

Furthermore, by plotting the values $\chi / L^{\gamma/\nu}$ around the critical point with respect to $tL^{1/\nu}$ for many system sizes, we should notice the curves, corresponding to each system size, collapse on each other. Actually, we want to reverse this process; to fine-tune our choice for ν so that we see curves collapsing onto each other.

In addition, what this scaling analysis suggests is that, at the critical point, $t = 0$, the quantity $\chi/L^{\gamma/\nu}$ should remain invariant with respect to system size. This is expected at least to leading order, as we have not considered corrections due to irrelevant variables anywhere [17]. This invariance can be used as a tool to find the critical point of the system.

The idea is to look for the point in which the curves $\chi/L^{\gamma/\nu}$ plotted with respect to t cross. This crossing point would correspond to the critical point. However, the remaining problem is that the exponent γ/ν is, in general, not known a priori. For this reason a quantity that might be used to locate the critical point is the Binder cumulant [27],

$$U_4 = \frac{3}{2}\left(1 - \frac{1}{3}\frac{\langle M^4\rangle}{\langle M^2\rangle^2}\right). \tag{3.47}$$

The Binder cumulant uses the ratio of the mean of two different powers of the magnetization. Since we take the mean values of the quantities, the ratio is not trivial. However, to leading order, the scaling theory predicts that the scaling, with respect to L, is the same for both $\langle M^4\rangle$ and $\langle M^2\rangle^2$. In the Ising model, since the spin is a scaling field (see App. D) and the magnetization squared and so on include spin-spin correlations, the finite-size scaling is given by the scaling exponent of the field, Δ_s, $M^2 \sim L^{-2\Delta_s}$ (see Eq. (D.31)). So, in principle, U_4 is a quantity that, when plotted with respect to t, should exhibit a crossing point that corresponds to the critical point and no finite-size scaling factor (such as $L^{\gamma/\nu}$ in the susceptibility) should be assumed.

Up to here we considered classical isotropic systems. On Section. 3.2, we saw that the d-dimensional transverse-field Ising model at zero temperature can be mapped to an effective $(d+1)$-dimensional anisotropic classical Ising model. Namely, the anisotropy appears between the interaction terms along the original spatial dimensions and the imaginary time dimension in Eq. (3.16). We consider the case where all J are equal and there is no anisotropy in the spatial dimensions.

To see if the anisotropy is important, one must examine the correlation length along the time dimension. We denote this correlation length by ξ_τ while by ξ we denote the correlation length in the spatial dimension. Then, for the transverse-field Ising models at least, it is applicable to consider, [24], the scaling at the critical point

$$\xi_\tau \sim \xi^z. \tag{3.48}$$

The z is the dynamic critical exponent and for the 2D transverse-field Ising model is considered to be equal to 1 [26], [17], [28]. This means that the scaling in the temperature/time dimension happens in the same manner as the scaling in the spatial dimensions. There is one relevant scaling length for all directions [24]. This was also motivated in App. D in the discussion around Eq. (D.37). The time and the spatial derivatives appear on essentially the same footing in the φ^4 Hamiltonian that would describe the anisotropic Ising model.

Another aspect we have brushed over is the proper definition of a correlation length. Consider again the quantum to classical mapping. There, due to the time direction being infinite, we could more properly define a correlation length, through a single decaying exponential in Eqs. (3.22) and (3.28). This is possible even if the spatial dimensions of the system are finite, in which case we would have the geometry $L \times L \times \infty$. In this case, due to finite-size scaling and the admittance that $z = 1$,

$$\xi_\tau^{-1} = E - E_0 \sim \frac{1}{L}. \tag{3.49}$$

We should restate that many of the arguments of this section are heuristic. We took the liberty of making assumptions while not having explicitly solved the model under discussion. Some of the argumentation followed from the assumption of universality. However, one example in which our heuristics are not enough, is that mean field theory (which is predicted to hold for $D > 4$) predicts values for the exponents such that the hyperscaling relation fails [17].

Nevertheless, the goal of this thesis is to put the TFIM on the sphere. This is a problem of dimensions, $D = 2 + 1$. As explained in Ch. 4, we aim to construct a locally isotropic TFIM on the sphere. Thus, it is more relevant to focus on the finite-size scaling arguments that are expected to hold for the universality class of the 3-dimensional classical Ising model. These include the fundamental relations for the finite-size scaling derived in this chapter. Namely, the exponents we will use are the exponent of the correlation length, ν as it exists within the argument, $tL^{1/\nu}$, of the scaling functions and the scaling dimension of the magnetization Δ_s.

3.4 Conformal symmetry and finite-size scaling

In the previous section, the finite-size scaling expressions were obtained by considering the RG theory. As mentioned in App. D, at the fixed point, scaling transformations do not change the parameters of the Hamiltonian. In this sense, the symmetry property of the system, at the fixed point, should be *scale invariance*.

It turns out that the fixed point Hamiltonian may be invariant under conformal transformations [17]. The system exhibits *conformal symmetry*. For practical purposes, a conformal transformation locally corresponds to a combination of a translation, rotation and dilatation (scaling transformation).

Conformal symmetry indicates the form of the correlation functions of physical observables. In particular, correlation functions of the scaling fields transform covariantly under the conformal transformations. This is similar to how correlation functions transfromed covariantly under scale transformations in the RG flow, which eventually gave us the form of the correlations functions (see for example Eq. (D.27)).

We also saw in Eqs. (3.22) and (3.28) that the correlation functions have a characteristic correlation length. Through Eq. (3.49) we showcased how, in a finite system, correlation lengths scale with system size. Conformal symmetry supplements this finite-size scaling result by determining the prefactors of Eq. (3.49).

Moreover, through Eqs. (3.23) and (3.29), we showed how low energy excitations are directly related to correlation lengths in the imaginary-time direction. Then, due to the conformal symmetry prediction, we should have an explicit expression for how these excitations scale with system size. In other words, doing finite-size scaling on the spectrum of the system should help us verify the appearance of conformal symmetry at the critical point.

To begin with, we will describe in more detail the conformal transformations. Consider a general infinitesimal transformation of a vector $\boldsymbol{r}$,

$$r'^{\mu} = r^{\mu} + \alpha^{\mu}(\boldsymbol{r}), \tag{3.50}$$

with $\alpha^{\mu}(\boldsymbol{r}) \ll 1$. If α is constant, this transformation is a translation. To see how other transformations come about, we need to consider a small volume around vector $\boldsymbol{r}$, $\Delta V(\boldsymbol{r})$. Then, we have to examine how the $\alpha(\boldsymbol{r})$ distorts this volume. For this we take the derivative over r^{ν},

$$\frac{\partial r'^{\mu}}{\partial r^{\nu}} = \delta^{\mu}_{\nu} + \alpha^{\mu}_{\nu}(\boldsymbol{r}), \tag{3.51}$$

where $\alpha^{\mu}_{\nu} = \dfrac{\partial \alpha^{\mu}}{\partial r^{\nu}}$. The $\alpha^{\mu\nu} = \alpha^{\mu}_{\kappa} g^{\kappa\nu}$ can be written as a sum of the three components,

$$\begin{aligned} \alpha^{\mu\nu} =& \frac{1}{2}(\alpha^{\mu\nu} - \alpha^{\nu\mu}) \\ &+ \frac{1}{d}\alpha^{\lambda}_{\lambda} g^{\mu\nu} \\ &+ \frac{1}{2}(\alpha^{\mu\nu} + \alpha^{\nu\mu}) - \frac{1}{d}\alpha^{\lambda}_{\lambda} g^{\mu\nu}. \end{aligned} \tag{3.52}$$

We know from continuum mechanics that the first term in Eq. (3.52) locally corresponds to a rotation of the volume $\Delta V(\boldsymbol{r})$. The second term corresponds to the dilatation of the volume. The last term is a traceless symmetric matrix and represents the shear of the volume $\Delta V(\boldsymbol{r})$. Conformal transformations are those whose shear component vanishes. Thus, conformal transformations are those which locally preserve the angles between vectors.

Therefore, conformal transformations are those which satisfy the equation,

$$\frac{1}{2}(\alpha^{\mu\nu} + \alpha^{\nu\mu}) - \frac{1}{d}\alpha^{\lambda}_{\lambda} g^{\mu\nu} = 0. \tag{3.53}$$

Based on what we discussed so far we can see that rigid rotations, translations and dilations do satisfy Eq. (3.53) [22]. In fact, these three transformations globally preserve

angles. In two dimension Eq.(3.53) can be satisfied by any analytic function, w, that maps the coordinate z to $w(z)$. In $d \geq 3$ the additionals transformation which satisfies Eq. (3.53) is the special conformal transformation (SCT),

$$\alpha^{\mu}(r) = b^{\mu} r^2 - 2b^{\lambda} r_{\lambda} r^{\mu}. \tag{3.54}$$

The b here is an infinitesimal constant vector. The SCT corresponds to a local composition of a rotation and a dilatation. To see this, we need to evaluate the Jacobian of the transformation [29]. It gives

$$\begin{aligned} \frac{\partial r'^{\mu}}{\partial r^{\nu}} &= \left(1 + 2b_{\lambda} r^{\lambda}\right) \delta^{\mu}_{\nu} + 2\left(b_{\nu} r^{\mu} - r_{\nu} b^{\mu}\right) \\ &\approx \left(1 + 2b_{\lambda} r^{\lambda}\right)\left(\delta^{\mu}_{\nu} + 2\left(b_{\nu} r^{\mu} - r_{\nu} b^{\mu}\right)\right). \end{aligned} \tag{3.55}$$

The approximate equality follows if we take terms only up to $\mathcal{O}(b)$. The component $\delta^{\mu}_{\nu} + 2(b_{\nu} r^{\mu} - r_{\nu} b^{\mu})$ of Eq. (3.55) is an orthogonal matrix up to $\mathcal{O}(b)$. Therefore, it corresponds to a local rotation [29]. The component $(1 + 2b_{\lambda} r^{\lambda})$ corresponds to a local dilation. This showcases that locally angles are preserved.

The four conformal transformations also have a finite counterpart [22]. It is also relevant to study the generators of the conformal transformations. The generators satisfy the conformal algebra, as seen in App. B2. It is through this algebra, in turn, that we can understand how the correlation functions transform. Some essential mathematical details of this are discussed in the App. B2. However, before utilizing these results, we will discuss the qualitative picture of the transformations of the correlation functions.

To heuristically describe the transformations, we consider the viewpoint of the RG flow. More specifically, in RG, the lattice spacing is rescaled by a constant multiplicative factor $1/b$, $a \to a/b$. In this case, all positions $\boldsymbol{r}$ change as $\boldsymbol{r}' = b\boldsymbol{r}$. This corresponds to the dilation. Through general conformal transformations, the lattice spacing could be rescaled by a factor that depends on position, $b(\boldsymbol{r})$. Then, $b(\boldsymbol{r})^d$ would be the Jacobian of the transformation $\boldsymbol{r} \to \boldsymbol{r}'$.

We assume that $b(\boldsymbol{r})$ is slowly varying and the Hamiltonian of the system is short ranged. In this case, we would expect that local parameters, near any specific region $\boldsymbol{r}_k$, would transform similarly to as if we were performing a uniform RG transfromation with a rescaling factor $b(\boldsymbol{r}_k)$ everywhere. We know that the fixed point Hamiltonian would be invariant if the rescaling factor was $b(\boldsymbol{r}_k)$ everywhere. Due to the above reasoning, it should also be invariant under a slowly varying $b(\boldsymbol{r})$.

Evidently, the argumentation presented is heuristic. We explained it in conjuction with the RG transformations because it motivates a generalization to Eq. (D.32). Specifically, for the correlation functions of observables φ,

$$\langle \varphi_1(\boldsymbol{r}_1)\varphi_2(\boldsymbol{r}_2)\dots\rangle = \prod_i b(\boldsymbol{r}_i)^{\Delta_i} \langle \varphi_1(\boldsymbol{r}'_1)\varphi_2(\boldsymbol{r}'_2)\dots\rangle, \tag{3.56}$$

where Δ_i is the scaling exponent of φ_i. As explained in App. B2 this type of transformation holds for scalar primary fields φ. Nevertheless, the physical results we will discuss do relate to scalar fields.

It is useful to determine how the correlation functions, which fulfill Eq. (3.56), look like as functions of the $\boldsymbol{r}_j$. Firstly, Eq. (3.56) determines the form of the two point correlation functions, such as $\langle\varphi_1(\boldsymbol{r}_1)\varphi_2(\boldsymbol{r}_2)\rangle$. Translations and rotations both yield $b = 1$. This means that the correlation function is invariant under those transformations. Thus, it depends on $|\boldsymbol{r}_2 - \boldsymbol{r}_1|$. Therefore, due to invariance under the 180° rotation, we have that $\langle\varphi_1(\boldsymbol{r}_1)\varphi_2(\boldsymbol{r}_2)\rangle = \langle\varphi_1(\boldsymbol{r}_2)\varphi_2(\boldsymbol{r}_1)\rangle$. This also holds for the correlation function on the right hand side of Eq. (3.56), $\langle\varphi_1(\boldsymbol{r}_1')\varphi_2(\boldsymbol{r}_2')\rangle = \langle\varphi_1(\boldsymbol{r}_2')\varphi_2(\boldsymbol{r}_1')\rangle$. However, $b(\boldsymbol{r}_1)^{\Delta_1}b(\boldsymbol{r}_2)^{\Delta_2}$ and $b(\boldsymbol{r}_1)^{\Delta_2}b(\boldsymbol{r}_2)^{\Delta_1}$ are in general not equal. Therefore, the two-point correlation function is zero unless $\Delta_1 = \Delta_2 = \Delta$. So, the general form of the two-point the correlation functions is

$$\langle\varphi_i(\boldsymbol{r}_1)\varphi_j(\boldsymbol{r}_2)\rangle = \frac{d_{ij}}{|\boldsymbol{r}_2 - \boldsymbol{r}_1|^{2\Delta}} \tag{3.57}$$

where $\varphi_i(\boldsymbol{r}_1)$ and $\varphi_i(\boldsymbol{r}_2)$ have the same scaling dimensions. Given that the correlation function is real and symmetric under $i \leftrightarrow j$, the matrix d_{ij} also has these properties.

It is easy to see that Eq. (3.57), does transform according to Eq. (3.56) for translations, rotations and dilatation. It is straighforward but laborious to work out the transformation under the SCTs. This is done, for example, in [30]. There, the symmetry of Eq. (3.57) under the inversion of $\boldsymbol{r}_1$ and $\boldsymbol{r}_2$ is used. Nevertheless, this general form for the two-point correlation function could be inferred from scale invariance. The advantage of conformal symmetry is more starkly shown from the fact that it, also, fixes the form of three point correlation functions [17].

Now, we can see what implications conformal symmetry has on finite-size scaling. To do that, we need to consider an appropriate conformal transformation. We will map the infinite d-dimensional plane, $\mathbb{R}^d$, to the "cylinder", $S^{d-1} \times \mathbb{R}$ as in [12]. Expressing the coordinates in $\mathbb{R}^d$ in radial coordinates we get

$$ds^2_{\mathbb{R}^d} = dr^2 + r^2 d\Omega^2. \tag{3.58}$$

The $d\Omega^2$ denotes the $d-1$ angle part of the coordinates. If we consider the coordinate transformation

$$(r, \Omega) = \left(e^{u/R}, \Omega\right), \tag{3.59}$$

where $-\infty < u < \infty$, the line element becomes

$$ds^2_{\mathbb{R}^d} = \frac{1}{R^2} e^{2u/R}\left(du^2 + R^2 d\Omega^2\right). \tag{3.60}$$

We notice that $du^2 + R^2 d\Omega^2$ is describes the "cylinder", $S^{d-1} \times \mathbb{R}$, with radius R. So, the metrics of the two geometries are related by the multiplicative factor $\frac{1}{R^2}e^{2u/R}$. This multiplicative factor is not a constant, it depends on the coordinate u. However, even in

this case the transformation is conformal. That is the angles between vectors are (locally) preserved in this mapping. For a more analytic explanation of this see Apps. B1 and B3.

The transformation conformally relates the theories defined on $\mathbb{R}^d$ and $S^{d-1} \times \mathbb{R}$. As explained in App. B3 and [12], the two-point correlation function of a field φ transforms as,

$$\langle \varphi(r_1, \Omega_1)\varphi(r_2, \Omega_2)\rangle_{\mathbb{R}^d} = R^{2\Delta} e^{-\Delta(u_1+u_2)/R} \langle \varphi(u_1, \Omega_1)\varphi(u_2, \Omega_2)\rangle_{S^{d-1}\times\mathbb{R}}. \tag{3.61}$$

From Eq. (3.57) we know that the correlation function of the left hand side is proportional to $\frac{1}{|\boldsymbol{r_2}-\boldsymbol{r_1}|}$. Using Eq. (3.59), we see that for large values of $|u_2 - u_1|$,

$$\langle \varphi(u_1, \Omega_1)\varphi(u_2, \Omega_2)\rangle_{S^{d-1}\times\mathbb{R}} \propto e^{-\frac{\Delta}{R}|u_2-u_1|}. \tag{3.62}$$

We see that the correlation function on the cylinder decays exponentially for two points far away from each other. We can physically explain this result based on finite-size scaling theory. The cylinder, on which the system is placed, is bounded in all dimensions except one. Therefore, we do expect that the correlation length, ξ, of the correlation function to be bounded by system size, as in Eq. (3.49) . Specifically here,

$$\xi = \frac{R}{\Delta}. \tag{3.63}$$

We see that the ξ is directly related to the scaling dimension of the corresponding scaling field. We notice that as a consequence of conformal symmetry, this result was derived for the geometry $S^{d-1} \times \mathbb{R}$. This is the motivation for studying the Ising model in $S^2 \times \mathbb{R}$. In particular, the quantum TFIM placed on the S^2 at zero temperature, maps, according to Section. 3.2, to a classical system corresponding to $S^2 \times \mathbb{R}$.

Having established this result for the correlation length, Eq (3.63), we should point out that the transformation of Eq. (3.59), does not follow from the four conformal transformations (translation, rotation, dilation and SCT) described previously. The motivation for using Eq. (3.62) for the transformation of the correlation function is explained in App. B3. Heuristically, we could perhaps say that in the limiting case of large radii R, the sphere S^{d-1} is locally equivalent to the plane.

We should emphasize, however, that the transformation of Eq. (3.59) is still a conformal one. The result of Eq. (3.63) has been confirmed analytically for the Ising model in the case of $d = 2$, where a conformal transformation can be carried out by any analytic function [11]. As we will discuss below, the classification of the energy spectrum which essentially follows from Eq (3.63), has been numerically verified in $d = 3$ as well.

As discussed, Eq. (3.63) shows how the correlation length is related to the scaling exponent. Due to Eqs. (3.23) and Eqs. (3.29), this gives a prediction for energies of the corresponding critical quantum system. In fact, the predictions of conformal symmetry are about the structure of the spectrum and not only for specific energy excitations.

In order to understand those predictions, we have to utilize the more concrete results derived in App. B2. In addition, the spectra are dealt within a quantum system, which in our case is the TFIM. Then, we need to treat the quantum mechanical entity that yields the same expression such as the classical correlation function $\langle\varphi_1(r_1)\varphi_2(r_2)\dots\rangle$.

We saw how correlation functions can be computed through vaccuum averages, in Eqs. (3.19). In general, we assume that there is a corresponding vacuum average for which, [30],

$$\langle\varphi_1(\boldsymbol{r}_1)\varphi_2(\boldsymbol{r}_2)\dots\rangle = \langle 0|O_1(\boldsymbol{r}_1)O_2(\boldsymbol{r}_2)\dots|0\rangle, \tag{3.64}$$

Essentially, we introduced operators O evaluated at the corresponding $\boldsymbol{r}_i$. These gain their $\boldsymbol{r}$ dependence via

$$O(\boldsymbol{r}) = e^{ir^\mu P_\mu} O(0) e^{-ir^\mu P_\mu}. \tag{3.65}$$

In App. B2 we explained how the generators act on the fields. The notations as well as the commutation relations are clarified there. In the case of the quantum mechanical operators, the action of the generators is given through the commutators $[\mathcal{G}, O(\boldsymbol{r})]$, [30]. Performing a transformation up to first order (similarly to Eq. (B.38) for the classical fields) in the right hand side of Eq. (3.64), we observe that this vaccuum must be invariant under G,

$$G|0\rangle = 0. \tag{3.66}$$

We are interested for the ones at $r = 0$, which are simpler [30],

$$[K_\mu, O(0)] = 0, \tag{3.67}$$
$$[P_\mu, O(0)] = -i\partial_\mu O(0)\big|_{\boldsymbol{r}=0}, \tag{3.68}$$
$$[D, O(0)] = -i\Delta O(0), \tag{3.69}$$
$$[L_{\mu\nu}, O(0)] = S_{\mu\nu} O(0). \tag{3.70}$$

The generators in the transformations are, in order, the generator of the SCTs, translations, dilations, and rotations. We can use these equations to intuitively understand how the spectrum of a quantum system, that exhibits conformal symmetry, looks like.

Due to Eq. (3.69), the state

$$|\Delta\rangle = O_\Delta(0)|0\rangle, \tag{3.71}$$

is an eigenstate of the dilatation operator D. We specified the operator O_Δ by the subscript Δ, to indicate that it corresponds to that dimension. More specifically,

$$D|\Delta\rangle = -i\Delta|\Delta\rangle \tag{3.72}$$

The scaling dimension of a state is raised and lowered by acting on $|\Delta\rangle$ with the generators of translations and SCTs respectively. An attempt to explain why this comes about is given in App. B2. Following [30] and due to Eq. (B.22) we have

$$DP_\mu|\Delta\rangle = -i(\Delta + 1)P_\mu|\Delta\rangle. \tag{3.73}$$

The momentum operator P_μ "raises" the eigenvalue of D by one unit. Similarly, the operator K_μ lowers the eigenvalue by one unit. Due to Eqs. (3.66), (3.67) and (3.71), the K_μ has the additional property,

$$K_\mu|\Delta\rangle = 0. \tag{3.74}$$

Therefore, acting on $|\Delta\rangle$, the K_μ no longer lowers the eigenvalue by one unit but rather terminates the eigenvalue descend. An operator/field is called a primary when it corresponds to the state $|\Delta\rangle$ for which Eq. (3.74) holds [30]. The next step now is to see where the energy of the system comes in. The physically motivated assumption is that the dilatation eigenstates $|\Delta\rangle$ form the basis of energy eigenstates.

One justification for this assumption follows from Eqs. (3.23), (3.29), and (3.63). We see that the correlation length is directly related to the scaling exponent as well as the energy difference. Therefore, these two quantities are directly related to each other. As explained, this is expected to hold in $S^{d-1} \times \mathbb{R}$ and it should hold for primary fields.

However, we can motivate a more general statement through Eq. (3.61), which has implication on the structure of the spectrum beyond the primary fields. Acting with an infinitesimal dilation, $r \to b\boldsymbol{r}$, with $b = (1+\varepsilon)$, the left hand side of Eq. (3.61) becomes,

$$b^{-2\Delta}\langle\varphi(\boldsymbol{r}_1/b, \Omega_1)\varphi(\boldsymbol{r}_2/b, \Omega_2)\rangle, \tag{3.75}$$

due to the transformation $\varphi(\boldsymbol{r}) \to \varphi'(\boldsymbol{r}) = b^{-2\Delta}\varphi(\boldsymbol{r}/b)$ described in App. B2.

The right hand side of Eq. (3.61) then necessarily becomes

$$b^{-2\Delta}R^{2\Delta}\exp\left\{-\Delta\frac{u_1+u_2}{R}\right\}b^{2\Delta}\langle\varphi(r_1 - R\ln b, \Omega_1)\varphi(r_2 - R\ln b, \Omega_2)\rangle. \tag{3.76}$$

We observe that the effect of the dilation on the left hand side (representing the flat space) corresponds to a translation along the u direction by $-R\ln b$ on the right hand side (representing the "cylinder"). The factor $b^{2\Delta}$ also comes from the translation of the u in the exponent of Eq. (3.76) and cancels the $b^{-2\Delta}$. The transformation carries over similarly in the quantum case (see Eq. (3.64)).

In terms of the TFIM and the quantum to classical mapping, the translation in the u direction is actually a translation in the imaginary time direction. This translation, as we saw in Section. 3.2, is induced within a quantum mechanical vacuum average via the transfer matrix, Eq. (3.9). In this case the argument in the transfer matrix would be $\delta\tau = -R\ln b \approx -R\varepsilon$. This would give

$$T = 1 - \delta\tau\mathrm{H} = 1 + i(\delta\tau)i\mathrm{H}. \tag{3.77}$$

To be explicit, what this analogy seeks is a relation between the generator of dilations, D and the Hamiltonian, H. Therefore, we want to induce a translation in the time direction,

within a vacuum state average (see Eq. (3.64)), with the Hamiltonian acting in a similar manner as a generator. This may be motivated, since within this average, to first order in ε, we have

$$O \to O + i\delta\tau[i\mathrm{H}, O], \tag{3.78}$$

for a time translation. To actually be analogous to the generator we must also demand that $\mathrm{H}|0\rangle = 0$, which in the TFIM we can do by redefining H to $\mathrm{H}' = \mathrm{H} - E_{ground}$. One particular aspect we should also clarify is that Eq. (3.61) is expected to hold for isotropic systems. So, it should be emphasized that the analogy presented for the TFIM relies on $z = 1$ in Eq. (3.48).

The conclusion, which relates the Hamiltonian spectrum on the "cylinder" to that of the dilation operator on the plane, should be more strictly reached. For example, in [31], the relation between the Hamiltonian in the cylinder and the generator of dilation on the flat space is explicitly shown in 2 dimensions using the stress-energy tensor. More specifically, one can derive how the stress-energy tensor transforms under the conformal mapping between the two geometries. However, it is beyond the scope of the thesis to attempt generalizing such quantum field theory arguments in three dimensions.

The classification of the energy spectrum, thus, happens according to the spectrum of the dilation operator, Eqs. (3.72), (3.73), and (3.74). The states with eigenvalues Δ correspond to the operators, O_Δ, called *primaries* (or quasi-primaries in the context of 2D conformal symmetry). Around each eigenvalue of a state created by a primary, there is a so called conformal multiplet consisting of eigenvalues of the *descendants* of the primary.

The descendants are generated by acting on the primary with P_μ and K_μ. The eigenvalues of their energy are given by $\propto (\Delta + n)$, where n is an integer, according to the construction which follows from Eq. (3.73). This behavior of the energy spectrum has been found numerically for $d = 3$ (see [16]).

So far, we have not discussed the rotations induced through Eq. (3.70). We did not use them in the construction of the energy eigenvalues. In fact, they attribute an additional quantum number to the eigenstates [16]. We can see this since the generator of rotations commutes with the generator of dilations (see also App. B2). Actually, as discussed in App. B2, only by admitting that there are scaling fields that belong to an irreducible representation of the $SO(3)$ can we define the primary fields in this sense.

Lastly, we would like to note that our considerations on conformal symmetry were about $d = 3$ or above. In the case of two dimensions, as we noted, conformal transformations can be carried out through analytic functions, w, that map z to $w(z)$. This enlarges the possible allowed transformations. Furthermore, the conformal group we described in App. B2 consists of the four generators corresponding to the four transformations we described. Through these, the conformal algebra is obtained. In two dimensions one may formulate the Virasoro algebra, through the use of stress-energy tensor [11].

This infinite algebra also includes the generators of the four transformations relevant in $d \geq 3$. The transverse-field Ising chain has been shown analytically to exhibit conformal symmetry [11]. Furthermore, on the more practical side, it is easier to numerically study the system placed on the $S^1 \times \mathbb{R}$ geometry. The main reason is the fact that simulating this corresponds to demanding periodic boundary conditions on the quantum chain. The systems of different sizes then look locally identical; this, as we explained in Ch. 2, is not the case for the sphere $\left(S^2\right)$.

Chapter 4

Transverse-field Ising model on the sphere

The goal of this chapter is to study the TFIM on the sphere and evaluate it at criticality. To define the spherical TFIM we will use the hopping parameters J that were introduced for the free particle problem. The J will be used as interaction coefficients in the TFIM. Even though they were found on the non-interacting problem, they contain the essential information on rotational invariance. In order to check if the system indeed exhibits the $SO(3)$ symmetry, we will look at its spectrum. For this, exact diagonalization will be used and, thus, small system sizes will be studied.

To study the system at criticality, we, first, have to find the critical field h, as explained in Chapter. 3. We will attempt to do so by using the finite-size scaling methods we know are applicable for the flat 2D transverse-field Ising model. These include finding crossing points of the Binder cumulant and of (appropriately rescaled) quantities such as the magnetization squared, M^2. However, the peculiarity that appears on the spherical model is that, for different system sizes, the systems are not necessarily locally equivalent. The coordination number (see App. C) as well as the statistical behavior of the J, shown for example in Fig. 2.8, change as we vary the system size. Ultimately, our search for the critical h is halted due to strong finite-size effects.

4.1 Low energy behavior

The general Hamiltonian of the TFIM with nearest neighbor interactions is

$$\mathrm{H} = -\sum_{\langle ij \rangle} J_{ij} S_i^x \otimes S_j^x - h \sum_i S_i^z. \tag{4.1}$$

From the discussion of Ch. 2, we know that placing the model on the sphere means, in principle, placing it on an irregular lattice. This lattice dictates how the spins connect to each other. We also saw that the $SO(3)$ is recovered faster, with respect to system size, for the free particle placed on the Fibonacci lattice. The main idea in this chapter is to use the free particle hoppings, Eq. (2.29), as interaction coefficients in the spin system. Since they approximately create the Laplacian (which is rotationally invariant), then, they should approximately satisfy the relation $J_{R(i),R(j)} = J_{i,j}$. Evidently, this relation is schematic and mostly appropriate in the continuum limit, since the rotated points are not necessarily part of the irregular lattice. In addition, this choice for the J implies, locally, the same isotropy that appears on the flat TFIM. This is discussed in the next section.

The first direct check we can do, to examine if the $SO(3)$ symmetry is recovered, is to look at the spectra. We will do this with exact diagonalization. However, due to the spin-1/2 Hilbert space having size 2, the Hamiltonian is described by an $2^N \times 2^N$ matrix. The upside is that the matrix is very sparse. The largest system we can simulate has in total $N = 24$ spins. According to the geometric arguments made in Section. 2.4, we expect to be able to discern (almost) degenerate energy levels with $l = 0, 1$, and 2.

In Fig. 4.1 we plot the low energy spectrum of excitations. The plots include excitations only in the odd $\mathbb{Z}_2$ sector ($\mathcal{P} = -1$). The ground state of the system, E_0, belongs to the even $\mathbb{Z}_2$ sector ($\mathcal{P} = 1$). A plot of excitations in the even sector looks qualitatively similar and would yield a similar discussion. In order to evaluate if $SO(3)$ is recovered with our choice of J_{ij}, we compare the low energy spectrum with that of a system where the interaction coefficients are constant and equal to the mean value of our J_{ij}.

The Fig. 4.1 shows, in both cases, clusters of three or five energy eigenvalues which are closer together and have a noticeable gap with respect to the rest. In the case of the free particle-J_{ij}, (b), these clusters exhibit a better degeneracy compared to the case of constant J, (a). This showcases the advantage of choosing J_{ij} that make up the Laplacian. Nevertheless, the appearance of noticeable clusters, even when the couplings are constant, signifies that the system is sensible to the underlying geometry. From this, we can confirm that the configuration of the connections between spins, that is the coordination number (described in more detail in App. C), is also very relevant for the interacting system in the sphere.

However, there are also eigenvalues for which it becomes more difficult to discern gaps in the spectrum. We, therefore, need, if possible, to be able to distinguish the energy levels more systematically. To do so, we will implement rotations in the same way as described in Section. 2.4. The permutations, R, of spin positions will be applied on the eigenstates; $|\psi\rangle \to R|\psi\rangle$. The permutation R corresponds to the equivalent of $e^{i\theta L^z}$ applied on the positions of the spins (and not the spins themselves). Here, $\theta = \frac{2\pi}{\sqrt{N}}$.

It is not guaranteed that the eigenstates themselves are eigenstates of this L^z. They

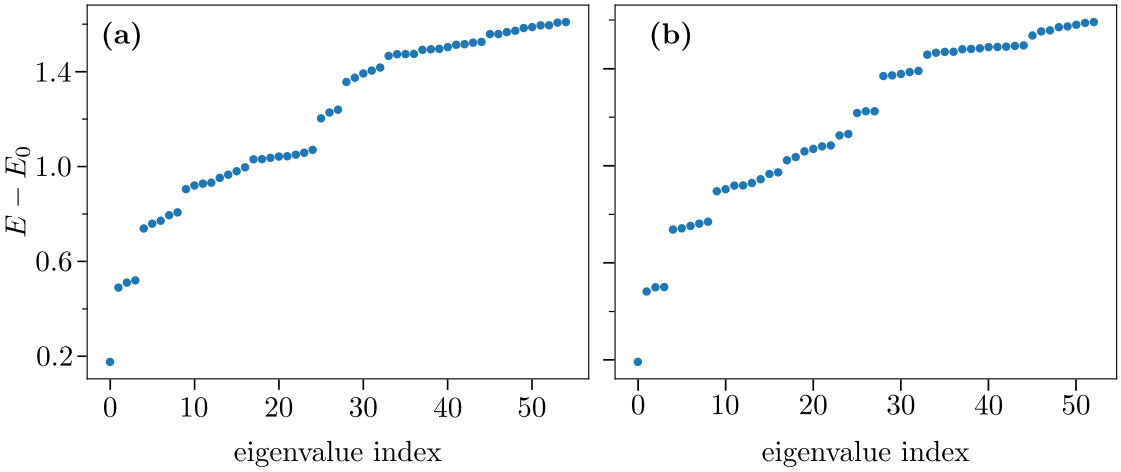

Figure 4.1: Low energy excitations for the spherical transverse-field Ising model. The triangulated Fibonacci lattice with $N = 24$ is used. The plots include excitations only in the odd sector of $\mathbb{Z}_2$ ($\mathcal{P} = -1$) at $h = 0.8$. The ground state of the system, E_0, belongs to the even $\mathbb{Z}_2$ sector. The mean value of the couplings J that solve the Laplacian is denoted by $\langle J \rangle$. (a) The low energy excitations of the TFIM with constant interaction coefficients, all equal to $\langle J \rangle$. (b) The low energy excitations of the TFIM where the free particle hoppings are used as interaction coefficients. We can observe that the spectrum in (b) exhibits better quasi-degeneracy compared to that in (a). We can distinguish better the almost degenerate levels with 1,3, and 5-fold quasi-degeneracies. These should correspond to the $SO(3)$ $l = 0, 1, 2$ levels. It must be noted that this distinction may also be done for (a), even though the approximate degeneracy is worse. This explicitly showcases that, apart from the appropriate couplings, the configuration of the system (how spins are connected to each other) plays an important role on creating the sphere.

might be linear combinations of the angular momentum eigenstates. Therefore, we need to look at eigenstates with similar energy eigenvalues. For example, if there are three similar energies, we will diagonalize the 3×3 matrix created from the inner products

$$\langle \psi_i | R | \psi_j \rangle. \tag{4.2}$$

The i and j indicate a combination of the three eigenstates which have adjacent energy eigenvalues.

In general, this process will be automated and will include inner products of up to five eigenstates similar in energy. For each eigenstate we have, we will find the 4 eigenstates with the closest energies. Then, we will form matrices of the inner products, Eq. (4.2), between these 5 eigenstates. As a result, we will create 1,3, and 5 dimensional matrices.

The 1 dimensional matrix is just the inner product of the rotated state with the original state. In the 3 dimensional one, the inner products are between three states (the chosen eigenstate and the 2 energetically closest eigenstates). The same logic follows for the

5 dimensional matrix. In order to find the angular momentum numbers, m, we will diagonalize the matrices. To extract the m, we will look at the arguments on the phase factors of the complex eigenvalues.

Since we know that $m = -l, \ldots, l$ we can easily assess the m we find. More specifically, we take the norm of the difference between the arranged m we obtained and their expected values. To accept that, an energy level corresponds to the l we set a threshold for the norm. This way we verified that the energy levels that visibly exhibit a quasi-degeneracy in Fig. 4.1 do indeed belong to $l = 0, l = 1$ and $l = 2$. This is, also, found for the perhaps less obvious $l = 1$ and $l = 2$ levels that appear around the 30^{th} energy eigenvalue.

In order to find any additional energy level, the idea is to lower the norm exactly before the point where we can no longer verify one of the visible energy levels. In the case of Fig. 4.1, this yields, for example, an additional $l = 2$ level that consists of the 37^{th} to the 41^{st} energy eigenvalue. The precise counting in the figures is not relevant as they are either way not visible. In general, such results should be taken with caution. A better verification of that should be to consider a rotation around a different axis. If we could confirm, using the same process, that the m we find also indicates an $l = 2$ energy level, then such results would be more concrete.

4.2 Spherical transverse-field Ising model at criticality

We are interested in the spherical TFIM at criticality particularly because of the suspected emerging conformal symmetry. In Section. 3.4 we described the predictions for the spectrum of systems placed on the $S^2 \times \mathbb{R}$ geometry that exhibit conformal symmetry and are isotropic. The isotropy is illustrated explicitly in Eq. (3.63), where the correlation length in the infinite direction scales with the linear system size, R, and not with a power of it. Therefore, for the theory to be applicable, the spherical TFIM should, at least, behave isotropically between the time and space directions.

Since the dynamical exponent, z, is taken to be equal to 1 for the flat 2D transverse-field Ising model [26], its behavior is considered to be isotropic at the critical point. This, as we saw in App. D, may be motivated by the fact that the derivatives in the φ^4 theory (which is used for the study of the Ising universality class in the continuum) in the time and space direction appear on the same footing. However, it is not evident why this might hold for the spherical TFIM described by Eq. (4.1). We can only motivate an answer for this. The way we constructed the spherical TFIM should make the model locally equivalent to a 2D flat TFIM.

More specifically, the couplings J used in the TFIM were also used to construct the Laplacian. Using the same J, we establish isotropy up to second order, in the sense described in the App. D, through Eqs. (D.37)- (D.41) for the classical Ising model. We saw in Section. 3.2 that the system at zero temperature is effectively described by a

Hamiltonian which has a component in the spatial directions and in the time direction $(\boldsymbol{r}, \tau)$, Eq (3.16). Schematically, for each site i in the spatial directions, in a single time step τ, the expansion of the intreacting terms gives

$$\sum_j J(\boldsymbol{r}_i - \boldsymbol{r}_j) s(\boldsymbol{r}_i, \tau) s(\boldsymbol{r}_j, \tau) \approx$$
$$\sum_j J(\boldsymbol{r}_i - \boldsymbol{r}_j) s(\boldsymbol{r}_i, \tau) \Bigg(s(\boldsymbol{r}_i, \tau) + \sum_k \left.\frac{\partial s}{\partial r^k}\right|_{\boldsymbol{r}_i, \tau} (r_i^k - r_j^k) + \sum_{k,l} \left.\frac{\partial^2 s}{\partial r^k \partial r^l}\right|_{\boldsymbol{r}_i, \tau} (r_i^k - r_j^k)(r_i^l - r_j^l) + \dots \Bigg). \quad (4.3)$$

We observe from Eqs. (2.25)- (2.27) that the construction of the Laplacian corresponds to the first order terms and the cross terms in second order being set to zero in Eq. (4.3). The coefficients of the diagonal second order derivatives become constant. This expansion, then, corresponds to the case of Eq. (D.40) which describes an isotropic system up to second order. It means that both directions appear on the same footing. It is easy to see that a similar expansion along the time direction at a constant $\boldsymbol{r}$, again, corresponds to that of an isotropic system.

Essentially, what we did with this expansion is establish the same kind of expansion up to second order (or up to $\boldsymbol{k}^2$ in the Fourier expansion in a regular lattice) as we would for the spatial and the time component of the flat 2D transverse-field Ising model. The $\boldsymbol{k}^2$ term is the relevant term up to which we keep when considering, for example, the φ^4 theory [32] (see also App. D). It is in this sense that we claim to locally approximate the flat system on our sphere.

In any case, one should verify the scaling behavior for the system by explicitly evaluating it at criticality. For this, we will first attempt to find the critical field h. One way to do so might be to look at the spectrum. In Section. 3.2, we saw that degeneracies of the excited states with the ground state indicate divergence of the correlation length. For this reason, we will evaluate how the low energy eigenvalues behave as functions of h. In Fig. 4.2, we plot the first ($\mathcal{P} = -1$) and second ($\mathcal{P} = 1$) energy excitations for $N = 14, 18, 22$.

The plots indicate a region, roughly around $h \approx 0.7$, where the energy of the second excited state moves towards the ground state energy. While the dip appears on all system sizes at the same region of h, it is not very instructive to do a finite-size scaling of the spectrum. One reason is that the linear sizes, $L = \sqrt{N}$, we can implement are all of the same order of magnitude. We could simulate even smaller systems to have a change of the order of magnitude. However, it is questionable how good approximations these system sizes would be to the sphere. Therefore, there can be no substantial scaling with exact diagonalization in this case.

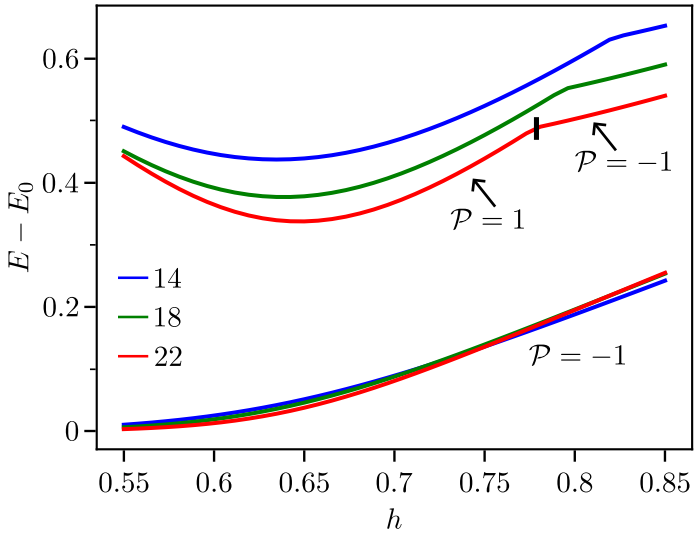

Figure 4.2: Plot of the first two excited energies of the spherical TFIM for various system sizes. The first excited states belong to the odd $\mathbb{Z}_2$ sector ($\mathcal{P} = -1$). The excitations energy in this case corresponds to Eq. (3.23). The second excited energies, for which $\mathcal{P} = 1$, correspond to Eq. (3.29). The dips they exhibit coarsely suggest that the critical value may be around $h \approx 0.7$. We also observe that the the second excited state has different $\mathcal{P}$ at the point where the slope of the energy abruptly changes.

In addition, the statistical distribution of the J is not similar between the system sizes considered. We saw in Section. 2.3 that this distribution is only similar between system sizes N and $m\Phi^2 N$, where m is an integer and Φ is the golden ratio, given by Eq. (2.3). In fact, we found that this most robustly holds for $N \gtrsim 200$. Therefore, this equivalency would be questionable even if we compared small system sizes related by a factor $m\Phi^2$.

In order to compare similar systems and reach the regime where finite-size scaling theory should hold, we have to consider large system sizes. The system sizes compared will be related by a factor of Φ^2 as explained before. We should note, however, that even though the statistical behavior for the J will be similar, the coordination number will be different for different lattice sizes. As explained in App. C, more sites with 6 neighbors appear as the system size is increased.

To evaluate these systems we will look at thermodynamic observables, such as the magnetization squared, M^2 or quantities directly related to observables, such as the Binder cumulant U_4. More specifically, these quantities will be plotted with respect to h for various system sizes. As discussed in Section. 3.3, the curves of $M^2 L^{2\Delta_s}$, where $L = \sqrt{N}$, or of the Binder cumulant should exhibit crossing points for different system sizes. In particular, the expectation is that for all system sizes the curves cross at the same point. This, in turn, is the critical point.

Realistically though, convergence to a single crossing is expected to happen at large system sizes, where finite-size scaling theory is actually applicable. If we see multiple crossings, we could, perhaps, apply corrections to finite-size scaling, as explained for example in [33]. The method we will be using for these evaluations is the Stochastic Series expansion (SSE) quantum monte carlo [34].

In order to study the quantum phase transition, we are interested in the zero temperature behavior of the system. However, in the SSE method, the number of operations required for the sampling updates becomes prohibitive as temperature is decreased [34]. Nevertheless, as we saw in Section. 3.3, the energies of the excited states for a finite system exhibit a gap with respect to the ground state. This gap decreases in an isotropic system, where $z = 1$, as $1/\sqrt{N}$ (see Eq. (3.49)).

Thus, because of this gap in the excitations for finite systems, the finite temperature effects should become unimportant, not only at $T = 0$ but at small temperatures as well. Since we are motivated to consider $z = 1$ for our system, the temperature we choose should scale down with system size as $1/\sqrt{N}$. Therefore, we will be using the relation

$$\frac{T(N_1)}{T(N_2)} = \frac{\sqrt{N2}}{\sqrt{N1}}, \tag{4.4}$$

to choose the temperatures for different system sizes.

In Fig. 3.47 we plot the value of the Binder cumulant against h for system sizes separated by a multiplicative factor of Φ^2. For these system sizes the distribution of the J includes a peak as the one indicated by the continuous arrow in Fig. 2.9. The crossing points, h_{cross}, do not converge for these system sizes. In particular, as we increase N the h_{cross} do not come closer to each other. Therefore, this indicates that finite-size scaling theory, as we described it, is not applicable. These 4 points do not fit in a $N^{-\omega}$ fit, where ω is a positive number. However, we should note that the region of h we are plotting is very restricted and the crossings differ up to the second important decimal.

In addition to that, the value of the Binder cumulant drops drastically for these crossing points. At the last crossing point the value of the U_4 is very small. However, as U_4 approaches 0, we would have $\langle M^4 \rangle \approx 3\langle M^2 \rangle$. This indicates a Gaussian distribution for the magnetization, [35]. This is also not what one would expect for an Ising system of dimension D = 2 + 1 = 3 [17] at criticality.

As noted, the temperature used for the plots of Fig. 4.3 is $\beta = 2\sqrt{N}$. We verified that the results are not artifacts of the choice for β. In particular, we checked that for the small system sizes, $N = 323$ and 828, the value of the Binder cumulant saturates to its zero temperature value around $\beta = 9\sqrt{N}$. Nevertheless, upon decreasing the temperature further than $\beta = 2\sqrt{N}$, for all system sizes considered, we saw no substantial difference in the values of h_{cross} of the crossing points. The value of U_4 did exhibit slight decrease as the temperature was lowered.

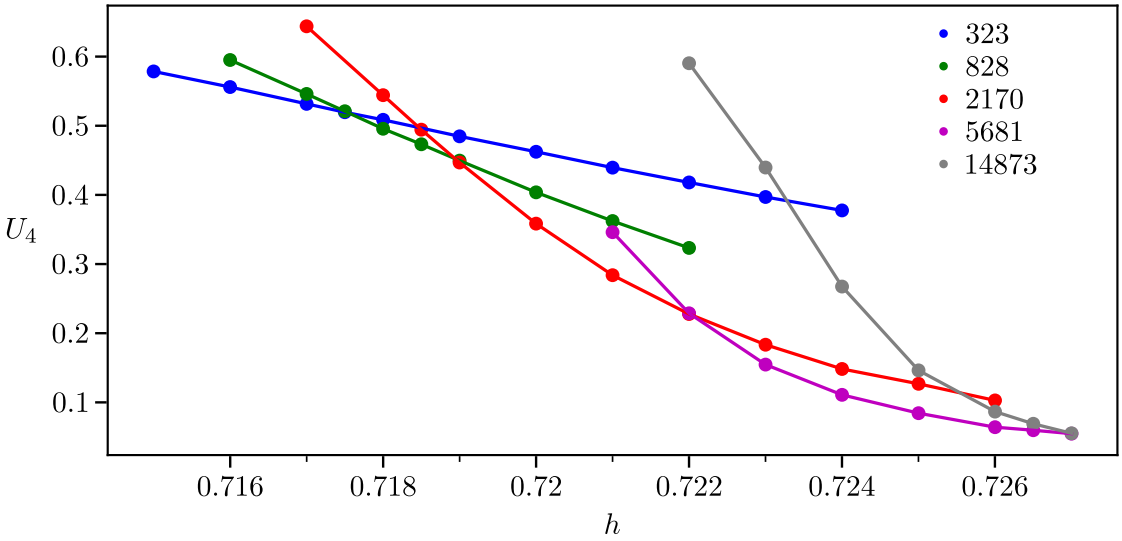

Figure 4.3: Binder cumulant of the TFIM on the *NN* Fibonacci lattice. The system sizes, N, related by a multiplying factor $m\Phi^2$ at $\beta = 2\sqrt{N}$. The colors indicate the different N. The statistical behavior of the J is similar for all N. The crossings points, h_{cross}, are the intersections of the lines of *consecutive* system sizes, that is between system sizes related by φ^2 (for example 323 with 828 and 828 with 2170). The 4 crossing points do not converge with system size. This indicates a different picture to the one proposed through the heuristic finite-size scaling theory. These 4 points do not fit in a $N^{-\omega}$ fit, where ω is a positive number. In addition, the value of the Binder cumulant drops drastically between the crossing points. This should imply that we are still not comparing similar systems. The coordination number "statistics" however do become more similar with increasing system size as described in App. C.

The finite-size effects are, therefore, very pronounced in our system. One essential aspect that might explain this is the difference in percentage of lattice sites with 6 neighbors between the different system sizes. We know, from mean field theory, that the critical point is linearly related to the coordination number [17]. Even though the critical regime is not described by mean field theory, it has been numerically confirmed that the coordination number does affect the value of the critical point. Flat 2D TFIM on different lattices (square, triangular, hexagonal), exhibit a different critical point as shown in [36].

This might explain why the crossing points do not converge. It could be that, in order to compare actually similar lattices, we would have to go to even larger system sizes. More particularly, as indicated in Fig. C.1, the percentage of lattice sites with 6 neighbors progressively saturates as system size is increased.

It is of interest to note that finite-size effects appear also on the classical Ising model on the sphere, which is studied by setting $h = 0$. We plot the Binder cumulant with

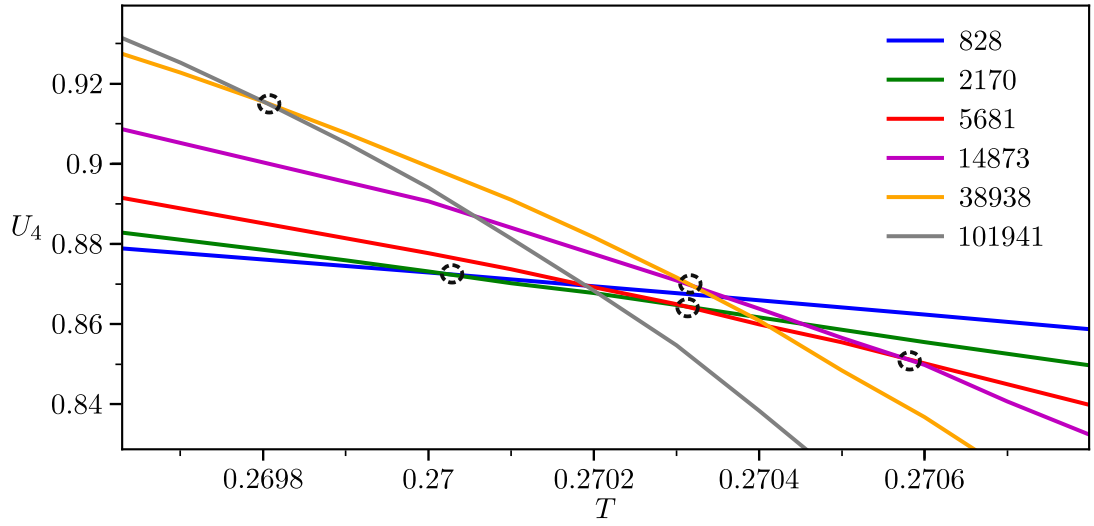

Figure 4.4: Binder cumulant for system sizes, N, related by a multiplying factor $m\Phi^2$ for the classical system where $h = 0$. The statistical behavior of the J is similar for all N. The crossing points are indicated by the dashed circles. The 5 crossing points do not converge with system size. They exhibit a non-monotonic behavior. The value of the Binder cumulant does not differ substantially between the different crossings. In fact, the crossing between $N = 38938$ and $N = 101941$, yields $U_4 \approx 0.916$. This is very close to the value of the Binder cumulant for the 2D Ising models with periodic boundary conditions [37]. However, this is probably a coincidence since there are no converging crossings to verify our result. The regime of finite-size scaling in the system may be obtained *at least* for linear sizes of the order of magnitude of $L \geq \sqrt{5681} \approx 75$. This follows, since the change in the monotonicity of the crossing points appears at the crossing of 5681 and 14873. The 75 is more an order of magnitude than an actual value.

respect to the temperature in Fig. 4.4. The crossings all appear in a very narrow region of temperatures around $T \approx 0.27$. We note that the critical value of the triangular flat Ising model is $T_c \approx 0.273$ [37]. To find this, we used the relation $T_c = 3.64J$ [37], our mean $\langle J \rangle \approx 0.3$ (the $\langle J \rangle$ is not the exactly the same between system sizes) and a division by 4 since we are considering spin-1/2 in Eq. (4.1).

However, the temperatures at the crossing points do not exhibit a monotonous behavior in Fig. 4.4. The various T_{cross} initially increase with system size and then at the crossing between system sizes $N = 14873$ and $N = 38938$ they decrease. The value of the Binder cumulant does not vary substantially between the different crossings.

In fact, the crossing between $N = 38938$ and $N = 101941$, yields $U_4 \approx 0.92$. This is very close to the value of the Binder cumulant for the 2D Ising models with periodic boundary conditions and shape such as the two directions essentially include the same number of lattice points. The value $U_4 \approx 0.915$ is found in [37]. To properly compare our

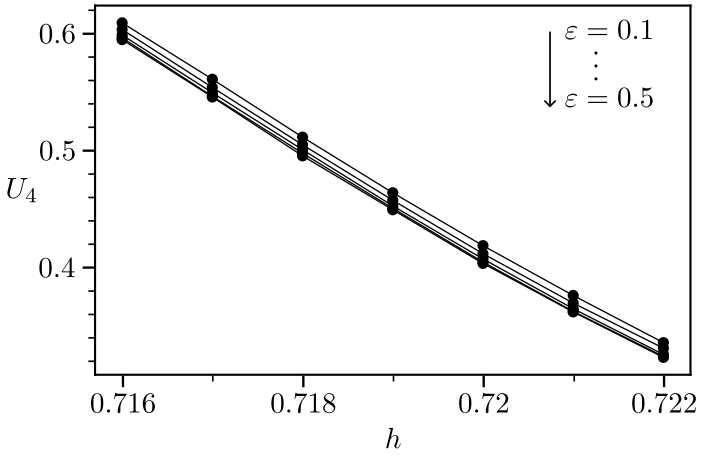

Figure 4.5: Binder cumulant values for different perturbations of the Fibonacci lattice for $N = 828$. For the different perturbations, we vary ε in Eq. (2.15). We plot for $\varepsilon = 0.1, 0.2, \ldots, 0.5$. The maximum variation in the values of U_4 is of the order of 2% with respect to their mean value. As ε approaches 0.5 the curves essentially converge.

results to [37] we should account for the factor 3/2 due to our definition of the Binder cumulant, Eq. (3.47).

However, since our result has not been verified with any finite-size scaling convergence (more crossings), it is probably accidental. Nevertheless, we see a similarity in the value of the crossing with the quoted one. The Ising model on the sphere does not have periodic boundary conditions in the sense of the models studied in [37]. It can, perhaps, be interpreted to have periodic boundary conditions along the azimuthial direction if we choose an axis of rotation. Moreover, we can make this consideration for any choice of the axis. This might explain the similarity between our result and the universal value of the Binder cumulant in such systems.

We can motivate that the regime of finite-size scaling in the sphere may be obtained *at least* for linear sizes $L \geq \sqrt{5681} \approx 75$ since the change in the monotonicity of the crossing points appears at the crossing of 5681 and 14873. The 75 should actually be an order of magnitude rather than an actual value. This might, also, partially explain the behavior of the crossings for the quantum model. Only the last crossing corresponds to the linear sizes, for which finite-size scaling may even begin to be relevant.

We should, also, check if the finite-size effects for the quantum Ising model relate to the particular choice of the lattice perturbation, in the sense discussed in Section. 2.1. The choice for our lattices up to now corresponds to $\varepsilon = 0.5$ in Eq (2.15). We motivated, through Tb. 2.3, that the solution with better spectrum is the one with ε around 0.5.

Nevertheless, it is worthwhile to evaluate if the Binder cumulant is affected by changing ε. We saw in Fig. 2.10 that the differences in the bulk behavior of the J for different ε

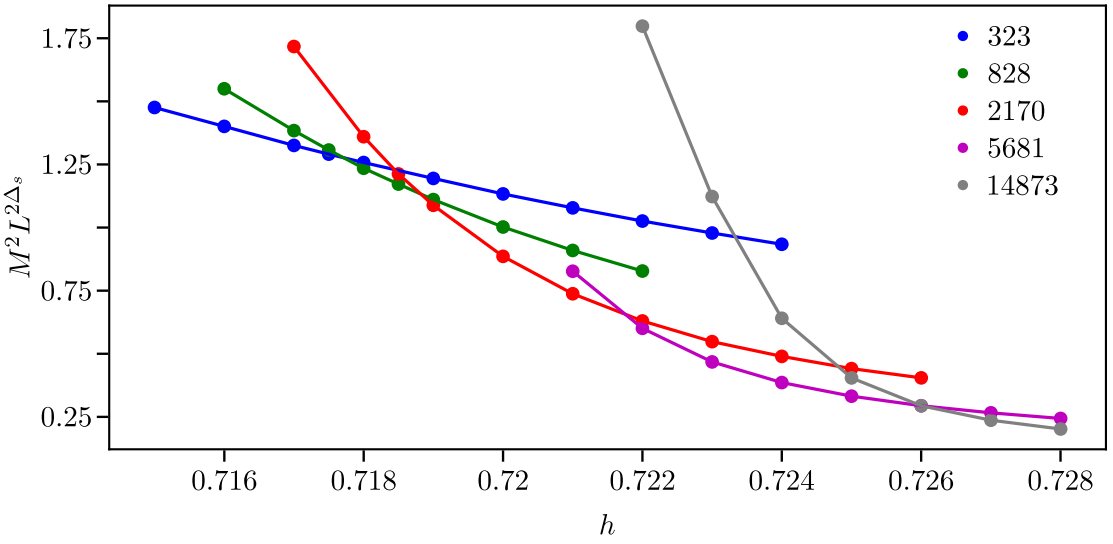

Figure 4.6: Rescaled Magnetization of the TFIM on the *NN* Fiobanacci lattice. The system sizes are related by a factor $m\Phi^2$. The statistical behavior of the J is similar for all N. Here, the linear size is given by $L = \sqrt{N}$ and the temperature is $\beta = 2L$. Here, the value of the exponent, $\Delta_s = 0.518$, is the value found for the 3 dimensional Ising universality class [38], [39]. The crossing points, h_{cross}, are coarsely similar to the ones in Fig. 4.3.

decrease with system size. Therefore, to see more pronounced effects, we plot different perturbations, ε, for $N = 828$ in Fig. 4.5. The maximum variation in the values of U_4 is of the order of 2% with respect to their mean value. Nevertheless, these changes cannot explain the drastic differences in the value of U_4 at the different crossing points.

Although the finite-size effects are pronounced for the spherical TFIM, there is indication that we are indeed locally approximating the flat 2D transverse-field Ising model. To see this, we make use of the scaling exponents of the 2D transverse-field Ising model. In Fig. 4.6 we plot the rescaled magnetization squared, $M^2 L^{2\Delta_s}$, using $L = \sqrt{N}$ and $\Delta_s = 0.518$ [38]. We again use $\beta = 2\sqrt{N}$. With this choice for Δ_s, the crossing points are very close to the ones found in the U_4 plot. However, we cannot resolve the scaling dimension Δ_s with sufficient precision. Choosing $\Delta_s = 0.5$ also gives similar results. Nevertheless, the crossing do look qualitatively different if we choose for example $\Delta_s = 0.4$ or $\Delta_s = 0.6$.

As discussed in Section. 3.3, the concept of universality is assumed, also, for the finite-size scaling. If that is to hold, the value of the Binder cumulant should be universal at the critical point. In our case, we cannot pinpoint a critical point. However, we can collapse the curves of *consecutive* system sizes (that is for example 323 and 828) onto each other, if we plot the Binder cumulant with respect to $(h - h_{cross})L^{1/\nu}$, Fig. 4.7. The $\nu = 0.63$ follows from the value at the 3 dimensional Ising universality class [38].

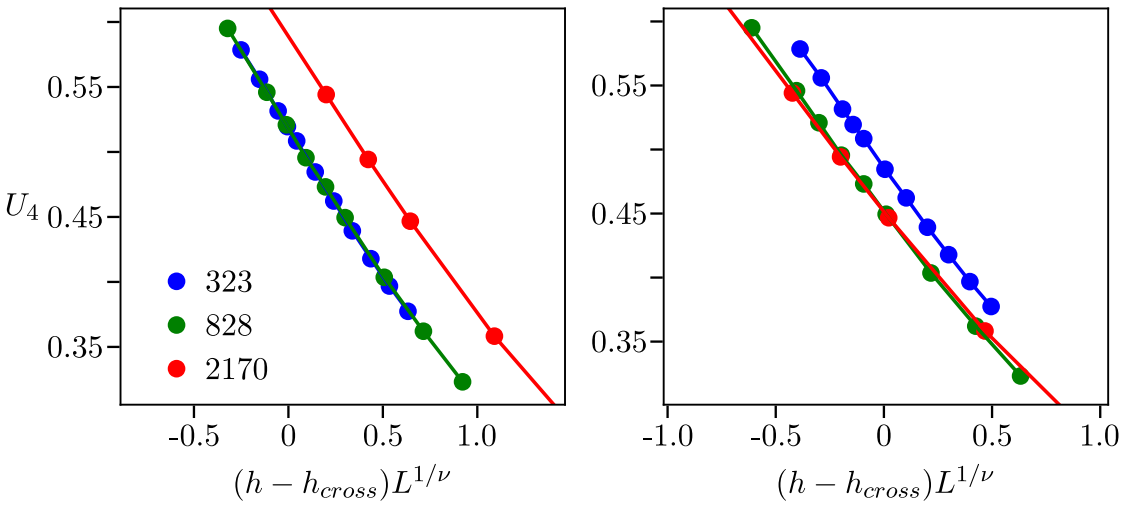

Figure 4.7: Collapsing Binder cumulant curves by plotting with respect to $(h - h_{cross})L^{1/\nu}$. Here, $L = \sqrt{N}$ and $\beta = 2L$. The h_{cross} are the crossing points of (323,828) and (828,2170) respectively for the plots, from left to right. Although the system sizes are relatively small and a critical point is not found, the plots indicate that it may still be relevant to rescale the crossings points with the exponent, $\nu = 0.63$, of the 3 dimensional Ising universality class [38]. This is still a coarse argumentation, as we do not have the resolution to infer the exact value for ν in our system, primarily due to the lack of a critical point.

The collapse becomes worse as we vary the value of ν to nearby values, such as 0.5 or 0.7. However, we note again, that we do not have the resolution to determine ν as we do not have a converging critical point.

Chapter 5

Conclusions and Outlook

The thesis investigated the free particle problem on the sphere and attempted to construct a spherically symmetric transverse-field Ising model, to be studied at criticality. In Ch. 2 we studied the free particle problem. Firstly, we created the tight-binding Hamiltonian of the model. As it is known, its Hamiltonian is directly proportional to the Laplacian. Thus, the hopping terms, J, of the tight-binding model, Eq. (2.29), were derived by discretizing the Laplacian and solving the corresponding system of linear equations using the neighboring distances of the lattice sites, Eq. (2.28). The code we set up for this can be straightforwardly applied to any lattice put on the sphere. We are interested in lattices that can easily scale up in size.

For the purposes of the thesis, we compared two such lattices. These were the icosahedron-seed and the Fibonacci lattice. Evaluating the spectra of the Hamiltonian for the two configurations, we concluded that the free particle's expected $SO(3)$ symmetry is recovered more quickly on the Fibonacci lattice. The difference between the two cases is that the icosahedron-seed seems to substantially retain the original icosahedral symmetry. This is observed by the degeneracies the systems exhibit on their spectrum in Fig. 2.6. The Fibonacci lattice on the other hand, being an "amorphous" geometry, has no symmetry constraint. This observation may suggest a more general conclusion. Namely, that there is an advantage in using (reasonably uniform) lattices that have no underlying symmetries, such as the Fibonacci lattice, in order to achieve true spherical symmetry for physical systems.

Furthermore, we understood the limitations the geometry of the Fibonacci lattice imposes on the spectrum. More specifically, it is possible to resolve the approximately degenerate energy levels up to the level for which the angular momentum quantum number is $l \approx \sqrt{N}/2$. This is shown in Fig. 2.13. It is explained by the fact that there is a minimum angle by which we can rotate the lattice so that it (approximately) maps to itself. The minimum angle scales down with system size as $\propto 1/\sqrt{N}$. This, as shown in Eq. 2.35, imposes a constraint on how many different L^z numbers, m, we can resolve.

In principle, we begin to not able to discern the m at energy levels for which $l \gtrsim \frac{\sqrt{N}}{2}$.

In addition, the subtleties of the underlying geometry affect the behavior of the hopping terms, J. As shown in Fig. 2.7, the J have the same dependence with respect to the distance between nearest neighbors, for all system sizes. However, the nearest neighbor distances themselves vary as we change the number of lattice sites, N. This can be seen from the histogram in Fig. 2.7, where the predominant nearest neighbor distances have different percentages for the different N. We observed that similar Fibonacci geometries only appear between lattice sizes that are related by a multiplicative factor of Φ^2, where Φ is the golden ratio. A histogram for the J has the same behavior between lattices sizes N and $\Phi^2 N$, as shown in Fig. 2.8.

It should be noted that the variations of the J at different N do not seem to be important in the realization of the Laplacian. In other words, even though the statistical distribution of the J is not the same, they are all used to explicitly construct the Laplacian and we observed no indication or peculiarity in the spectrum that can be traced back to different J statistics. However, we also used the hopping terms as interactions coefficients in defining the transverse-field Ising model (TFIM) on the sphere. We did so motivated by the fact that the J do, in general, contain the information of rotational symmetry that is characteristic to the Laplacian. In the case of the TFIM, the variations of the J should, in principle, matter.

The quantum phase transition of the TFIM and the motivation to study it on a sphere were explained in Ch. 3. In particular, the transverse-field Ising model at criticality exhibits $\mathbb{Z}_2$ symmetry breaking. Due to the quantum to classical mapping, one can infer the nature of the quantum phase transition by the phase transition of the classical Ising model in a dimension higher, $D = d + 1$ [17]. The energy excitations in the quantum model are linearly related to the correlation length of scaling fields, φ, of the classical model. The $d = 2$ TFIM on a sphere can be mapped to the $D = 3$ classical model where the third (time) direction is infinite. This yields the effective geometry $S^2 \times \mathbb{R}$.

Moreover, the Ising model is suspected to exhibit conformal symmetry at its critical point. As elaborated further in App. B, there is a prediction according to which the correlation length of the correlation function of φ on the $S^2 \times R$ geometry is directly related to its scaling dimension (Δ) [12]. This finite-size scaling prediction is given by $\xi = \frac{R}{\Delta}$ where ξ scales linearly with the sphere radius. This motivates the more general prediction, where the energy spectrum of the quantum Hamiltonian may be classified according to the spectrum of the generator of dilations [30], [16]. The eigenstates should, also, have a corresponding l quantum number.

Motivated to study the TFIM on the sphere, we defined its Hamiltonian in Ch. 4 as

$$\mathrm{H} = -\sum_{\langle ij \rangle} J_{ij} S_i^x \otimes S_j^x - h \sum_i S_i^z, \tag{5.1}$$

where J_{ij} are the free particle hoppings. We firstly evaluated if using this Hamilto-

nian, instead one where the J are constant, is better for recovering the degeneracies of the $SO(3)$ symmetry. We plotted the low energy spectrum for both cases and saw an improvement with our proposition. The approximate $SO(3)$ degeneracies we observed were up to $l = 2$. This should be expected due to the geometric constraints explained in Ch. 2. Furthermore, we motivated, through a long wavelength expansion, that the Eq. (5.1) is locally equivalent to the flat $d = 2$ TFIM.

In order to study the system at criticality, we attempted to find its critical point. We did that by using the Binder cumulant, U_4, which is known to exhibit no scaling with system size (at least to leading order) near the critical point [35]. Converging crossing points of Binder cumulant curves plotted with respect to h for different system sizes should yield a critical point. After some numerical experimentation, we noticed substantial variations in h between the crossing points. To improve the situation, we, then, compared locally similar systems with system sizes given in steps, $N, \Phi^2 N, \Phi^4 N...$ as explained in Ch. 2. This yielded intersections of the curves that were all relative close to $h = 0.72$.

However, still no converging behavior was noticed and, between the intersections, the value of U_4 drastically varied, as shown in Fig. 4.3. This was understood to be related to severe finite-size effects not captured in the context of the finite-size scaling theory explained in Ch. 3.3. In specific, it is possibly related to the fact that, even though the systems were locally similar, the number of sites with 6 neighbors, c_6, was different for the system sizes. In particular, the coordination number c_6 has a non-smooth behavior with respect to the system size as explained in App. C. Each system size belongs to a different segment of Fig. C.1.

Trying to explain this result further, we plotted the Binder cumulant with respect to the temperature for the classical Ising model on the sphere, by setting $h = 0$. In this case, the effective geometry was simply S^2. The crossing points of the curves were concentrated around a value which was reasonably close to the critical temperature of the triangular flat lattice. This result is expected, since c_6 is dominant in our lattice. The value of U_4 did not exhibit drastic changes between the crossing and was relatively close to the universal value it has for systems with symmetric geometry, $L \times L$, and periodic boundary conditions [37]. Nevertheless, the intersections of the curves showed a non-monotonous trend. The linear system sizes, $L = \sqrt{N}$, for which the monotonicity changes correspond to the largest ones we evaluated for the quantum model. This might suggest that we were still considerably away from the regime where finite-size scaling theory is applicable. So any result, such as the value of the Binder cumulant, cannot be robustly confirmed.

As we saw, the differences in the underlying lattice persist even for large lattice sizes. These do yield severe finite-size effects when comparing even seemingly similar systems. To alleviate this, one should use even more uniform distributions of points on the sphere that follow from optimizations. Having tried to implement our free particle solver on large lattices that are numerical solutions of the Thomson problem, we found both

a better spectrum (more approximately degenerate energy levels) as well as a more concentrated distribution for the J around a single value. Unfortunately, such lattices require a computational cost which makes scaling up not straightforward. Future work should then be in the direction of investigating and using spherical lattices with more uniform distribution of points.

In addition, in the search for the critical point, we considered a region of h (or of the temperature in the classical case) where the crossings may differ in the third significant digit (or fourth in the classical case). This is evident in Fig. 4.3 and 4.4. One can notice that a seemingly small rescaling (a multiplicative factor that differs to 1 in the third or fourth digit) of the couplings J could lead to a considerable shift in a crossing point. Such rescalings are relevat because the similarity of different system sizes is not guaranteed in our irregular lattices and it depends also on the correct determination of the J through Eq. (2.28), which we solve numerically. In the future, we can try fixing the value of $\langle J \rangle$ for all sizes. We may also demand that in Eq. (2.27) the right hand side is not the same for all system sizes and depends on the (statistically averaged) lattice spacing found for each system size. These brute force corrections are motivated by the fact that in a regular lattice they are trivially satisfied. It is not obvious, however, if they would help "regularize" our systems more, since we attempted to do so anyway with solving the Laplacian.

Appendices

A Euler Characteristic for the sphere

The following property and proof are attributed to Euler.

There can be no polyhedron with symmetrically distributed sites and identical faces for arbitrary number of sites.

Consider points on a plane that are all connected by edges and no two edges intersect. An example is shown in Fig. A.1. This is a *planar graph*. Then, we define the Euler characteristic $\mathcal{K}$ as

$$\mathcal{K} = V - E + F. \tag{A.1}$$

V is the total number of vertices (or sites or points), E the total number of edges (or segments) and F the total number of faces.

Consider a specific initial graph and a constant number of vertices V. Adding an edge, between two points, that does not intersect an already existing one, produces one more face. Therefore, it holds that $F - E$ remains constant as we add edges. From this follows, $\mathcal{K}$ = const, for specific initial configuration and V = const. Next, we add a vertex anywhere on the plane. This does not yet change $\mathcal{K}$, because the new vertex is not connected to the graph and thus is not part of it. To connect it, we add one edge. As long as it is only one edge that is connected to the new vertex, we have no additional face. Therefore $V - E$ is constant. Adding another edge, creates a face but keeps $F - E$ constant as explained above. Therefore, $\mathcal{K}$ = const, for specific initial graph.

We can start with a planar graph with three vertices. By counting we see that no matter how many edges or faces the initial graph has $\mathcal{K} = 2$. We should note that in this counting we also add +1 face which represents the outer surface. For example, the outer surface is the exterior surface of the polygon created by the red vertices in Fig. A.2. We can create all possible planar graphs from corresponding graphs with three vertices. Therefore, by adding vertices and edges, $\mathcal{K}$ remains constant. So, we have

$$\mathcal{K} = 2 \quad , \quad \text{for planar graphs.} \tag{A.2}$$

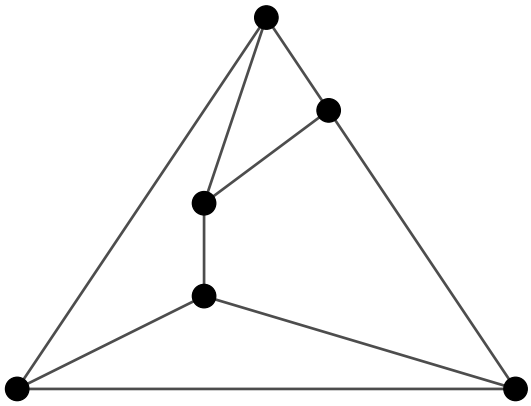

Figure A.1: A planar graph with 6 vertices.

To make a discrete sphere, we consider convex polyhedra. In Fig. 2.2 we can see the faces of such a polyhedron. As is inferred visually, for convex polyhedra, a line connecting any two points, that do not lie on the same face, always lies in the interior of the polyhedron. Every convex polyhedron can be laid in the plane as a connected planar graph. More specifically, we can map the polyhedron and its faces to the plane. In order to be consistent though, in mapping to the plane one should exclude a single vertex and all the edges that connect to it. This vertex is considered to be the north pole which maps to infinity on the plane. In counting for $\mathcal{K}$ in the resulting planar graph, we will add $+1$ representing the missing vertex instead of adding $+1$ for an additional face as we did before.

Therefore for a convex polyhedron produced by a tessellation procedure on the sphere, $\mathcal{K} = 2$. With this constraint, we can examine if a convex polyhedron has a single repeating face. We follow [5].

In triangulating, let n_k be the number of vertices that give rise to k edges. Then

$$V = \sum_k n_k \tag{A.3}$$

$$E = \sum_k \frac{1}{2} k n_k \tag{A.4}$$

$$F = \sum_k \frac{1}{3} k n_k \tag{A.5}$$

The relation for the faces comes from the fact that a vertex connected to k edges belongs

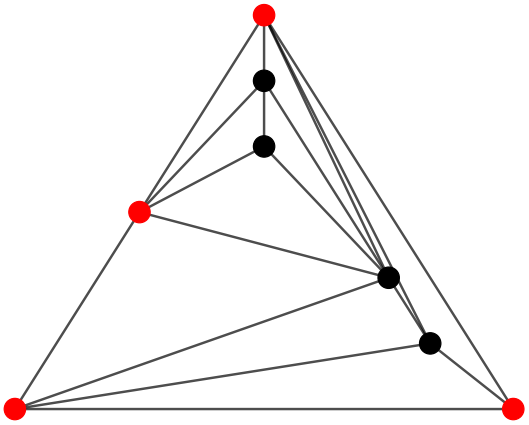

Figure A.2: A planar graph with 8 vertices. The statement *a vertex connected to k edges belongs to k triangles* does not hold for the red vertices. However, when we map back to the sphere, new edges are created either between red vertices or between the red vertices and the additional vertex we named as north pole. Then this statement holds.

to k triangles. There are n_k such vertices in total. If one considers the sphere represented as a planar graph, then it is not clear why this should hold for the outermost vertices. For example, this statement does not seem to hold for the red vertices in Fig. A.2. This discrepancy is related to the fact that in order to properly count, we map a sphere to a plane and the outermost vertices (red in Fig. A.2) might connect to the vertex which is mapped to infinity. The factor $\frac{1}{3}$ indicates that a single vertex makes up one third of each triangle. Consistently, if we tessellated with rectangles or pentagons this factor would be $\frac{1}{4}$ and $\frac{1}{5}$ respectively, while the expressions for V and E would be the same.

Substituting Eqs. (A.3) to (A.5) in Eq. (A.1), the Euler characteristic is given by

$$\mathcal{K} = \sum_k \left(1 - \frac{k}{6}\right) n_k = 2. \tag{A.6}$$

To make a uniform covering with triangles we would, at least, need all vertices to connect to the same number of edges. That means that we have to see if Eq. A.6 is satisfied for a specific k. In other words, examine if $\mathcal{K} = \big(1 - k/6\big) n_k = 2$, can be satisfied. Evidently

for $k \geq 6$ we have $\mathcal{K} \leq 0$. For the rest we have,

$$k = 3, n_k = 4 \rightarrow \text{regular tetrahedron},$$
$$k = 4, n_k = 6 \rightarrow \text{regular octahedron},$$
$$k = 5, n_k = 12 \rightarrow \text{regular icosahedron},$$

where we indicate the regular polyhedra that satisfy these constraints. We see that there can be no polyhedron with more than 12 vertices which has identical triangular faces. Correspondingly, it is easy to check that there can be no polyhedron with more than 8 vertices which has identical square faces and no polyhedron with more than 20 vertices with identical pentagonal faces.

B Conformal transformations

B1 Transformation of the metric

In the main text we saw that the ds^2 of $\mathbb{R}^3$ and $S^2 \times \mathbb{R}$ are related by the transformation of Eq. (3.60). In fact, they are related by a prefactor that depends on position. Such a prefactor will be generally denoted as $\Omega(\boldsymbol{x})$. In this section we will explain in more detail the conformal transformations from the viewpoint of the transformation of the metric.

In order to see how a conformal transformation comes about consider first the (simpler) scale transformation, under which lengths l, transform as ; $l \rightarrow \sqrt{\Omega} l$. Since it is a dilation, Ω is independent of $\boldsymbol{x}$. Vectors defined on the original geometry should be dilated as well. Therefore, the length squared of the infinitesimal dx^μ, which is found through

$$ds^2 = g_{\mu\nu} dx^\mu dx^\nu \tag{B.1}$$

should be rescaled by a factor Ω as

$$ds^2 \rightarrow \Omega ds^2. \tag{B.2}$$

The general conformal transformations induce

$$ds^2 \rightarrow \Omega(\boldsymbol{x}) ds^2. \tag{B.3}$$

We should clarify that in order to reach these results we did more than a coordinate transformation. More specifically, if we had done only a coordinate transformation then both the metric $g_{\mu\nu}$ and the dx^μ would have been transformed. That is

$$g'_{\mu\nu} = \frac{\partial x^\alpha}{\partial x'^\mu} \frac{\partial x^\beta}{\partial x'^\nu} g_{\alpha\beta}, \tag{B.4}$$
$$dx'^\mu = \frac{\partial x'^\mu}{\partial x^\alpha} dx^\alpha. \tag{B.5}$$

We can confirm that

$$g_{\mu\nu}dx^{\mu}dx^{\nu} = g'_{\mu\nu}dx'^{\mu}dx'^{\nu}. \tag{B.6}$$

Then, in order to obtain Eq. (B.2) or Eq. (B.3), we can do one more step and rescale the transformed metric as $g'_{\mu\nu} \to \Omega(\boldsymbol{x})g'_{\mu\nu}$. This is called a Weyl rescaling. Therefore, in total, a conformal transfromation induces the change of metric

$$g'_{\mu\nu} = \Omega(\boldsymbol{x})\frac{\partial x^{\alpha}}{\partial x'^{\mu}}\frac{\partial x^{\beta}}{\partial x'^{\nu}}g_{\alpha\beta}. \tag{B.7}$$

Consider the flat space metric, denoted $g_{\mu\nu} = \eta_{\mu\nu}$. We demand the condition that the metric remains invariant under the transformation, $g' = g$ (so the flat space is mapped to itself). From this, one can deduce that the allowed coordinate transformations, for $d = 3$, are the four infinitesimal transformations we described in Ch. 3.4 [22]. That is the translation, rigid rotations, dilations and SCTs.

One can also confirm that the finite version of these transformations map the plane to itself. Specifically, in the case of the finite SCT we have

$$x'^{\mu} = \frac{x^{\mu} - x^2 b^{\mu}}{1 - 2b \cdot x + b^2 x^2}. \tag{B.8}$$

The $x = 0$ is mapped to itself. The point b^{μ}/b^2 is mapped to ∞ and the point $x \to \infty$ is mapped to the value -b^{μ}/b^2. So, we need to include a point at ∞ to make sense of the mapping of the geometry to itself in the case of SCTs.

The coordinate transformation of Eq. (3.59) resulted in Eq. (3.60), according to which

$$ds_{\mathbb{R}^3} = \frac{1}{R^2}e^{2u/R}ds_{S^2\times\mathbb{R}}. \tag{B.9}$$

In this case, a Weyl rescaling by $\Omega(r) = R^2e^{-2u/R} = R^2/r^2$ would give

$$ds_{\mathbb{R}^3} \to \Omega(r)ds_{\mathbb{R}^3} = ds_{S^2\times\mathbb{R}}. \tag{B.10}$$

Using Eq. (B.7) and this $\Omega(r)$ we can confirm that in this case the metric is not mapped to itself. This might seem obvious since the geometries are different. However, we can motivate a specific feature in the case of $d = 2$.

The coordinates are given by $z = re^{i\theta}$. The conformal transformation would be $z \to w(z) = R/2\pi \ln(z)$. It is analytic everywhere except for the origin. For $w = u + iv$ we see that $u = \ln(r)$ and $v = iR\theta/2\pi$. If we allow θ to take any value (and not be restricted to let's say $[0, 2\pi)$) then w should again span all the complex plane. However, it is necessary to enforce a constraint on the functions $f(z) = f(r, \theta)$ since they should be single valued for $\theta' = \theta + 2\pi$ and θ.

This condition corresponds to periodicity of the functions in the transformed plane $z \to w$ along the v direction. We should note that the transformation $\ln(z)$ is not the

same as $u \sim \ln(r)$ (the prefactor can be adjusted) we had in Eq. (3.59). Nevertheless, due to the periodic boundary conditions it allows for the same cylinder interpretation as the corresponding transformation of Eq. (3.59) for $d = 2$. At the same time though, for practical purposes and intuition, it can map the complex plane to itself and not on a different geometry.

From Eq. (B.7) one can see that angles are preserved (locally) in conformal transformations. More specifically, the normalized inner product of two vectors u^μ and w^ν,

$$cos(\theta) = \frac{g_{\mu\nu}u^\mu w^\nu}{\sqrt{g_{\mu\nu}u^\mu u^\nu}\sqrt{g_{\mu\nu}w^\mu w^\nu}}, \tag{B.11}$$

stays invariant in the conformal transformation since the factor $\Omega(\boldsymbol{x})$ cancels between the numerator and the denominator.

B2 Covariant transformation of the correlation functions

The question that arises in the main text is for which field and transformations we expect Eq. (3.56) to hold. In this appendix we explain how this transformation comes about for fields that are scalar under rotation. We use group theoretic arguments.

The conformal transformations are the translation, the dilation, the rigid rotation and the special conformal transformation (SCT). The generators of the transformations have the following form when they act on the coordinates,

$$P_\mu = -i\partial_\mu \tag{B.12}$$
$$D = -ir^\mu\partial_\mu \tag{B.13}$$
$$L_{\mu\nu} = i(r_\mu\partial_\nu - r_\nu\partial_\mu) \tag{B.14}$$
$$K_\mu = -i(2r_\mu r^\nu\partial_\nu - \boldsymbol{r}^2\partial_\mu). \tag{B.15}$$

These infinitesimally transform the coordinates as

$$r'^\mu = r^\mu + i\alpha U r^\mu, \tag{B.16}$$

where the U are exactly the expressions in Eqs. (B.12)- (B.15) and the form of α depends on the transformations. In translations and dilations, for example, it is a small positive number (it is not complex!). We clarify this here as to avoid possible confusions with the signs later on.

Using Eqs. (B.12) through (B.15), one can derive the commutation relations of the generators of the transformations *on the coordinates*. To be more succinct here, the commutation relations that are relevant in our discussion are the following,

$$[D, P_\mu] = iP_\mu, \tag{B.17}$$
$$[D, K_\mu] = -iK_\mu, \tag{B.18}$$
$$[D, L_{\mu\nu}] = 0. \tag{B.19}$$

What is important about using the conformal algebra is that we can carry over the results and understand the conformal transformations of correlation functions. However, as we will see there are subtelties introduced on the commutation relations when we consider operations on fields.

We will treat the transformations as active transformations [22]. We illustrate what we mean with examples. In an active translation where $\boldsymbol{r} \to \boldsymbol{r} + \boldsymbol{a}$ the field $\varphi(\boldsymbol{r})$ would transform as

$$\varphi(\boldsymbol{r}) \to \varphi'(\boldsymbol{r}) = \varphi(\boldsymbol{r} - \boldsymbol{a}). \tag{B.20}$$

This would then mean that the new field is really the same as the old field just shifted. We could also equivalently state $\varphi'(\boldsymbol{r}') = \varphi(\boldsymbol{r})$. However, when it comes to rotations, for example, where we consider $r'^{\mu} = \Lambda^{\mu}_{\nu} r^{\nu}$ through the rotation matrix Λ, we have

$$\varphi(\boldsymbol{r}) \to \varphi'(\boldsymbol{r}) = L_{\Lambda}\varphi(\Lambda^{-1}\boldsymbol{r}). \tag{B.21}$$

We notice that it is not only the shifted coordinates that appear but also this L_{Λ} in front of the field. So, in this case, $\varphi'(\boldsymbol{r}') = L_{\Lambda}\varphi(\boldsymbol{r})$. That means a transformation L_{Λ}, called functional transformation, is induced on the field itself. That is, it would also happen at $\boldsymbol{r} = 0$. If L_{Λ} is not trivial (equal to 1) then the field has spin. Correspondingly, the field itself will, in principle, change non-trivially (under a functional transformation) also under dilations and rotations [22]. The shift in coordinates is always there. The fields changing non-trivially is what eventually gives us the prefactors depending on $b(\boldsymbol{r})$ in Eq. (3.56). So, in active transformations we have $\varphi'(\boldsymbol{r}') = (\text{something})\varphi(\boldsymbol{r})$, where this something would act on the field itself and would be there even at $\boldsymbol{r} = 0$.

We want to see how the generators of the conformal transformations act on fields. Since there are extensive bibliographical references for this, we will quote the results. However, before we do that, we will attempt to clarify a subtle point, pertaining to how the commutation relations of the generators look like for field transformations. Namely, we will argue that, for example,

$$[D, P_{\mu}]\varphi(\boldsymbol{r}) = -iP_{\mu}\varphi(\boldsymbol{r}), \tag{B.22}$$

where we see a minus sign compared to the commutation for the coordinates in Eq. (B.17).

To find the commutator we have to induce a translation and a dilation on the field. As discussed, these correspond to $\varphi(\boldsymbol{r}) \to \varphi(\boldsymbol{r} - \boldsymbol{a})$ and $\varphi(\boldsymbol{r}) \to \varphi\left(\frac{\boldsymbol{r}}{1+b}\right)$ respectively. We assume that there is no prefactor in front of φ for the dilations (the field has zero scaling dimension) for ease of calculations. So, if we consider the operations

$$e^{-ia^{\mu}P_{\mu}}\varphi(\boldsymbol{r}) = \varphi(\boldsymbol{r} - \boldsymbol{a}), \tag{B.23}$$

$$e^{-ibD}\varphi(\boldsymbol{r}) = \varphi\left(\frac{\boldsymbol{r}}{1+b}\right) \tag{B.24}$$

we surmise that

$$P_{\mu}\varphi(\boldsymbol{r}) = -i\partial_{\mu}\varphi(\boldsymbol{r}), \tag{B.25}$$

and

$$D\varphi(\boldsymbol{r}) = -ir^{\mu}\partial_{\mu}\varphi(\boldsymbol{r}), \tag{B.26}$$

for zero scaling dimension. Next, we consider the transformation

$$\left(e^{-ibD}e^{-ia^{\mu}P_{\mu}} - e^{-ia^{\mu}P_{\mu}}e^{-ibD}\right)\varphi(\boldsymbol{r}) = \varphi\left(\frac{\boldsymbol{r}-\boldsymbol{a}}{1+b}\right) - \varphi\left(\frac{\boldsymbol{r}}{1+b} - \boldsymbol{a}\right). \tag{B.27}$$

If we assume infinitesimal b and a^{μ} we expand up to second order (to have non-zero terms). We get on each side of Eq. (B.27)

$$-ba^{\mu}[D, P_{\mu}]\varphi(\boldsymbol{r}) = ba^{\mu}iP_{\mu}\varphi(\boldsymbol{r}). \tag{B.28}$$

From this we surmise that $[D, P_{\mu}]\varphi(\boldsymbol{r}) = -iP_{\mu}\varphi(\boldsymbol{r})$.

This calculation may also resolve the apparent sign inconsistency discussed for the raising and lowering of the scaling dimensions around Eq. (3.73).

The action of the generators will be quoted as it can be found in detail in [22]. We have,

$$P_{\mu}\varphi(\boldsymbol{r}) = -i\partial_{\mu}\varphi(\boldsymbol{r}), \tag{B.29}$$

$$L_{\mu\nu}\varphi(\boldsymbol{r}) = i\left(r_{\mu}\partial_{\nu} - r_{\nu}\partial_{\mu}\right)\varphi(\boldsymbol{r}) + S_{\mu\nu}\varphi(\boldsymbol{r}), \tag{B.30}$$

$$D\varphi(\boldsymbol{r}) = \left(-i\Delta - ir^{\nu}\partial_{\nu}\right)\varphi(\boldsymbol{r}), \tag{B.31}$$

$$K_{\mu}\varphi(\boldsymbol{r}) = \left(-i2r_{\mu}\Delta - r^{\nu}S_{\mu\nu} - 2ir_{\mu}r^{\nu}\partial_{\nu} + i\boldsymbol{r}^2\partial_{\mu}\right)\varphi(\boldsymbol{r}). \tag{B.32}$$

We now can find the relation between $\varphi'(\boldsymbol{r})$ and $\varphi(\boldsymbol{r})$ for each case. To give a concrete example we study the dilations. More specifically, we consider the dilation for which

$$\boldsymbol{r}' = (1+\varepsilon)\boldsymbol{r}. \tag{B.33}$$

In this case, the Jacobian determinant of the transformation is given to first order in ε by $(1+\varepsilon)^d$. The φ transforms as

$$\begin{aligned}
\varphi(\boldsymbol{r}) \to \quad \varphi'(\boldsymbol{r}) &= \varphi(\boldsymbol{r}) - i\varepsilon D\varphi(\boldsymbol{r}) \\
&= \varphi(\boldsymbol{r}) - \varepsilon\Delta\varphi(\boldsymbol{r}) - \varepsilon r^{\nu}\partial_{\nu}\varphi(\boldsymbol{r}) \\
&= (1-\varepsilon\Delta)\varphi(\boldsymbol{r} - \varepsilon\boldsymbol{r}) \implies, \\
\varphi'(\boldsymbol{r} + \varepsilon\boldsymbol{r}) &= (1+\varepsilon)^{-\Delta}\varphi(\boldsymbol{r})
\end{aligned} \tag{B.34}$$

to first order in ε. We can now consider the correlation functions taken over the $\varphi'(\boldsymbol{r}')$ from the left hand side of Eq. (B.34), $\langle\varphi_1'(\boldsymbol{r}_1')\varphi_2'(\boldsymbol{r}_2')\varphi_3'(\boldsymbol{r}_3')\dots\rangle$. In a system with conformal symmetry the assumption is that, [22],

$$\langle\varphi_1'(\boldsymbol{r}_1)\varphi_2'(\boldsymbol{r}_2)\varphi_3'(\boldsymbol{r}_3)\dots\rangle = \langle\varphi_1(\boldsymbol{r}_1)\varphi_2(\boldsymbol{r}_2)\varphi_3(\boldsymbol{r}_3)\dots\rangle.^{1} \tag{B.35}$$

[1] The correlation functions are calculated through a path integral, $\langle\varphi_1(\boldsymbol{r}_1)\varphi_2(\boldsymbol{r}_2)\varphi_3(\boldsymbol{r}_3)\dots\rangle \sim \int[d\varphi]\varphi_1(\boldsymbol{r}_1)\varphi_2(\boldsymbol{r}_2)\varphi_3(\boldsymbol{r}_3)\dots e^{-S[\varphi]}$ [22]. The $S[\varphi]$ is the action and is taken to be conformally invariant when we admit conformal symmetry. According to [22] the further assumption for the Eq. (B.35) to hold is that the integration measure [dφ] must also remain invariant. Also, it evidently does not matter if we denote either $\boldsymbol{r}$ or $\boldsymbol{r}'$ on both sides of Eq. (B.35).

From Eq. (B.34) we then have

$$\langle\varphi_1(\boldsymbol{r}_1')\varphi_2(\boldsymbol{r}_2')\varphi_3(\boldsymbol{r}_3')\dots\rangle = \prod_i (1+\varepsilon)^{-\Delta_i}\langle\varphi_1(\boldsymbol{r}_1)\varphi_2(\boldsymbol{r}_2)\varphi_3(\boldsymbol{r}_3)\dots\rangle. \tag{B.36}$$

This yields the expected scaling form, where as we dilate the distance between fields (by resumming in the RG sense of App. D), we confirm the correct polynomial form for the correlation functions. The Δ is the scaling dimension of φ. We see that the prefactor $(1+\varepsilon)$ relates to the Jacobian in the same manner as b in Eq. (3.56). That is $b = (1+\varepsilon)$. For spinless fields, those for which $S_{\mu\nu} = 0$, we can make an infinitesimal SCT transformation using Eq. (B.32), in a very similar manner as we did for the dilations. In this case, we again have the form of Eq. (3.56) with $b = b(\boldsymbol{r})$.

Such transformations reveal why Eq. (3.56) looks like it does for spinless fields. Due to symmetry under conformal transformations the correlation functions of the transformed φ and of the original φ are equal. Therefore, (for spinless fields)

$$\prod_i b(\boldsymbol{r})^{\Delta_i}\langle\varphi_1(\boldsymbol{r}_1')\varphi_2(\boldsymbol{r}_2')\varphi_3(\boldsymbol{r}_3')\dots\rangle = \langle\varphi_1(\boldsymbol{r}_1)\varphi_2(\boldsymbol{r}_2)\varphi_3(\boldsymbol{r}_3)\dots\rangle. \tag{B.37}$$

A field for which this holds and b is related to the Jacobian as we described and $\tilde{\Delta}$ is a number, is called a quasi-primary [2].

Furthermore, we note that to first order in α_g for a certain transfomration G, the correlation function of the $\varphi(\boldsymbol{r})$ transforms as,

$$\begin{aligned}\langle\varphi_1(\boldsymbol{r}_1)\varphi_2(\boldsymbol{r}_2)\varphi_3(\boldsymbol{r}_3)\dots\rangle - i\alpha_g\big\{&\langle G\varphi_1(\boldsymbol{r}_1)\varphi_2(\boldsymbol{r}_2)\varphi_3(\boldsymbol{r}_3)\dots\rangle \\ &+ \langle\varphi_1(\boldsymbol{r}_1)G\varphi_2(\boldsymbol{r}_2)\varphi_3(\boldsymbol{r}_3)\dots\rangle \\ &+ \langle\varphi_1(\boldsymbol{r}_1)\varphi_2(\boldsymbol{r}_2)G\varphi_3(\boldsymbol{r}_3)\dots\rangle + \dots\big\}.\end{aligned} \tag{B.38}$$

Due to this linearity in first order we can directly use results such as Eq. (B.34) for each term. Admitting conformal symmetry, the left hand side of Eq. (B.35) is actually found via Eq. (B.38). Therefore, the part of Eq. (B.38) within the $\{\}$ should vanish [30].

Here, we only discussed explicitly the transformations of spinless fields, as these are sufficient for the purposes of the main text of the thesis. It is also possible to find how correlation functions transform for fields with spin (non-zero $S_{\mu\nu}$) [30].

B3 Mapping to the $S^2 \times \mathbb{R}$

As discussed in the main text around Eq. (3.61) and in App. B1, the transformation from $\mathbb{R}^3$ to $S^2 \times \mathbb{R}$ is not generated by the $d = 3$ conformal group, even though the geometries

[2] The distinction between the primary and the quasi-primary seems to not be relevant in $d = 3$ [16]. In $d = 2$ the fields that transform covariantly under projective conformal transformations (which correspond to the transformations we discuss in this appendix) are called quasi-primary, whereas the ones that transform covariantly under any conformal transformation (analytic function $w(z)$) are called primary [11].

are conformally related. This is because the mapping $r = e^{u/R}$ does not follow from integrating up infinitesimal transformations. Therefore, it is not obvious how one can derive Eq. (3.61), since it does not follow from the considerations of App. B2.

We will motivate an explanation following [30]. We can introduce radial coordinates for the $\mathbb{R}^3$, $(r, \boldsymbol{n})$, where $\boldsymbol{n}$ are the unit vectors of the angular part. If we consider again the transformation $u = R \ln r$ we can express the correlation functions of $\mathbb{R}^3$ as

$$\langle \varphi_1(r_1, \boldsymbol{n}_1)\varphi_2(r_2, \boldsymbol{n}_2)\ldots\rangle_{\mathbb{R}^3} = \frac{1}{r_1^{\Delta_1}}\frac{1}{r_2^{\Delta_2}}\ldots f(u_i - u_j, \{\boldsymbol{n}_i\}). \tag{B.39}$$

We explicitly took out factors $1/r_i^{\Delta_i}$. These factors account for the scaling of the correlation functions. This scaling corresponds to the discussion on App. B1. Since the scaling is taken care of it should be that the remaining terms depend on the ratios r_i/r_j as well as all the unit vectors $\boldsymbol{n}_i$. This then yields the dependence on $u_i - u_j$.

The assumption of conformal symmetry implies that the correlation functions on conformally related geometries are related to each other by a scale factor that may depend on position. We want to find this factor here. Since f in Eq. (B.39) depends on the difference of the coordinates of the cylinder and cannot be re-written as a difference of the r, we can infer that it is related to the correlation function of the fields on the cylinder. We may say that the cylinder field φ_{cyl} is given by, [30],

$$\varphi_{\mathrm{cyl}}(u, \boldsymbol{n}) = \frac{r^{\Delta}}{R^{\Delta}}\varphi_{\mathrm{flat}}(r, \boldsymbol{n}). \tag{B.40}$$

The scale factor is in thus $(r/R)^{\Delta}$. The r is there due to the prefactors in Eq. (B.39). The reason we included the R in the denominator comes from the fact that the Jacobian of the transformation is actually $dr/du = r/R$. Explicitly including the Jacobian in the transformation of the fields is motivated by the fact that the integration measure of an integral, that may include the fields (such as the action in quantum field theory [22]), transforms by this Jacobian. Demanding invariance due to conformal symmetry should correspond to φ transforming by the Jacobian to a certain power.

We also notice that the square root of the Weyl transformation between the $\mathbb{R}^3$ and $S^2 \times \mathbb{R}$ is given by $\sqrt{\Omega(r, \boldsymbol{n})} = R/r$ (see Eqs. (B.9) and (B.10)). Then we may assume that Eq. (B.39) is also written as

$$\langle \varphi_1(r_1, \boldsymbol{n}_1)\varphi_2(r_2, \boldsymbol{n}_2)\ldots\rangle_{S^2\times\mathbb{R}} = \frac{1}{\sqrt{\Omega(r_1)}^{\Delta_1}}\frac{1}{\sqrt{\Omega(r_2)}^{\Delta_2}}\ldots\langle \varphi_1(r_1, \boldsymbol{n}_1)\varphi_2(r_2, \boldsymbol{n}_2)\ldots\rangle_{\mathbb{R}^3}. \tag{B.41}$$

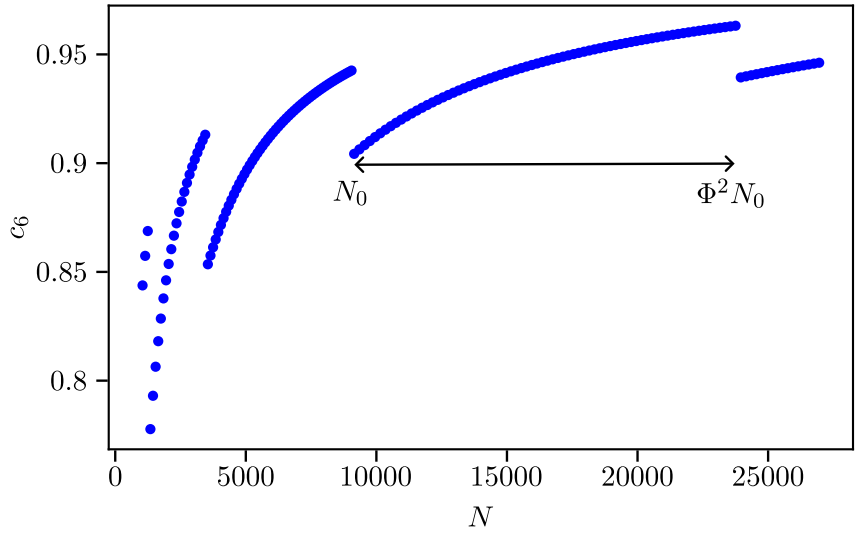

Figure C.1: Percentages of sites with 6 neighbors, c_6, with respect to system size N. The c_6 does not smoothly increase with N. It exhibits gaps that separate the curve into segments. Each segment spans system sizes that differ by the multiplicative factor of the golden ratio squared. If N_0 is the first system size of the segment then the last would be $\approx \Phi^2 N_0$. The segments progressively get less steep.

C Coordination numbers of the Fibonacci lattice

The lattice sites of the triangulated Fibonacci lattice do not all have the same number of neighbors. In particular, the majority of the lattice sites connect to 6 adjacent lattice sites, while the rest connect to either 5 or 7 adjacent lattice sites. As explained in App. A, the existence of lattice sites with a number of neighbors different than 6 is, in general, necessary in order to fulfill the Euler formula for the triangulated sphere, Eq (A.6).

We are interested in how the percentages of sites with 6 neighbors, c_6, and those with 5 and 7 neighbors, c_5 and c_7, vary with system size. In addition, as indicated in Eq. (2.19), the system size is directly related to the radius of the sphere. So, in geometric terms, we will see how the c relate to the curvature of the sphere.

In Fig. C.1 the c_6 is plotted with respect to N. While it typically increases with system size its behavior is not smooth. There appear distinct gaps where the value of c_6 is abruptly decreased. Therefore, the curve is actually separated in different segments. Each segment spans system sizes that differ by the multiplicative factor of the golden ratio squared. If N_0 corresponds to the first system size of the segment then the last is $\approx \Phi^2 N_0$.

We want to understand how c_6 increases with N within each segment and what happens at the points where the gaps appear. To do that we have to check the number of sites,

and not the percentages, with connectivity 5 and 7. We will annotate this absolute number of sites with uppercase C. The C_5 and C_7 remain essentially constant within the segments, especially as system size is increased, and show an abrupt increase at the same point where c_6 drops.

Since

$$c_j = \frac{C_j}{N}, \tag{C.1}$$

we know that due to the constant C_5 and C_7 the c_5 and c_7 simply scale with the inverse of N. This type of scaling is then also true for c_6, since $c_5 + c_6 + c_7 = 1$. In other words,

$$c_6 \approx 1 - \frac{\text{const}}{N} \qquad \text{within segments.} \tag{C.2}$$

For smaller system sizes than those plotted in Fig. C.1 the behavior is somewhat similar but not as smooth within the segments. Similar behavior of the c_6 in general is found for the coordination numbers in [40].

It is also interesting to note that the abrupt changes on the c happen at points where the configuration of the J is as the one indicated by the dashed arrow in Fig. 2.9. The large percentage of small values for J indicates, through Fig. 2.7, that many nearest neighbor distances are large.

D Renormalization group and the Ising model

In this section, the phase transition of the classical Ising model will be discussed. After illustrating the appearance of scale invariance at the point of the continous phase transition, we will introduce the renormalization group approach. The goal of this is to motivate the scaling of thermodynamic quantities with respect to system parameters; the temperature and the magnetic field. In addition, we will mention the φ^4 theory as it pertains to the description of the Ising model in the continuum.

This appendix is by no means a detailed description of continuous phase transitions nor is it a robust introduction to RG. To properly verify the validity of RG one should work on explicit models. Therefore, here, we resort to describing the logic behind it, mainly following the exposition of [17]. Throughout, we treat the general statements of RG as assumptions and try to put direct references when such statements appear.

Implicitly or explicitly we focus on the classical Ising model. The energy of a given configuration of spins for the Ising model is given by

$$E = -J \sum_{ij} s_i s_j - h \sum_i s_i. \tag{D.1}$$

The magnetization is obtained from the statistical average over the spin configurations $\{s\}$,

$$\begin{aligned} M &= \frac{1}{N}\sum_i \langle s_i \rangle \\ &= \frac{1}{N}\frac{1}{Z}\sum_{\{s\}}\sum_i s_i \exp\left(-\beta E(s)\right), \end{aligned} \tag{D.2}$$

where N is the total number of spins in the system. The susceptibility is the derivative of the magnetization with respect to the field h. It is then given by

$$\chi = \frac{\partial M}{\partial h}\Big|_{h=0} \tag{D.3}$$

$$= \frac{\beta}{N}\left(\langle S_{total}^2 \rangle - \langle S_{total} \rangle^2\right), \tag{D.4}$$

where $S_{total} = \sum_i s_i$. Furthermore, we define the cumulant

$$\Gamma(\boldsymbol{r}_i - \boldsymbol{r}_j) = \langle s_i s_j \rangle - \langle s_i \rangle \langle s_j \rangle. \tag{D.5}$$

The cumulant is an indicator of the statistical dependence of spins s_i and s_j. We assume that it is translationally and rotationally invariant. From it, we can get the important form of the susceptibility, according to which

$$\chi = \beta \sum_r^{\infty} \Gamma(r), \tag{D.6}$$

where by r we mean the distance between lattice points. The upper limit is taken to be infinite because we consider an infinite system. So, Eq. (D.6) illustrates how correlations at different length scales (that is different r) contribute to χ. Since the mean value of the spin or of s^2 is a bounded value, the value of the susceptibility only grows depending on how many of the terms in the sum actually contribute (being non-zero).

Due to this interpretation of the susceptibility we can describe the qualtitative characteristics of the phase transition. The classical Ising model undergoes at the critical temperature, T_c, a *continuous phase transition*. It is characterized by the divergence of quantities such as the susceptibility or the specific heat at the critical point (at least at $d = 3$ the specific heat is predicted to behave like this). Then, we can see from Eq. (D.6) that a divergence of the susceptibility corresponds to the existence of correlation at all length scales (terms continue to be non-zero up to the infinite limit of the sum in Eq. (D.6)).

Furthermore, the contribution from correlations at all length scales, at the phase transition, suggests that there is no one characteristic length scale to the system. In order to reconcile this with the appearance of a correlation length, ξ, in the correlation functions (such as the ones described in Section. 3.2 for example) we should take $\xi \to \infty$. In other

words, if ξ was finite, there should be no important contributions to Eq. (D.6) for $r > \xi$ (and hence there would not be a divergence).

The picture this suggests is the existence of regions of spins, in the lattice, that are correlated and that range in length from small (however larger than the lattice constant) up to ξ. When $\xi \to \infty$, the argumentation is that no matter if one zooms in or out of the system, they will essentially always see correlated regions at all length scales. This suggested *scale invariance* is the underlying idea for the renormalization group (RG) applications.

Practically, through the framework of RG we can mathematically evaluate the rescaling. In order to do this, we need to see what remains invariant upon this rescaling. A characteristic quantity that should remain invariant is the partition function

$$Z = \mathrm{Tr}_s e^{-\beta H(s)}. \tag{D.7}$$

An RG application on spin systems is the block spin transformations. The lattice, with lattice spacing a, is divided in blocks of linear size b, each of which contains more than one lattice site. There, a majority rule may be defined so that if most of the spins within the block are up (down) then the block is assigned a single spin value, s', which is up (down). The new Hamiltonian of the system is calculated by tracing out the possible spin configurations within each block.

The tracing out can be done in a manner that simultaneously enforces the majority constraint by using a projection operator, Q. Q takes the value 1 only for the configuration where the spins in the block, $\{s\}$, are in a majority of the same sign as s'. Otherwise it is zero. It follows that $\sum_{s'} Q(s', \{s\}) = 1$, as most spins in the block are necessarily either up or down. Therefore,

$$e^{-H'(s')} = \mathrm{Tr}_s \prod_{\text{blocks}} Q(s', \{s\}) e^{-H(s)}, \tag{D.8}$$

and

$$Z = \mathrm{Tr}_{s'} e^{-H'(s')} = \mathrm{Tr}_s e^{-H(s)}. \tag{D.9}$$

Here we redefined the Hamiltonian, H, to the reduced Hamiltonian βH. In this type of transformations, by taking the trace of spin configurations within each block, we coarse grained over the local degrees of freedom. We found a probability distribution, left hand side of Eq. (D.8), of quantities that depend on the larger-scale behavior of the spins (to the majority of them, s'). The general assumption that arises from Eq. (D.8) is that the probability distribution of quantities that depend on long wavelength degrees of freedom should be left invariant under the RG transformation.

Such block spin RG schemes have been implemented, for example, in the Ising model [41]. In doing so, the quantities that are monitored are actually the couplings, $\{K\}$, that appear in the transformed reduced Hamiltonian. From Eq. (D.1), for the Ising these would be βJ and βh. In fact, through the block spin transformations additional couplings (next

to nearest neighbors for example) might appear due to the coarse graining procedure (the tracing out). The question is if such couplings are relevant, in a sense to be defined immediately.

Under successive RG transformations, R, the couplings transform depending on the length b and the structure of the transformation $\{K'\} = R(\{K\})$. In principle, the new couplings depend not only on their previous value but also on the value of the other couplings. The very general assumption of the renormalization group transformation is that there exists a fixed point in the RG flow. At that point, $\{K'\} = \{K\} = \{K^*\}$.

The further assumption is that we can linearize the flow around the fixed point. For the deviations of the couplings around their fixed point value, $K'_a - K^*_a$, we have

$$K'_a - K^*_a \sim \sum_b T_{ab}(K_b - K^*_b). \tag{D.10}$$

The matrix T_{ab} is the Jacobian of the transformation, $\frac{\partial K'_a}{\partial K_b}\Big|_{K^*}$. This suggests that we can define scaling variables, υ^i, that are linear combinations of these deviations. These are defined as

$$\upsilon^i = \sum_a e^i_a(K_b - K^*_b) = \lambda^i \upsilon^i, \tag{D.11}$$

where $\boldsymbol{e}$ are the left eigenvectors of T_{ab}. We also assume that λ^i is real and set it as $\lambda^i = b^{y_i}$. According to the picture presented, the υ^i transform as

$$\upsilon^i \to b^{y_i}\upsilon^i, \tag{D.12}$$

near the critical point. What is important here is the sign of the exponent, y_i, of the multiplicative factor. If $y_i > 0$ then the υ will grow and, thus, move away from its fixed point value $\upsilon = 0$. In this case the scaling variable is relevant and must be set to 0. If $y_i < 0$ then υ will eventually reach its fixed point value. In the latter case the scaling variable is considered irrelevant, since it is anyway expected to reach the fixed point value irrespective of its initial value.

In the case of the Ising model, in order to find the critical point, the temperature and the magnetic field should be adjusted. The temperature dependence is usually given by the reduced temperature, $t = \frac{T - T_c}{T_c}$, so that at the critical point $t = 0$. Having to adjust two parameters indicates the existence of two relevant scaling variables; the thermal scaling variable, υ_t, and the magnetic scaling variable, υ_h. In general, through the RG, we are interested to see the manner in which the observables depend on the parameters of the systems. This way the nature of the divergences might be explained (which turn out to be a power law).

The thermodynamic observables are directly related to derivatives of the free energy with respect to the temperature or the magnetic field. So, divergences of observables

are attributed to the free energy. As we saw, the partition function remains invariant under an RG transformation. We consider the reduced free energy per site,

$$f\{K\} = -\frac{1}{N}\ln Z, \tag{D.13}$$

which depends on the couplings and through which we can calculate thermodynamic quantities. Under the renormalization group transformation that induces $N \to b^{-d}N$ on the number of blocks, f is assumed to transform as [17]

$$f(\{K\}) = g(\{K\}) + b^{-d} f_s(\{K'\}). \tag{D.14}$$

The first argument, $g(\{K\})$, in Eq. (D.14) is considered to be an analytic function of the $\{K\}$, even at the critical point. It is obtained by tracing out the degrees of freedom inside each block. So in the qualitative picture, where the appearance of the long wavelength correlations are the ones relevant for the divergences, it is reasonable to assume that it is analytic. Therefore, the divergences should be attributed to the singular part of the free energy, f_s, which transforms as

$$f_s(\{K\}) = b^{-d} f_s(\{K'\}). \tag{D.15}$$

The f_s can equivalently be considered a function of the scaling variables. Denoting only the two relevant scaling variables of the Ising model, which under multiple RG transformations rescale as seen in Eq. (D.12), we have

$$f_s(\upsilon_t, \upsilon_h) = b^{-nd} f_s(b^{ny_t}\upsilon_t, b^{ny_h}\upsilon_h). \tag{D.16}$$

Since this is expected to hold near the fixed point, we expect an upper bound on the times, n, we can iterate under the RG, so that Eq. (D.16) is satisfied. This is given by $|b^{ny_t}\upsilon_t| = \upsilon_{t0}$, where υ_{t0} is arbitrary but small enough. Solving for n, we can subsitute into Eq. (D.16).

Furthermore, we want an expression for the reduced free energy per site that entails the temperature and the magnetization variables (t and h respectively). For this we consider

$$\upsilon_t = \frac{t}{t_0} + O(t^2, h^2) \tag{D.17}$$

and

$$\upsilon_h = \frac{h}{h_0} + O(th). \tag{D.18}$$

So, u is taken to be an analytic function of t and h. The form of the dependence may be assumed, given that the critical point in the Ising model appears at vanishing magnetic field. For $h = 0$, the $\mathbb{Z}_2$ symmetry of the Ising model should be apparent even if additional couplings appear under the renormalization group flow. So the relevant variables are separated into two subspaces depending on even or odd symmetry under $s \to -s$. The h_0 and t_0 are non-universal constants, that is system specific parameters.

Solving for n as described and using Eqs. (D.17) and (D.18), the above discussion leads up to the general result according to which

$$f_s(t,h) = \left|\frac{t}{t_0}\right|^{d/y_t} \Phi\left(\frac{h/h_0}{|t/t_0|^{y_h/y_t}}\right). \tag{D.19}$$

The function Φ is called a scaling function. The dependence on system specific parameters is apparent only through h_0 and t_0 which are called scale factors.

Another notion that arises and is directly related to the above is that of universality. This may be seen from the argumentation that some couplings are irrelevant, in that they, irrespective of their initial value, reach the fixed point under RG transformations. This (loosely) suggests that critical systems with Hamiltonians that differ up to these irrelevant couplings, are described by the same fixed point.

In general, such fixed points are considered to define a universality class of critical behaviors, that describes the systems whose critical point eventually map onto it [10]. The criticality and free energy of the systems, in the neighborhood of the fixed point, is assumed to be identical. Under this general assumption, the scaling function of Eq. (D.19) and the scaling exponents we will discuss, are considered to be universal.

By taking derivatives of the scaling function, Eq. (D.19), we can then see the scaling behavior of thermodynamic observables at criticality. This way, one can verify that the scaling assumes a power-law form with respect to t or h, at the critical point. Since the scaling exponents are all related to y_t and y_h one can also infer relations between them that do not include the y.

The scaling relations at $h = 0$, take the form

$$C \sim |t|^{-\alpha} \qquad h = 0, \quad t \to 0, \tag{D.20}$$

$$M \sim (-t)^{\beta} \qquad h = 0, \quad t \to 0, \tag{D.21}$$

$$\chi \sim |t|^{-\gamma} \qquad h = 0, \quad t \to 0. \tag{D.22}$$

The thermodynamic quantities are the specific heat, the spontaneous magnetization and the susceptibility. We note here that M should not diverge since it is an intensive quantity, Eq. (D.2). Thus the exponent β is positive. In addition, in order for M to be non-zero the system should be in a spin configuration which is not symmetric under the $\mathbb{Z}_2$ symmetry. The symmetry breaking, which would allow this configuration is expected at infinite systems [42].

There is an additional scaling exponent, ν, that is attributed to the scaling with temperature of the correlation length. It is assumed, by the scaling hypothesis [43], that there exists a single correlation length ξ which is relevant in the system at criticality. However, correlation lengths are attributed to correlation functions which in principle measure something different. Examples are the spin and energy density correlation

functions in Section. 3.2, (although these specific ones were calculated for an anisotropic system).

The hypothesis may then imply that all correlation lengths scale with the same exponent ν. To infer the scaling of the correlation length we evaluate the connected spin-spin correlation function of Eq. (D.5). If we make a change in the Hamiltonian $\mathrm{H} \to \mathrm{H} - \sum_{\boldsymbol{r}} h_o(\boldsymbol{r}) s(\boldsymbol{r})$, the spin-spin correlation functions can be obtained by taking the second derivative of $\ln Z$ with respect to the small h_o,

$$G(\boldsymbol{r}_2 - \boldsymbol{r}_1) = \frac{\partial^2}{\partial h_o(\boldsymbol{r}_1) \partial h_o(\boldsymbol{r}_2)} \ln Z \Big|_{h_o=0}. \tag{D.23}$$

To find how this object transforms one has to evaluate the correlation function in the RG transformed Hamiltonian, $\mathrm{H}' = R\{\mathrm{H}\}$. We assume we are close to the fixed point. Since the Z remains invariant under the RG block spin transformation, one needs to evaluate how h_o transforms, since it also appears in Eq. (D.23). If we assume that $h_o(\boldsymbol{r})$ is a slowly varying field, then (given that the Hamiltonian has short range interactions) we may assume that $h_o(\boldsymbol{r}_i)$ transforms as a uniform field (acting with the same value in the neighborhood of i). This assumption implies that $h_o(\boldsymbol{r}_i)$ transforms as v_h, since v_h is given to first order by the uniform field h, Eq. (D.18).

In turn, this means that the transformed Hamiltonian has the same form insofar as h_o is concerned, with $h_o \to h'_o$ and the spins being the block spins s'. To find the G' we take the second derivative of the unchanged $\ln Z$ with respect to h'_o. We actually have to evaluate this derivative in terms of the original h_o in order to see how G' is related to G. However, as mentioned, the h'_o are local fields acting on the resulting block spins, s'.

Therefore, a change on $h'_o(\boldsymbol{r}'_i)$ corresponds to a change on all the fields $h_o(\boldsymbol{r}_i)$ acting on the original spins, s, within that block. Since the partition function remains invariant we have

$$\ln Z' \left(h'_o + \delta h'_o \left(\boldsymbol{r}'_1 \right) \right) = \ln Z \left(h_o(\boldsymbol{r}_i) + \sum_i \delta h_o(\boldsymbol{r}_i) \right), \tag{D.24}$$

where on the right hand side we have to sum over all i which are included in the block $\boldsymbol{r}'_1$. We expand the reduced free energies up to second order, so that the second order derivative of Eq. (D.23) comes out. We can then evaluate G' in terms of G. More specifically, denoting G' as $G_{\mathrm{H}'}$ to indicate that it is evaluated in the transformed Hamiltonian, we have

$$G\left((\boldsymbol{r}_2 - \boldsymbol{r}_1)/b\right)_{\mathrm{H}'} = b^{2(d-y_h)} G\left(\boldsymbol{r}_2 - \boldsymbol{r}_1\right)_{\mathrm{H}}. \tag{D.25}$$

The factor b^d comes from the fact that in the sum of Eq. (D.24), the spins within each block are in total b^d in units of lattice spacing. The factor of 2 in the exponent arises due to the double summation of i in the second order expansion. The b^{-2y_h} is due to the h_o rescaling. Explicitly denoting the t dependence and setting $h = 0$, we get

$$G(r, t) = b^{-2(d-y_h)} G(r/b, b^{y_t} t). \tag{D.26}$$

Writing this, we assumed isotropic behavior for $G(r,t)$ and dropped the dependence on the Hamiltonians as this is indicated by the rescaling of r. Actually, the approximation of isotropy in a lattice should become better at large distances. This is expected to hold, however, if the short range interactions are isotropic. For example, in the case where the interactions in the x and y directions differed, we would expect this anisotropy to be apparent even at large scales (when comparing the x and y direction at large scale).

At the critical point $t = 0$, Eq. (D.26) indicates for $G(r)$ at large distances,

$$G(r) \propto r^{-2(d-y_h)}. \tag{D.27}$$

We also want to see how the correlation length scales with respect to t as $t \to 0$. For this, we can again make n iterations of the rescaling of Eq. (D.26) up to a point where the linearized RG transformations are valid. Solving for n, this gives

$$G(r,t) = \left|\frac{t}{t_0}\right|^{2(d-y_h)/y_t} \Psi\left(r/\left|t/t_0\right|^{-1/y_t}\right). \tag{D.28}$$

We assume that $G(r) \propto e^{-r/\xi}$ and observe the dependence $\propto r/\left|t\right|^{-1/y_t}$ in Eq. (D.28). Then the correlation length would scale as $\xi \propto \left|t\right|^{-1/y_t}$. This scaling exponent is denoted ν, and is equal to $\nu = 1/y_t$.

It turns out that due to the dependence of α, Eq. (D.20), on the y and due to $\nu = 1/y_t$ we can infer the hyperscaling relation

$$\alpha = 2 - d\nu. \tag{D.29}$$

Here, the α is the exponent related to the specific heat, which is related to the correlation function of the energy density. The ν is related to the correlation length which, as we saw, can be inferred from the spin-spin correlation function.

At various points we re-expressed the reduced free energy in terms of v_t and v_h (which in this case are to first order proportional to t and h). However, in the general case, there is a subtlety introduced when we do that. The Hamiltonian is initially expressed in terms of the interaction coefficients K (for example βJ and βh here) and the interaction terms (for example the sums over $s_i s_j$ and s_i here). In principle, then, if the scaling fields explicitly appear instead of the K, they will not necessarily couple to the previous interaction terms.

They will couple to the scaling operator or scaling fields, which we will denote as φ. To be consistent, the φ should in turn be able to be re-expressed as a combination of the interaction terms. In fact, introducing the Hamiltonian in the continuum limit we should have

$$\mathrm{H} \propto \sum_i v_i \int \varphi_i(r) \frac{d^d r}{\alpha^d}. \tag{D.30}$$

The summation over i indicates the scaling variables coupling to their corresponding field and the $\int d^d r/\alpha^d$ follows from limiting procedure of making the discrete lattice sum a continuous quantity. This suggests that under an RG transformation where the lattice spacing is dilated $\alpha \to b\alpha$ and $\upsilon_i \to b^{y_i}\upsilon_i$, the partition function may stay invariant if $\varphi_i(r) \to b^{d-y_i}\varphi_i(r)$. The $d - y_i$ should then be the scaling dimension, Δ_i, of φ_i,

$$\Delta_i = d - y_i. \tag{D.31}$$

Therefore, technically, it should be the correlation functions of the scaling field φ_h, that obeys relations such as Eq. (D.28). In this equation we also see $\Delta_h = d - y_h$. We can now specifically understand the Ising model's scaling fields (φ_t and φ_h). We can see the relation between the scaling variables and the interaction terms in Eqs. (D.17) and (D.18). Due to this proportionality to first order, we may then motivate that the main content of the scaling fields is described by the spin density (s_i) and the energy density ($s_i s_j$).

Furthermore, due to the rescaling $\varphi_i(r) \to b^{d-y_i}\varphi_i(r)$, one may generalize the rescaling of the correlation function of φ [17],

$$\begin{aligned}\langle \varphi_1(r_1)\varphi_2(r_2)\ldots\varphi_N(r_N)\rangle = \\ b^{-\Delta_1-\Delta_2\ldots-\Delta_N}\langle \varphi_1(r_1/b)\varphi_2(r_2/b)\ldots\varphi_N(r_N/b)\rangle.\end{aligned} \tag{D.32}$$

Nevertheless, the continuum limit, Eq. (D.30), was taken by brute force. Also we did not account for a cut-off in the integral, which would correspond to the lattice constant being the smallest lattice distance. One may study the Ising universality class in the continuum by using effective Hamiltonian,

$$\mathrm{H} = \int d^d r \left[\frac{1}{2}(\nabla\varphi)^2 + \frac{1}{2}ta^{-2}\varphi^2 + ua^{d-4}\varphi^4 + ha^{-d/2-1}\varphi\right]. \tag{D.33}$$

The $\varphi = \varphi(r)$ here is the scalar order parameter of the theory. It might also be denoted φ corresponding to the φ^4 theory. The corresponding partition function of this system integrates over possible configurations for each $\varphi(r)$. It might seem arbitrary to introduce such a Hamiltonian. However, one can map the Ising spin model to a continuous path integral version [42]. This version includes higher order terms in φ. The reason the Hamiltonian contains up to φ^4 may be justified by considering the relevance of the higher order in φ around the fixed point.

In general it is not our purpose to delve into the approximate solution (namely the ε-expansion) of this theory. Here, we will only state some basic intuitions and results. Firstly, to infer information for the fixed points we may do a dimensional analysis. So if we consider rescaling $a \to ba$ and demand that only the parameters change but the

Hamiltonian is invariant we would have

$$t' = b^2 t, \tag{D.34}$$

$$h' = b^{d/2+1} h, \tag{D.35}$$

$$u' = b^{4-d} u. \tag{D.36}$$

The results indicate that there is a fixed point when the scaling variables are all zero. In this case only the first term remains in the Hamiltonian of Eq. (D.33). At $d > 4$ the relations indicate that u is an irrelevant coupling. Therefore this fixed point is described by the two relevant variables that correspond to the thermal and magnetic sector. This motivates why this fixed point may describe the critical Ising model. However, for $d > 4$ the mean field theory is expected to hold due to the Ginzburg criterion. There is an inconsistency between the Gaussian predictions (Gaussian due to setting t, h and u equal to zero in Eq. (D.33)) and the exponents predicted by mean field [17].

This dimensional analysis essentially corresponds to the lowest order and naive implementation of an RG transformation, since we simply rescale and demand that the Hamiltonian remains invariant. However, one can verify, by calculating the correlation function $\langle \varphi(\boldsymbol{r}_1)\varphi(\boldsymbol{r}_2)\rangle$ at the Gaussian fixed point, that the scaling dimension of the field φ^2 is indeed given by $\Delta = d - y_t$. The $y_t = 2$ is given by Eq. (D.34).

In general a more complete RG transformation is performed through the ε-expansion. In this expansion one essentially keeps track of how the scaling variables change (up to orders of $\varepsilon = 4 - d$) under infinitesimal RG transformations from the Gaussian fixed point to a new fixed point which is relevant one at criticality (since u is a relevant scaling variable). That is the Wilson-Fisher fixed point. From the flow of the scaling variables we can infer, up to orders of ε, the scaling exponent of the scaling variables at the Wilson-Fisher fixed point. To be clear, at zero order the scaling variable has the value as it is calculated from the Gaussian fixed point Hamiltonian (and with respect to this Hamiltonian is it initially considered to have the properties of a scaling variable).

The RG transformed Hamiltonian, which is obtained by a coarse graining procedure, should be re-expressed with the same integral limit so that the transformed scaling variables may be compared to the initial ones. So, the process includes a coarse graining and a rescaling. However, more detail on the ε-expansion shall not be part of the thesis. It can be found, for example, in [32] or [44].

Lastly, we would like to discuss the role of anisotropy in the Ising model at criticality. We implicitly assumed that the system we treat is isotropic, in the sense that the lattice spacing and the interaction are the same in every direction. This is not necessarily the case and in the context of the thesis, where we treat irregular lattices, it is surely not guaranteed. In general it is possible for interactions to be different in each direction. For example in $d = 3$, we may change the constant interaction term J in Eq. (D.1) to J^x, J^y, and J^z.

In order to discuss anisotropy in the physical system (and to be concrete on how both the choice of the interaction terms and of the lattice contribute) we should look at the interaction part of the Ising model. If we assume a continuous spin variable, $s(\boldsymbol{r})$, in the spirit of Eq. (D.33), the interaction terms would look like $\sum_{ij} J(\boldsymbol{r}_i - \boldsymbol{r}_j)s(\boldsymbol{r}_i)s(\boldsymbol{r}_j)$. Expanding in $\boldsymbol{r} = (r^1, r^2, ..)$ around a specific point i, we get

$$\sum_j J(\boldsymbol{r}_i - \boldsymbol{r}_j)s(\boldsymbol{r}_i)s(\boldsymbol{r}_j) \approx$$
$$\sum_j J(\boldsymbol{r}_i - \boldsymbol{r}_j)s(\boldsymbol{r}_i)\Bigg(s(\boldsymbol{r}_i) + \sum_k \left.\frac{\partial s}{\partial r^k}\right|_{\mathbf{r}_i} (r_i^k - r_j^k) + \sum_{k,l} \left.\frac{\partial^2 s}{\partial r^k \partial r^l}\right|_{\mathbf{r}_i} (r_i^k - r_j^k)(r_i^l - r_j^l) + \dots \Bigg). \quad \text{(D.37)}$$

Firstly, if the system is isotropic then the first order term is zero,

$$\sum_j J(\boldsymbol{r}_i - \boldsymbol{r}_j)(r_i^k - r_j^k) = 0. \quad \text{(D.38)}$$

This is also zero if the lattice is regular but looks different in each direction (for example a regular rectangular lattice where the lattice spacing in one dimension is larger than the other and has different J between the dimensions). In addition, the second order cross terms in the Taylor expansion are also zero for the isotropic system

$$\sum_j J(\boldsymbol{r}_i - \boldsymbol{r}_j)(r_i^k - r_j^k)(r_i^l - r_j^l) = 0. \quad \text{(D.39)}$$

These are also zero for a system defined on a regular lattice which looks different in each direction, both in terms of lattice spacing and J. However, the discrepancy, between an isotropic system and one that is defined on a regular lattice but is anisotropic, comes from the diagonal second order terms. Namely, for the isotropic case we have non-zero second order terms that look like

$$\sim c \sum_k \frac{\partial^2 s}{\partial \left(r^k\right)^2}, \quad \text{(D.40)}$$

whereas for the anisotropic but regular type of systems they are

$$\sim \sum_k c_k \frac{\partial^2 s}{\partial \left(r^k\right)^2}. \quad \text{(D.41)}$$

The c or c_k here are just coefficients that come from the summation in Eq. (D.37). If we now assume the continuous limit, where the sum becomes an integral, we can integrate by parts both expressions. This results in the appearance of terms $\left(\partial s/\partial r^k\right)^2$. In fact,

this type of second order expansion goes into setting the φ^4 approximation. Then we can see that the first term of the φ^4 Hamiltonian, Eq. (D.33), corresponds to the case of an isotropic system, i.e. Eq. (D.40) [17].

An anisotropic system, in the sense that Eq. (D.41) holds, should then include different second order terms for each direction in its φ^4 approximation. Nevertheless, the second order derivatives in each direction still appear essentially on same footing. Then, the assumption for the Ising model at criticality is that by rescaling the lattice spacing in each direction appropriately (given that the integrals go to infinity and so on), we can treat the anisotropic problem essentially as the isotropic one [17].

In any case, this motivation should be more explicitly verified. The anisotropy apparent in the TFIM (which is relevant for the thesis) is introduced due to the quantum to classical mapping. There the anisotropy appears between the time and the spatial directions.

We should note that we expanded up to second order and not up to any higher order in Eq. (D.37). This is justified retroactively in the context of RG. It is again a question about the relevance (in the RG sense) of higher order terms and whether or not they give subleading corrections.

Acknowledgements

Firstly, I would like to thank Fabian for the suggestion to work on this peculiar problem and his passionate support of it. His close supervision of my work and the multiple insights he naturally provided for the thesis helped me greatly to improve as a physicist. I would also like to thank him for the opportunity he provided to present the work on a conference and for his meticulous attention to detail when it came to presentations and posters.

Furthermore, I want to thank Stefan for being my second supervisor and for his suggestions and insights especially on the treatment of the spin system. I look forward to working with him in the future. Moreover, I thank him for providing the SSE quantum monte carlo code for the thesis and granting the additional computing resources. Computations were also performed by computing resources granted by RWTH Aachen University under project "thes1750".

I also thank Ion Cosma Fulga for his suggestions on the Fibonacci lattice as well as providing the first (quite helpful) coding section of the thesis.

The every day life in the office was quite pleasant and at times very whimsical. I want to thank all the people in the IQI for creating a friendly and warm environment. It was really fun to share the office with Konstantinos, David and Steven and I really had a great time when we attended the DPG conference together. A shoutout also goes to Steven for proofreading part of the thesis and for general moral support. Thanks also to Don, Julius and Tobias for the occasional fun encounters and conversations. Discussing the arbitrariness of life and of Germany was always a fun way to pass those late afternoons in the office with Nikolaos. May we have many more of those.

Special thanks also go to Raffaele, Björn and Juval for being my friends in this new country and for all the fun times we had in the last two years. I want to thank my family and friends in Greece for their love and constant support throughout the years. Lastly, I would like to thank my partner, Eleni, who has been unconditionally loving and supportive this very demanding year. Thank you for being there for every emotional turmoil the thesis brought and for making Aachen feel like home.

Bibliography

[1] Edward B Saff and Amo BJ Kuijlaars. Distributing many points on a sphere. *The mathematical intelligencer*, 19:5–11, 1997.

[2] Oleg R Musin and Alexey S Tarasov. The tammes problem for n= 14. *Experimental Mathematics*, 24(4):460–468, 2015.

[3] Luca Maria Del Bono, Flavio Nicoletti, and Federico Ricci-Tersenghi. The most uniform distribution of points on the sphere. *arXiv preprint arXiv:2407.01503*, 2024.

[4] Michael Atiyah and Paul Sutcliffe. Polyhedra in physics, chemistry and geometry. *arXiv preprint math-ph/0303071*, 2003.

[5] Oleg A. Vasilyev, Anna Maciołek, and S. Dietrich. Sensitivity of the thermodynamics of two-dimensional systems towards the topological classes of their surfaces. *Physica A: Statistical Mechanics and its Applications*, 624:128960, 2023.

[6] Richard C Brower, Michael Cheng, and George T Fleming. Improved lattice radial quantization. *arXiv preprint arXiv:1407.7597*, 2014.

[7] Richard C Brower and Evan K Owen. The ising model on $\mathbb{S}^2$. *arXiv preprint arXiv:2407.00459*, 2024.

[8] Evguenii A Rakhmanov, Edward B Saff, and YM1306011 Zhou. Minimal discrete energy on the sphere. *Mathematical Research Letters*, 1(6):647–662, 1994.

[9] Colin J Cotter. Compatible finite element methods for geophysical fluid dynamics. *Acta Numerica*, 32:291–393, 2023.

[10] Michael E Fisher. Renormalization group theory: Its basis and formulation in statistical physics. *Reviews of Modern Physics*, 70(2):653, 1998.

[11] Philippe Christe and Malte Henkel. *Introduction to conformal invariance and its applications to critical phenomena*, volume 16. Springer Science & Business Media, 2008.

[12] John L Cardy. Universal amplitudes in finite-size scaling: generalisation to arbitrary dimensionality. In *Current Physics–Sources and Comments*, volume 2, pages 370–373. Elsevier, 1988.

[13] FC Alcaraz and HJ Herrmann. Numerical difficulties in obtaining 3d critical exponents from platonic solids. *Journal of Physics A: Mathematical and General*, 20(16):5735, 1987.

[14] Martin Weigel and Wolfhard Janke. Universal amplitude-exponent relation for the ising model on sphere-like lattices. *Europhysics Letters*, 51(5):578, 2000.

[15] Richard C Brower, George Fleming, Andrew Gasbarro, Timothy Raben, Chung-I Tan, and Evan Weinberg. Quantum finite elements for lattice field theory. Technical report, 2016.

[16] Wei Zhu, Chao Han, Emilie Huffman, Johannes S Hofmann, and Yin-Chen He. Uncovering conformal symmetry in the 3d ising transition: state-operator correspondence from a quantum fuzzy sphere regularization. *Physical Review X*, 13(2):021009, 2023.

[17] J. Cardy. *Scaling and Renormalization in Statistical Physics*. Cambridge Lecture Notes in Physics. Cambridge University Press, 1996.

[18] JN Ridley. Packing efficiency in sunflower heads. *Mathematical Biosciences*, 58(1):129–139, 1982.

[19] G.H. Hardy, E.M. Wright, D.R. Heath-Brown, and J. Silverman. *An Introduction to the Theory of Numbers*. Oxford mathematics. OUP Oxford, 2008.

[20] Geertjan Huiskamp. Difference formulas for the surface laplacian on a triangulated surface. *Journal of computational physics*, 95(2):477–496, 1991.

[21] M. Hamermesh. *Group Theory and Its Application to Physical Problems*. Addison Wesley Series in Physics. Dover Publications, 1989.

[22] P. Francesco, P. Mathieu, and D. Senechal. *Conformal Field Theory*. Graduate Texts in Contemporary Physics. Springer New York, 2012.

[23] Sheer El-Showk, Miguel F Paulos, David Poland, Slava Rychkov, David Simmons-Duffin, and Alessandro Vichi. Solving the 3d ising model with the conformal bootstrap. *Physical Review D—Particles, Fields, Gravitation, and Cosmology*, 86(2):025022, 2012.

[24] S. Sachdev. *Quantum Phase Transitions*. Cambridge University Press, 2011.

[25] Masuo Suzuki. Relationship between d-dimensional quantal spin systems and (d+1)-dimensional ising systems: Equivalence, critical exponents and systematic approximants of the partition function and spin correlations. *Progress of theoretical physics*, 56(5):1454–1469, 1976.

[26] Sei Suzuki, Jun-ichi Inoue, and Bikas K Chakrabarti. *Quantum Ising phases and transitions in transverse Ising models*, volume 862. Springer, 2012.

[27] K. Binder. Critical properties from monte carlo coarse graining and renormalization. *Phys. Rev. Lett.*, 47:693–696, Aug 1981.

[28] MSL du Croo de Jongh and JMJ Van Leeuwen. Critical behavior of the two-dimensional ising model in a transverse field: A density-matrix renormalization calculation. *Physical Review B*, 57(14):8494, 1998.

[29] Marc Gillioz. Conformal field theory for particle physicists. *arXiv preprint arXiv:2207.09474*, 2022.

[30] Slava Rychkov. *EPFL lectures on conformal field theory in $D \geq 3$ dimensions*, volume 10. Springer, 2017.

[31] John Cardy. Conformal field theory and statistical mechanics. *Exact Methods in Lowdimensional Statistical Physics and Quantum Computing (Oxford University Press, Oxford, 2010)*, pages 65–98, 2008.

[32] J. Zinn-Justin. *Phase Transitions and Renormalization Group*. Oxford Graduate Texts. OUP Oxford, 2007.

[33] KSD Beach, Ling Wang, and Anders W Sandvik. Data collapse in the critical region using finite-size scaling with subleading corrections. *arXiv preprint cond-mat/0505194*, 2005.

[34] Anders W. Sandvik. Stochastic series expansion method for quantum ising models with arbitrary interactions. *Phys. Rev. E*, 68:056701, Nov 2003.

[35] Anders W. Sandvik, Adolfo Avella, and Ferdinando Mancini. Computational studies of quantum spin systems. In *AIP Conference Proceedings*. AIP, 2010.

[36] Henk WJ Blöte and Youjin Deng. Cluster monte carlo simulation of the transverse ising model. *Physical Review E*, 66(6):066110, 2002.

[37] W Selke. The critical binder cumulant for isotropic ising models on square and triangular lattices. *Journal of Statistical Mechanics: Theory and Experiment*, 2007(04):P04008, 2007.

[38] Martin Hasenbusch. Finite size scaling study of lattice models in the three-dimensional ising universality class. *Physical Review B—Condensed Matter and Materials Physics*, 82(17):174433, 2010.

[39] Youjin Deng and Henk WJ Blöte. Simultaneous analysis of several models in the three-dimensional ising universality class. *Physical Review E*, 68(3):036125, 2003.

[40] AS Pochinok, AV Molochkov, and MN Chernodub. Ising model on the fibonacci sphere. *arXiv preprint arXiv:2301.06849*, 2023.

[41] Th. Niemeijer and J. M. J. van Leeuwen. Wilson theory for spin systems on a triangular lattice. *Phys. Rev. Lett.*, 31:1411–1414, Dec 1973.

[42] N. Goldenfeld. *Lectures On Phase Transitions And The Renormalization Group.* CRC Press, 2018.

[43] Shang-keng Ma. Introduction to the renormalization group. *Reviews of Modern Physics*, 45(4):589, 1973.

[44] Kenneth G. Wilson and J. Kogut. The renormalization group and the ε expansion. *Physics Reports*, 12(2):75–199, 1974.